A Novel SPH Method for Investigating the Role of Saliva in Swallowing using 4D CT images

by

Andrew Kenneth Ho

B.E.Sc., The University of Western Ontario, 2008
M.E.Sc., The University of Western Ontario, 2010

A THESIS SUBMITTED IN PARTIAL FULFILLMENT OF
THE REQUIREMENTS FOR THE DEGREE OF

DOCTOR OF PHILOSOPHY

in

The Faculty of Graduate and Postdoctoral Studies

(Electrical & Computer Engineering)

THE UNIVERSITY OF BRITISH COLUMBIA

(Vancouver)

April 2017

Abstract

The thesis presents novel computer methods towards simulation of oropharyngeal swallowing. The anatomy and motion of the human upper airway was extracted from dynamic Computed Tomography (CT) data using a novel tool and workflow. A state-of-the-art SPH method is extended to accommodate non-Newtonian materials in the extracted geometries. A preliminary numerical experiment of six human oropharyngeal swallows using Smoothed Particle Hydrodynamics (SPH) demonstrates that the methods are robust and useful for simulation of oropharyngeal swallowing.

The presence of saliva is well known to be important for mastication, swallowing, and overall oral health. However, clinical studies of patients with hyposalivation are unable to isolate the effect of saliva from other confounding factors. The simulation presented in this thesis examines fluid boluses under lubricated and non-lubricated boundary conditions. Upon comparison with medical image data, the experiments suggest that saliva does not provide a significant lubricative effect on the bolus transit times, but it may serve to reduce residue and therefore improve overall swallowing efficacy. Our findings, while preliminary, corroborate with existing clinical research that finds that groups with hyposalivation do not have significantly different transit times with control groups, but that residue may be increased

in the hyposalivation group.

Previous studies using computer simulation of fluid flow in the oropharynx typically make use of simplified geometries. Our work uses dynamic 320-row Area Detector Computed Tomography (ADCT) images as the basis for the simulations, and therefore does not require simplifying geometric assumptions. Since the data are dynamic, motion trajectories are all supplied by the ADCT data, and extrapolation from 2D sources such as bi-plane videofluoroscopy is not required. Processing the image data required the development of a novel workflow based on a new tool, which we call *BlendSeg*. We utilize and extend Unified Semi-Analytic Wall (USAW) SPH methods so that orophrayngeal swallowing simulations may be performed. These extensions include the simulation of non-Newtonian boluses, and moving 3D boundaries. Partial validation of the extended USAW SPH method is performed using canonical flows.

Preface

A swallowing proof-of-concept model using SPH to represent a bolus in a biomechanical model of a human head was published in [55].

The extensions to USAW SPH described in Chapter 3 were performed by myself in collaboration with Prof. Sheldon Green and Prof. Sidney Fels. Prof. Green and Prof. Fels advised me on the suitable assumptions for oropharyngeal swallowing, and the extensions required in USAW SPH. They also advised me on suitable experiments to run for the partial validation. I derived the extensions for the moving boundaries in 3D, and the non-Newtonian materials. I also performed the validation experiments and wrote the chapter.

The experiments in Chapter 4 were conducted at UBC by myself in collaboration with Dr. Yoko Inamoto, Dr. Eiichi Saitoh, Prof. Rebecca Affoo, Prof. Nicole Rogus-Pulia, Prof. Mark Nicosia, Prof. Sheldon Green, and Prof. Sidney Fels. The 320-row ADCT data was gathered by Dr. Inamoto, Dr. Saitoh, and their colleagues at Fujita Health University in Japan. They allowed us to use the data for our numerical simulations and provided verification of the airway identification using *BlendSeg*. They also generated the CT images and provided feedback on the chapter. Dr. Affoo and Dr. Rogus-Pulia performed the bolus transit time measurements of the

ADCT data and the simulations. They also provided clinical analysis of the results, and feedback on the chapter. Prof. Nicosia, Prof. Green and Prof. Fels provided support with the interpretation of fluid simulation results, as well as feedback on the chapter. I extracted the airway from the ADCT images using *BlendSeg*, and ran the extended USAW SPH simulation of the slip and no-slip simulations. I also wrote the bulk of the chapter. The work in Chapter 4 was approved by the UBC Clinical Research Ethics Board under certificate no. H16-01546.

A version of section 4.3 describing a workflow for extracting dynamic boundaries from 4D data using *BlendSeg*, has been published in [54]. Dr. Yoko Inamoto and Dr. Eiichi Saitoh provided the 320-row ADCT data. I was responsible for the design of the workflow, the creation of the *BlendSeg* tool, and also wrote the manuscript.

The rheology measurements of the bolus, described in Section 4.4, were performed at UBC in Prof. Dana Grecov's rheology lab, by Nick Yeh and myself. Nick performed the rheology measurements using the *KINEXUS* rheometer. I prepared the samples, and fit a Cross model to the data.

Table of Contents

List of Tables

List of Figures

Acknowledgements

First and foremost, I would like to thank Dr. Yoko Inamoto and Dr. Eiichi Saitoh of Fujita Health University. Without the research they have conducted, as well as their willingness to collaborate, the bulk of this thesis would have been impossible. I must thank Prof. Mark Nicosia for his guidance and wisdom in fluid simulation and swallowing. I would also like to thank Prof. Rebecca Affoo, who has spent an enormous amount of time getting me up to speed on saliva. To Prof. Bill Pearson and Dr. Jana Rieger, thank you for your invaluable support with anatomy and physiology of swallowing, as well as the interpretation of the 320-row ADCT images. Dr. Nicole Rogus-Pulia, thank you for the support and interpretation of the oropharyngeal swallowing results. Nick Yeh and Dr. Dana Grecov, thank you for your help with measuring the rheology of the bolus.

Last and most importantly, I would like to thank my advisors for their support and guidance. Thank you Sheldon, for all the chocolate, and Sid, for believing in me.

I dedicate this thesis to my dad, who always believed in me, my mum, who pushed me to graduate and get a job, and Ronnie, who put up with me through all these years.

Chapter 1

Introduction

Swallowing disorders (dysphagia) occur for a multitude of reasons, including, but not limited to, muscle and tissue changes associated with aging, neurological disorder such as stroke or Parkinson's disease, and oncology treatment for tumours in the head and neck region. Dysphagia may lead to a significant decrease in quality-of-life and malnutrition. Aspiration of foreign materials into the lungs can lead to pneumonia and death. In a retrospective cross-sectional study, researchers found that over 50% of head and neck cancer patients treated with surgery combined with radiotherapy or chemotherapy suffered from oropharyngeal dysphagia, with malnutrition present in 20% of patients [37].

One factor that is thought to contribute to dysphagia is reduced saliva production, or hyposalivation. For example, Pauloski et al. [101] found that head and neck cancer subjects who underwent intensity-modulated radiotherapy, which was used to target the tumour while sparing the salivary glands, performed better in swallowing tasks than a control group that underwent conventional radiotherapy. This suggests that sparing the salivary glands improves swallowing function. However in a study by Rogus-Pulia et al. [107], the authors found that in subjects with Sjögren's syndrome,

an autoimmune disorder that results in an extremely dry mouth, 96% of swallows were judged to be functional, and no strong correlation was found between temporal measures of swallowing and salivary flow rate. One of the challenges in drawing strong conclusions from patient data is that often it is impossible to separate the variable of interest, for example salivary flow rate, from other confounding factors, such as reduced mobility of the tongue, hindering the analysis of the data.

This thesis describes the extension of a state-of-the-art fluid simulation technique, Unified Semi-Analytic Wall (USAW) SPH [32], for the purpose of simulating oropharyngeal swallowing of non-Newtonian fluids. The simulation method has been widely used for wave simulation, and possesses desirable features such as an implicit representation of the air-liquid interface, and a natural handling of complex 3D geometry.

320-row Area Detector Computed Tomography (ADCT) datasets give us an unprecedented view of the human head and neck during swallowing [57]. The data also presents unique processing challenges when trying to extract geometry that can be used in a computer simulation. A novel workflow centred around a newly created tool, *BlendSeg*, was developed in order to extract the airway boundary correctly from the ADCT data.

A computer simulation of oropharyngeal swallowing is performed using the airways extracted from the ADCT data, and the extensions to the USAW SPH method. These preliminary experiments of starch-thickened liquid boluses in the oropharynx give us insight into the role of saliva in normal swallows. The results suggest that in healthy subjects saliva does not significantly increase the speed of starch-thickened boluses, contrary to

our initial expectations. However, saliva may help to decrease the quantity of residue after swallowing. Although these are preliminary experiments, they highlight the need for further study of this complex phenomenon.

1.1 Computer simulation of swallowing

Computer simulation of fluids can help us achieve a greater understanding of the physics in the human body because a simulation is able to isolate and change a single variable in order to understand its contribution to the overall phenomena. It is also useful in situations where detailed measurements and observations are difficult or impossible to perform. For example, *in-vivo* measurements of the bolus flow in swallowing are usually limited to 2D videofluoroscopic studies, fibreoptic endoscopic studies, or manometry. Measuring quantities such as the saliva thickness on the surface of the tongue during swallowing, shear-rates and intra-bolus velocity is impossible with modern technology. Because of these difficulties, computer simulation presents an attractive alternative that allows us to predict these quantities with a mathematical model.

Swallowing is a complex phenomenon that most people take for granted. People swallow a large variety of materials that undergo significant structural and chemical changes due to both mastication and mixture with saliva. As the aerodigestive tract is used for both breathing and swallowing, the interface between the bolus and the air must be considered. To further complicate matters, the tongue, soft-palate, pharynx, and larynx all undergo very large deformations during the oropharyngeal phase of swallowing in order

to propel the bolus into the esophagus while preventing aspiration into the lungs and nasal passage. Only a limited number of numerical swallowing simulations in the oropharynx have been performed due to these challenges. This thesis limits its scope to the study of the fluid dynamics of liquid boluses in the oropharynx. It does not explicitly consider the structural and muscular biomechanics of the oral, pharyngeal, and laryngeal complexes.

1.2 Smoothed Particle Hydrodynamics

Smoothed Particle Hydrodynamics (SPH) is a computational fluid simulation method that belongs to the "mesh-free" family of techniques [76]. It excels in simulating transient, free-surface flows because it does not require explicit handling of the fluid-air interface, making it particularly attractive for an oropharyngeal swallowing simulation. One of the main challenges with SPH is the application and enforcement of solid wall boundary conditions. Ghost particles, mirroring, and repulsive force particles are three of the most common techniques for representing solid walls. Of the three, only the repulsive force particles are suitable for handling a complex moving geometry. The repulsive particles line the surface of the solid walls and are effective at preventing the fluids from penetrating the solids. However they are not effective in enforcing the typical "no-slip" boundary condition assumption in viscous fluid simulations.

The Unified Semi-Analytic Wall (USAW) SPH method modifies the original SPH formulation to allow solid walls to be represented by arbitrarily shaped surfaces [32]. The method can handle complex boundary shapes and

is capable of enforcing a "no-slip" condition. However, most of the development focuses on high Reynolds number flows of Newtonian materials such as water. We extend the USAW SPH method to simulate non-Newtonian materials by deriving an equation for estimating shear-rate that includes a new surface integral term. Our implementation also presents a discretized method of handling moving boundaries in 3D. This thesis describes the extended USAW SPH method, and an implementation is tested using canonical flows, such as Hagen-Poiseuille and the lid-driven cavity. We are able to demonstrate convergence of the method in the tested scenarios.

These extensions are necessary for simulating oropharyngeal fluid flow, but are also applicable if USAW SPH is to be used in other applications. For example, in arterial blood flow, shear stress on the inner walls of arteries causes atherosclerosis, plaque formation on the inner walls of the blood vessel, which may lead to a stroke or heart attack [23]. Numerical simulations of the blood flow can predict wall shear stress [13] and neglecting the non-Newtonian properties of blood may significantly influence the simulation results [59, 60]. Arterial walls are sometimes simulated with static geometry, however in reality they are elastic and numerical studies have shown that the displacement of the walls has a significant effect on wall shear stress [82].

1.3 Oropharyngeal bolus simulation with the extended USAW SPH method

We use the extended USAW SPH method to perform a numerical experiment using computer fluid simulation of liquid bolus flow in the oropharynx in order to study saliva's role in swallowing. The experiments utilize geometry derived from state-of-the-art dynamic, 320-row Area Detector Computed Tomography (ADCT) images of human swallowing. The ADCT creates dynamic 3D images that sometimes contain artifacts due to subject or bolus motion, and these images require significant human intervention to process correctly. A new workflow is described that allows for relatively efficient manual extraction of moving boundaries from the ADCT images. The execution of the workflow required the development of a purpose built software tool, *BlendSeg*, which allows an operator to deform a surface mesh while maintaining both the mesh and shape topology.

A small series of experiments, limited in scope to a few human subjects, is performed by using the boundaries generated with *BlendSeg* to drive SPH particles in both slip and no-slip simulations. The boluses swallowed by the participants in the ADCT images are starch-thickened fluids which exhibit non-Newtonian behaviour. Their properties are measured in a rheometer and modelled as a Cross-type fluid using the extended USAW SPH method. We expected to find that the full-slip condition gives a good approximation to normal swallowing because of the presence of the saliva layer, which has a much lower viscosity than the thickened boluses. However, the results indicate that the no-slip condition provides a much better approximation to

the bolus flow, especially with respect to oral containment. On the other hand, we observed an increase in oropharyngeal residue after the swallow when comparing the no-slip to the slip simulation. These findings suggest that saliva does not have a large influence on the speed of the bolus, but it might help to reduce oropharyngeal residue and therefore increase swallowing efficacy, consistent with findings of clinical researchers [106].

The next section lists the contributions presented in this thesis. Chapter 2 describes the anatomy and physiology of swallowing, background in fluid simulation, bolus simulation, SPH, segmentation and modelling from 4D imaging data, and the *ArtiSynth* biomechanics toolkit upon which the work is built. Chapter 3 describes the USAW SPH method and the extensions required to simulate oropharyngeal bolus flow. We validate the simulations by comparison with well-known Couette, Hagen-Poiseuille, and lid-driven cavity flows. Chapter 4 describes a computer fluid simulation of oropharyngeal swallowing using USAW SPH. The geometry motion is based on dynamic 3D ADCT images of healthy participants swallowing starch-thickened boluses. The *BlendSeg* tool is also described in this chapter.

1.4 Contributions

The contributions of this thesis are:

Extension of USAW SPH for oropharyngeal swallowing: The Unified Semi-Analytic Wall (USAW) SPH method is a modern approach to correcting the "particle deficiency" problem inherent in classical SPH for-

mulations for fluid flow. We demonstrate that, with some modification, the method is suitable for fluid simulation of non-Newtonian boluses in the oropharynx. The method was extended to include a formulation for computing shear-rates, which is in turn used to compute an instantaneous viscosity for non-Newtonian fluids. We demonstrate numerical convergence using a lid-driven cavity experiment and Hagen-Poiseuille flows.

Workflow for creating dynamic 3D boundaries from 4D imaging data: We describe a technique for creating dynamic, 3D moving boundaries derived from 4D (3D and time) imaging data. Correctly extracting a suitable boundary from the images requires significant human intervention, and could not be fully automated. We created a tool, *BlendSeg*, that gives a human operator a large degree of control in the creation of a moving boundary that closely follows dynamic 3D volumetric images.

Numerical study examining saliva's role in bolus transport and residue in healthy individuals: These techniques are used to perform a set of 3D oropharyngeal swallowing simulations. We test the performance of both slip and no-slip boundary conditions in normal swallows of starch-thickened liquids. Boundary motion is derived from dynamic 3D images of healthy participants. The numerical predictions are compared to measurements gathered from the source images. The results suggest that in normal individuals saliva does not significantly increase the bolus speed for thickened liquids. However, saliva may help to decrease the quantity of oropharyngeal residue, thereby improving swallowing efficacy. Further inves-

tigation could expand the number of subjects and swallows under analysis, making the findings more clinically relevant.

Chapter 2

Background

This chapter begins with a brief overview of the anatomy and physiology of human swallowing, followed by a review of literature in fluid simulation and Smoothed Particle Hydrodynamics. Previous research performing fluid simulation of the bolus is then reviewed, followed by a review of segmentation of 4D data, and an introduction to the *ArtiSynth* simulation platform.

2.1 Anatomy and physiology of swallowing

Swallowing is a complex process consisting of four phases that are roughly delineated: the preperatory and oral phases, which are voluntary, and the pharyngeal and esophageal, which are involuntary [25]. See Figure 2.1 for a labelling of anatomical structures in the head and neck.

Preparatory and oral phase

During the oral preparatory phase, solids are broken down mechanically by coordinated motion of the tongue, teeth, and cheeks. During this process, saliva is introduced to the food bolus, aiding in the break down of food and beginning the digestion process. For liquids, the oral preparatory phase does not include mastication.

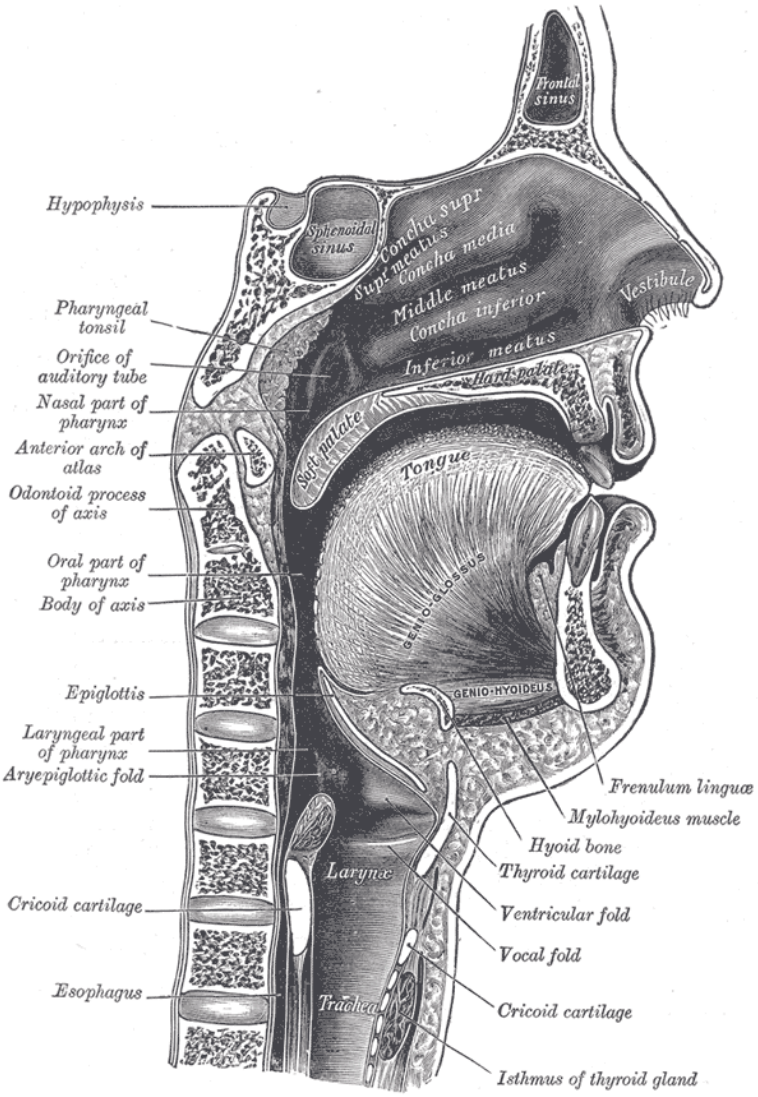

Figure 2.1: An illustrated lateral view of a cut-away human head showing the oral, pharyngeal and laryngeal region with major structures labeled [41].

When the bolus is ready to be swallowed, it is placed in a trough formed on the superior aspect of the tongue. The tip of the tongue touches the back of the upper incisors. The soft palate forms a seal with the postero-superior

aspect of the tongue that contains the bolus, preventing it from leaking prematurely into the pharynx. The swallowing sequence begins with the movement of the soft-palate postero-superiorly to close the nasopharynx. Almost simultaneously, the tongue pushes up towards the palate, creating a travelling wave of pressure [96]. In healthy adults, the closure of the nasopharynx coincincides with the beginning of the stripping wave that propels the bolus into the esophagus [42]. As the tongue moves upwards, the prepared bolus may fall into the pharynx due to gravity, or it may be pushed through due to the motion of the tongue. The superior surface of the tongue continues pushing upwards, exerting pressure on the hard palate and squeezing the tail of the bolus out of the oral cavity and into the pharynx.

Pharyngeal Phase

The pharyngeal phase of swallowing is involuntary, and begins as the bolus enters the oropharynx. It is triggered by touch sensors on the pharynx. As the glossopalatal junction (GPJ) opens and the bolus passes through it, the pharynx is raised by the pharyngeal levator muscles to receive the bolus, while airway protection mechanisms are triggered in order to prevent aspiration of the bolus into the nasopharynx and the larynx. Nasopharyngeal closure is achieved by the soft palate and superior pharyngeal constrictors. Elevation of the tongue base is accompanied by elevation of the hyoid bone and lowering of the epiglottis. The protection of the airway is achieved primarily by closure of the vocal folds in the inferior to superior direction [78]. As the bolus nears the larynx, the arytenoid cartilege begins to close and the epiglottis lowers to a horizontal position. The epiglottis continues to

lower and direct the bolus away from the vocal folds. Pharyngeal peristalsis is achieved through posterior motion of the base of the tongue and the activation of the middle and inferior pharyngeal constrictors. These motions squeeze any remnants of the bolus down towards the esophagus. The pharyngeal phase ends when the bolus reaches the upper esophageal sphincter, which is open to receive the bolus.

Esophageal Phase

Like the pharyngeal phase, the esophageal phase is also involuntary. The esophagus contains rings of constrictor muscles along its length. The constrictor muscles contract sequentially to form another peristaltic wave, triggered by touch sensors lining the esophageal wall, to push the bolus into the stomach. Peristalsis continues as long as there is food within the esophagus.

2.1.1 Imaging of swallowing

Medical imaging is a powerful tool in modern medicine for both clinical practice and research. This section describes very briefly some of the most common imaging methods used in swallowing. Videofluoroscopic (VFL) studies and fibreoptic endoscopic evaluation of swallowing (FEES) are currently being used in diagnostic imaging of dysphagia. In Japan, some researchers have begun using dynamic computed tomography for diagnosis. Other imaging techniques used for swallowing research include magnetic resonance imaging, and ultrasound.

Figure 2.2: Videofluoroscopic image of subject swallowing barium. The posterior of the bolus, contained in the oral cavity, has low image intensity and is visible on the left side of the image. Image by Hellerhoff, distributed under a CC BY 3.0 license [50].

Videofluoroscopic swallowing study

The most common method for diagnostic imaging of swallowing is the videofluorographic (VFL) study, also known as a Modified Barium Swallow (MBS) study. It is the current gold-standard method for clinical diagnosis of dysphagia. The VFL creates and records 2D projections of the subject using x-rays. There is good contrast between bones, soft tissues, and air (see Figure 2.2). Differentiating soft-tissues is challenging as they all appear with similar intensities in the resulting images. Subjects swallow food and liquid mixed with barium, which provides contrast in the VFL images. The work of Martin-Harris et al. [84] attempts to establish a standardized protocol for VFL studies combined with a grading scheme, called the Modified Barium Swallow Impairment Profile (MBSImP).

Fibreoptic Endoscopic Evaluation of Swallowing

Fibreoptic Endoscopic Evaluation of Swallowing (FEES) provides a video image of the pharynx, base of tongue, and larynx through the use of an endoscope inserted through the nasal passage (see Figure 2.3). Although FEES is more invasive than VFL, it is more accessible to clinicians, and does not require the use of ionizing radiation. For swallowing, FEES has been shown to be as sensitive as VFL in detecting premature spillage of the bolus from the oral cavity, residue after the swallow, and laryngeal penetration and aspiration [53].

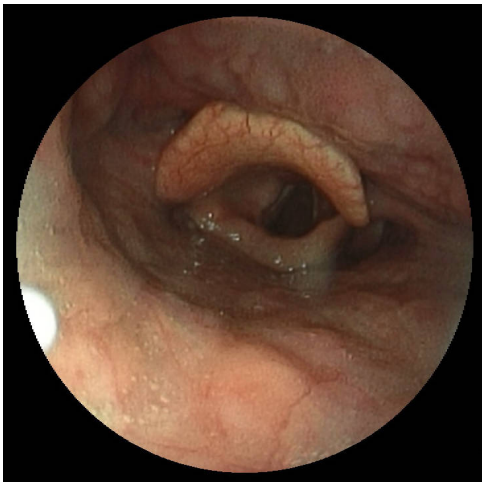

Figure 2.3: Fibreoptic Endoscopic view of the larynx. The epiglottis, base of tongue, pharynx, and glottis are visible. Image by Med Chaos, distributed under a CC BY-SA 3.0 license [16].

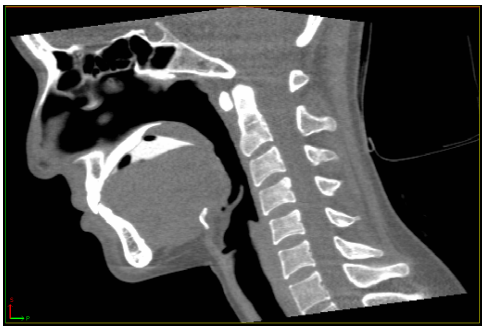

Figure 2.4: 320-row area detector CT mid-sagittal slice of swallowing. 4 ml nectar-thick bolus is visible in the oral cavity with high image intensity. Image courtesy of Fujita Health University [57].

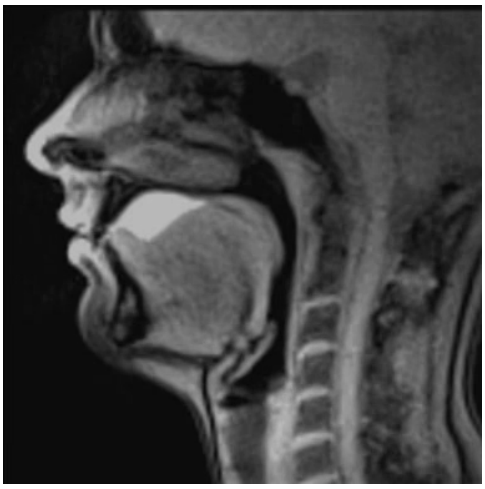

Figure 2.5: Realtime-MRI of mid-sagittal slice of a normal subject swallowing pineapple juice. Image by Martin Uecker, distributed under a CC BY-SA 3.0 license [118].

Dynamic Computed Tomography

Computed Tomography (CT) uses ionizing radiation to create 3D volumetric images. Recently, 320-row Area Detector Computed Tomography (ADCT) has been used to capture dynamic 3D images of swallowing at 10 frames per second [57]. The subject is seated in either a 45° supine or semi-prone position during imaging, and swallows a bolus mixed with barium, similar to a VFL study (see Figure 2.4). Currently, ADCT is the only imaging modality that captures fully 3D and dynamic images at rates sufficient for oropharyngeal swallowing.

Real-time Magnetic Resonance Imaging

Magnetic Resonance Imaging (MRI) uses a magnetic field to excite hydrogen atoms in the body. In response to the magnetic field, the atoms emit

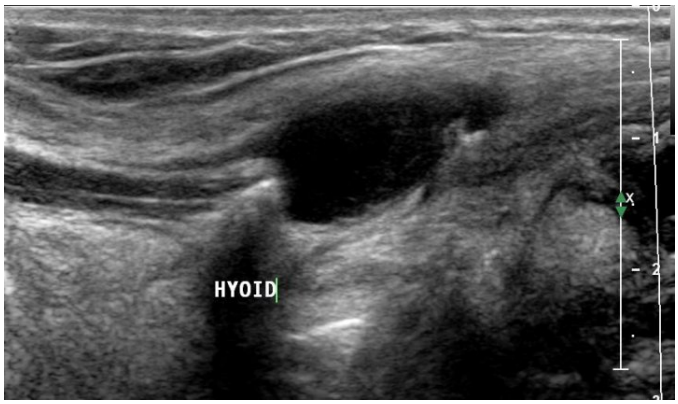

Figure 2.6: Ultrasound image showing sagittal view of hyoid (low image intensity) and thyroglossal duct cyst. Image by Laughlin Dawes, distributed under a CC BY-NC 2.5 license [47].

a signal that is received by the MRI and processed to create 3D volumetric images. Real-time MRI has been used to image healthy subjects swallowing pineapple juice [118, 123] (see Figure 2.5). The sequence captures a single slice at speeds of 24 frames per second. MRI does not involve the use of ionizing radiation, and is a very attractive alternative to VFL and CT. However, it is not yet widely used, perhaps because of its relative inaccessibility compared to VFL and FEES. Some concerns are that it requires the subject to lie in a supine position, which may be dangerous for individuals unable to maintain oral containment of a bolus.

Ultrasound

Ultrasound (US) images have been used successfully in swallowing research, however is not currently used in diagnostic imaging (see Figure 2.6). They are an attractive alternative to VFL and FEES because it is non-invasive and does not use ionizing radiation. US images have been used to image

tongue propulsion of boluses, hyoid motion, pharyngeal motion, and the esophagus [17]. One interesting application of ultrasound is in imaging infants during breastfeeding [38], where it can be used to image a milk bolus passing from a breast or bottle, through the oral cavity, pharynx, and esophagus.

2.1.2 Saliva

Saliva plays an important role in oral health. Decreased salivary flow, or hyposalivation, results in profound deterioration of oral homeostasis, increased susceptibility to dental caries and infections, decreased regulation and control of the oral microflora [114]. Individuals with hyposalivation may also experience impaired swallowing, or dysphagia [34, 100, 103].

Salivary gland hypofunction can be caused by developmental or congenital disorders [28], increased medication usage [113], systemic disorders such as Sjögrens syndrome [35], radiotherapy-induced damage to salivary acinar tissue [51], anxiety [8], and aging [1]. Evidence examining the effect of hyposalivation on swallowing, using an objective assessment method such as videofluoroscopy, suggests that saliva is necessary for lubrication and moistening of the oral mucosa and bolus, and that hyposalivation may affect mastication, bolus formation and transport [43, 105]. A recent study of chemoradiation patients finds a relationship between salivary flow rate and swallowing efficacy [106]. Despite the fact that some of these studies suggest that there is a critical relationship between saliva and swallowing, other findings have failed to show a significant association [111]. For example, a study of patients suffering from Sjögren's syndrome [107], found no

strong correlations between salivary flow rates and bolus transit times. The exact nature of the relationship between saliva and swallowing is still not well understood.

2.2 Fluid simulation

A fluid is any material in a state that continually deforms under shear stress, such as liquids, gasses, and plasmas. In fluid dynamics, the material is assumed to be a continuum even at infinitesimally small scales, ignoring individual molecules and their interactions. Fluids are assumed to obey the laws of conservation of mass, momentum, and energy. In this work, we assume that temperature remains constant throughout a simulation and does not have an impact on the momentum of the fluid, allowing us to ignore the conservation of energy equation. Although all fluids are somewhat compressible, liquid flows at low speeds can be approximated as incompressible, meaning the density is a constant.

When performing fluid simulation, one of the first choices that a modeller needs to make is the method of representing the simulation domain. The optimal choice depends on the problem being studied. For flows with static geometry, for example air moving over an aeroplane wing or through a rigid pipe, static Eulerian discretizations are generally the best choice because they can be solved efficiently and accurately once a mesh is generated [27, 64]. A mesh discretizes the simulation domain with a finite number of small "cells" or "elements" with non-zero volume. Quantities of interest, such as the density, velocity, and pressure, are stored relative to the mesh. For

example, pressure might be stored at the centre of each cell, while velocities might be stored at the middle of a cell wall, or at a cell corner.

An Eulerian discretization is one where the mesh that represents the domain is not changed or moved for the duration of the simulation. For example, a network of weather stations on the ground that measures wind speed, pressure, and temperature tracks these quantities as a function of time at fixed locations, forming an Eulerian representation of the geographical area that they span. A Lagrangian discretization is one where each cell in the mesh always surrounds the same material. As the material moves, the cell walls moves as well so that the same volume of material remains within the cell from the start to the end of the simulation. Lagrangian methods have limited use in fluid simulation because of the large amount of distortion that occurs for many fluid flows. As the mesh distortion increases, cells can become long and thin causing the volume of each cell to approach zero, or even become negative, causing the simulation to become unstable. At this point, the simulation stops and can only continue once the domain is remeshed, and quantities are transferred from the old to the new mesh. Generating a suitable mesh may be a non-trivial problem and, depending on the type of elements used, may require significant manual intervention. Interpolation of variables from one mesh to another may result in undesirable numerical diffusion, an artificial source of damping. If there is only a moderate amount of movement of solid geometry, the Arbitrary-Lagrangian-Eulerian (ALE) technique can accommodate the motion without the need to remesh, while maintaining most of the desirable properties of an Eulerian simulation [26].

Free-surface simulation

Simulating a liquid bolus in the oropharynx is challenging because there are actually two fluids to consider, the bolus and the air, with an unknown interface between them, a so-called free-surface problem. Explicit simulation of the air phase is probably unnecessary for swallowing because of its low density relative to most liquids. Meshed Lagrangian simulations are attractive for free-surface problems because the cell walls of the mesh can be used to represent the free surface. However this approach encounters issues if it reaches a point there is a large amount of movement in the fluid that causes significant mesh distortion. For example, a thin streak of fluid is hard to represent without using an intractable number of elements.

Eulerian simulations have been modified to represent free-surfaces using techniques such as Volume-of-Fluid (VOF) [52, 117], where an additional scalar, between zero and one, representing the fraction of fluid occupying each cell is tracked and advected in addition to the other physical quantities. Level-set techniques [31, 108] work similarly to VOF, but the free surface is represented implicitly as the zero level of a scalar field representing signed distance to the free-surface. Hybrid techniques such as Particle-In-Cell (PIC)/Marker-and-Cell (MAC) [46], Fluid-Implicit-Particle (FLIP) [11, 125] employ a background Eulerian grid and advect discrete particles in order to track the fluid phase.

Moving boundary handling

Another major difficulty of bolus simulation is the moving boundaries in the aerodigestive tract which deform significantly in order to both propel the bolus and protect the airway. This result in parts of the simulation domain collapsing completely and then reopening, making meshing an extreme challenge.

Eulerian methods can be modified to accommodate irregular and moving boundaries using techniques such as Immersed Boundaries [88, 102]. Of these Immersed Boundary techniques, there are those designed for thin filaments [9, 124], which are two-way coupled and must include a model of the solid mechanics, and those for irregular boundaries for which the solids are treated as "rigid" (though they may change position) [29, 65, 90]. Hybrid methods such as PIC/FLIP have been reformulated to handle arbitrarily aligned solids by using a variational formulation to derive a coupled pressure solve [5].

2.2.1 Mesh-free methods

Recently, mesh-free methods have become popular for solving fluid free-surface problems because they can easily handle the fluid-air interface [6]. Their most defining feature is that lack of the mesh-defined connectivity that traditional Lagrangian and Eulerian methods rely on, resulting in a big advantage when there is a moving interface because mesh-free methods do not require remeshing. Mesh-free methods are Lagrangian, as their computation points move with the material, meaning there is no need to

solve for the advection term in the momentum equation, a non-linear term that can be challenging to handle correctly. In general, however, they are computationally more expensive than the traditional meshed methods, and imposition of boundary conditions can be challenging. The increased computational cost is partially offset because mesh-free methods do not require a mesh to be generated.

The oldest and most popular mesh-free method for fluid simulation is Smoothed Particle Hydrodynamics (SPH), which was originally formulated to solve problems in astronomy [40, 80, 91]. Many mesh-free methods have been developed for fluid simulation, such as the Moving Least Squares (MLS) method [7] and Moving Particle Semi-Implicit (MPS) [67, 68], but this work will focus on the SPH method.

2.2.2 Smoothed Particle Hydrodynamics

Smoothed Particle Hydrodynamics (SPH) was first adapted for incompressible free-surface fluid simulation by Monaghan et al. [92]. Typical SPH derivations begin by considering that a smooth function in a domain χ may be reproduced exactly under convolution with the Dirac delta function:

$$f(\mathbf{x}) = \iiint_{\chi} f(\mathbf{x}')\,\delta(\mathbf{x}' - \mathbf{x})\,\mathrm{d}\mathbf{x}' \tag{2.1}$$

The representation is then transformed to a smoothed approximation by replacing the delta function with a "kernel" function, usually a polynomial

approximation to the Gauss function, with local support:

$$\langle f(\mathbf{x})\rangle = \iiint_{\chi} f(\mathbf{x}')\, W(\mathbf{x}' - \mathbf{x}, h)\, \mathrm{d}\mathbf{x}', \tag{2.2}$$

where $W(\mathbf{x}' - \mathbf{x}, h)$ is the kernel function, centered at 0 and scaled by h, a "smoothing length" which determines the extent of the interaction. As h approaches zero, $W(\mathbf{x}, h)$ tends towards the Dirac delta function. The kernel is defined to have local support, so that $W(\mathbf{x}' - \mathbf{x}, h) = 0$ for anything outside of its support domain, Ω. This allows the integral in equation (2.2) to be evaluated over the truncated domain Ω:

$$\langle f(\mathbf{x})\rangle = \iiint_{\Omega} f(\mathbf{x}')\, W(\mathbf{x}' - \mathbf{x}, h)\, \mathrm{d}\Omega. \tag{2.3}$$

Monaghan's first paper [92] applies the SPH equations to the inviscid, incompressible Navier-Stokes equations (the Euler equations). It uses weak compressibility and an artificial speed-of-sound to solve for pressure. An artificial damping term is included to damp pressure oscillations and maintain stability. Special repulsive-force particles are placed along boundaries to prevent SPH particles from passing through solid boundaries. A Newtonian viscosity term was first described by Morris et al. [95], who also describe a surface-tension term [94]. The viscosity term was later validated in 3D by Sigalotti et al. [110]. It has been used for diverse applications such as large wave modelling in dam breaks [71], mud-flows [109], and high-pressure die-casting [18].

Monaghan's damping/stabilization term is capable of adding a signifi-

cant amount of viscous damping (energy loss) to a simulation. The work of Colagrossi et al. [19] use a moving least squares (MLS) filter to smooth density variations in the fluid, and also show that it is applicable for explicit two-phase simulations with high density ratios between the liquid and gas. The MLS filter conserves energy and also reduces the amount of energy loss in Monaghan's damping term. However, this filter was found to disrupt the total volume of fluid for long simulations by Antuono et al [3]. Marrone et al. [83] describe a numerical viscous damping term that, when applied to weakly compressible solvers, smooths the pressure field significantly without adding unwanted viscosity to the flow while also preventing numerical instability.

Non-Newtonian fluids in SPH

Generalized non-Newtonian fluid models are idealized representations of flows where the *apparent* viscosity, represented in this thesis by μ_{eff}, depends only on the shear rate, $\dot{\gamma}$. Some of the common viscosity models include power-law, Herschel-Bulkley, Bingham, and Cross. Non-Newtonian fluids have been modelled with SPH, mostly explicitly. Shao and Lo [109] simulated a Cross fluid to model mud flow. Xu et al. [122] perform a 3D simulation of a Cross fluid to model droplet impacts, thin-plate injection mold, and jet buckling. Hosseini et al. [56] simulate power law, Herschel-Bulkley, and Bingham viscosity models using an explicit solver. Explicit viscosity solvers place a severe time-step restriction on the simulation. The maximum time step size typically depends on the order of Δx^2, while an explicit pressure solve limits time steps to the order of Δx. To make mat-

ters worse, the viscosity time step restriction scales with the inverse of the viscosity. For a power-law fluid at rest, the effective viscosity is infinity. Fan et al. [30] describe an implicit formulation in 2D for the viscosity term in the momentum equation which does not limit the time step size, however it requires solving a large system of equations. For high effective viscosities, this can result in much larger time step sizes and faster simulations, although the cost of solving the each time step is high.

Incompressible SPH formulations

The first truly incompressible SPH method (PSPH) was described by Cummins and Rudman [22]. They use an approach analogous to a "fractional-step" method in meshed techniques, and describe an approximate Laplacian operator, similar to Morris et al.'s viscous diffusion term, to perform an implicit pressure projection. They take a fractional step to advance velocity and then use the divergence of velocity as a source term to solve for the pressure. Boundary handling was performed using reflected particles, with special handling for 90° corners. Contrary to explicit SPH methods, the implicit pressure solve requires an explicit definition of the free-surface boundary so that the zero boundary condition can be applied correctly. Shao and Lo [109] use a symmetric version of Cummins and Rudman's Laplacian operator but use a source term derived from a fractional computation of density instead of divergence of velocity. Their boundary handling used fixed ghost particles instead of fictitious reflected particles. Both of these methods were developed for 2D, and with walls containing 90° degree bends only. It is not obvious how these methods can be extended in general to arbitrary boundary

shapes. Incompressible solvers generally show much smoother pressure contours than weakly-compressible solvers [71], however setting up and solving the pressure projection equation can be time consuming, though this may be offset by the ability to take larger time steps while still remaining stable. Additionally, care must be taken when defining the free-surface interface as this forms a boundary condition in the pressure solve and as such, the pressures are sensitive to this definition.

Insufficient kernel support and the γ correction term

Near solid walls, two problems arise with SPH: applying boundary conditions, and handling the truncated kernel support. The truncated kernel support arises near walls and causes the integral in equation 2.3 to under represent the true value of $f(\mathbf{x})$. Bonet and Kulasagaram re-formulate SPH as an Euler-Lagrange problem and the resulting formulation, in the absence of viscosity, conserves linear and angular momentum. During this process, they introduce a corrective term, γ, into the SPH formulation that corrects for the insufficient kernel support problem [10, 69],

$$\gamma(\mathbf{x}) = \iiint_{\Omega} W(\mathbf{x}' - \mathbf{x}, h)\, \mathrm{d}\Omega, \tag{2.4}$$

which evaluates to unity within the fluid and less than unity when close to a solid wall or free surface. The modified SPH interpolation equation is

$$\langle f(\mathbf{x}) \rangle = \frac{1}{\gamma(\mathbf{x})} \iiint_{\Omega} f(\mathbf{x}')\, W(\mathbf{x}' - \mathbf{x}, h)\, \mathrm{d}\Omega. \tag{2.5}$$

One of the main challenges with this approach is that γ and its gradient are difficult to compute accurately. They address this problem by pre-computing γ and then approximating its value with a spline function based on distance to walls. Special handling is required for corners and irregular geometries.

The Unified Semi-Analytic Wall (USAW) SPH method extends the work of Bonet and Kulasegaram. Ferrand et al. describe an efficient and accurate method for computing γ by describing an analytic solution for $\nabla\gamma$ when using the 5^{th}-order Wendland kernel [32], and solve for γ by integrating it in time along with other physical variables. Leroy et al. extend USAW SPH to solve for pressure implicitly [72], as well as to include a $k-\epsilon$ turbulence model. The USAW methods mentioned so far have only been applicable for 2D solvers. Mayrhofer et al. extend the method to 3D [85]. One of the limitations of the USAW method is that the analytic calulation of $\nabla\gamma$ has only been formulated for the Wendland kernel. Mayrhofer et al. describe a theoretical approach for accomodating moving boundaries in 3D, however they do not describe a discretized approach and application. Additionally, they have not yet adapted their formulation for non-Newtonian materials.

2.3 Fluid simulations of swallowing

Computer simulations of swallowing in the oropharynx has been performed by other researchers in the past, however many of the models were created with simplified geometries of the airway. For example, Chang et al., in [15], model a Newtonian fluid in a axisymmetrized pharynx, from the glossopalatal junction to upper esopahagel sphincter (UES). They use a

finite-element solver on a mesh with prescribed boundary motion, and assume there is no air. The boundary motion is interpolated from the work of Kahrilas et al. [62] and Cook et al. [21], who use bi-plane videofluoroscopy to determine opening diameters of the oropharynx and UES, respectively. Inlet conditions are prescribed by applying a pressure for the duration of GPJ opening, and a velocity estimated from the literature. A pressure of zero is prescribed at the outlet when the UES is open. The authors suggest that this work could be used to predict pressure profiles in the pharynx. This work is extended to 3D in [14] using a K-SNAKE algorithm applied to bi-plane fluoroscopy images, and assuming that pharyngeal cross sections have an elliptical shape. Meng et al. [87] extend the 2D work in [15] by modelling a non-Newtonian power-law fluid instead of a Newtonian fluid.

3D visualization of oropharyngeal swallowing from medical images were created in [61] and [73], as an aggregate of multiple swallows. Their work did not simulate the bolus, but used image data to visualize it.

Nicosia et al. [99] approximate bolus ejection from the oral cavity by simulating two approaching parallel plates in 2D axisymmetric coordinates by solving for the stream and vorticity functions. They used this model to study the pressure required to clear half of the bolus from the oral cavity as viscosity varies. The work was extended in [98] to study the effect of partial-slip boundaries on the shear rates and ejection times of a bolus. In another study by Nicosia [97], an ALE simulation was solved with finite-elements to study oral containment of a bolus on a tongue subject to "lingual pumping" gestures exhibited in some subjects prior to swallowing. The simulation was in 2D and used geometry derived from videofluoroscopic images [62].

Mizunuma et al. [89] used a static CT scan as the basis for creating a realistic 3D geometry of the oral cavity and pharynx. Movement of solids was derived from videofluoroscopic data The solids simulation used finite-elements, and a solid visco-elastic finite element model represented the bolus. Sonomura et al. [112] used similar geometry but replaced the volumetric FE organs with shell elements, and performed a fluid simulation of the bolus using volume-of-fluids to represent both water and a starch-thickened non-Newtonian bolus. Kikuchi et al. [63] use a mesh-free MPS method to simulate the organs and bolus, using structures derived from CT data and motion derived from videofluoroscopic images.

Outside of swallowing itself, mastication has been simulated using SPH by Harrison et al. [48, 49]. They use an elastobrittle SPH material model to represent agar gel and its fracture during mastication.

2.4 Segmentation and modelling from 4D imaging data

Recent advances in dynamic Area Detector CT (ADCT) now allow for 3D and time imaging of dynamic phenomena such as swallowing. The current state of the art uses a 320-row ADCT to capture dynamic 3D images [36, 57]. The amount of detail in these images is stunning, and allows us to study dynamic oropharyngeal swallowing in 3D. A fluid simulation of the liquid bolus in the oropharynx would allow us to study physical phenomena related to swallowing, such as xerostomia (dry-mouth), and how it affects bolus flow.

Commercial software, such as *Amira* or *Mimics*, are not currently ca-

pable of extracting a dynamic surface from 4D CT data that is suitable for simulation. Much of the published literature on 4D segmentation has been focused on the heart, and use model based approaches to identifying structures. McInerney et al. [86] use a model based approach that utilizes an expanding sphere in order to segment the left ventricle and track its motion in 4D. A Finite Element model provides regularizing forces based on stretching and curvature. Montagnat et al. [93] define a 4D simplex-based framework in order to segment the left ventricle. Their framework allows for curvature-based regularization, or a statistical-model-based regularization in both space and time. Some approaches use statistical models that make use of prior knowledge of the shape of the heart and its motion [58, 81], or take advantage of the cyclic nature of the heart beat and use a Fourier analysis [24, 74].

Because the ability to generate 4D images of the airway is so new, to the best of the author's knowledge there has been no work done yet in modelling the airway from 4D CT images. Statistical models can not be leveraged until a sufficiently sized training set has been created. 4D images of oropharyngeal swallowing contain challenges that are not present in images of, for example, the left ventricle. The airway is the void space defined by surrounding organs such as the tongue, hard- and soft-palate, pharynx, and the esophagus. The esophagus is initially closed and pressed flat, typically providing no contrast unless an air bubble is trapped or the bolus is passing through it. It runs parallel and very near to the trachea, which has very strong edges between the airway and the air. During the propulsion phase of swallowing, the oral cavity and pharynx collapse completely, also resulting in very little edge

contrast over large parts of the region. The vocal folds and nasopharynx are also squeezed shut in order to protect the airway. To add further difficulty, the bolus, when stationary, provides ample contrast with surrounding soft tissues, however once it begins to move, its contrast lowers to the point where it has similar intensity to the soft tissues, making edge identification more difficult. Blurring and ghosting artifacts in the images further edge detection methods. Volumetric model based methods that take advantage of physical constraints such as incompressibility can not be used to regularize the segmentation unless all of the organs are registered individually.

2.5 *ArtiSynth* biomechanics toolkit

ArtiSynth is a Java-based toolkit for solving multibody physics problems [77]. It includes a physics library that can perform coupled rigid-body and finite-element simulations, along with complex tasks such as the ability to resolve collisions and solve inverse simulation problems. *ArtiSynth's* main applications are for simulation of biomechanics problems in the human body. It has been used to simulate many anatomical structures and functions such as speech [45], tongue motion [115], face [33], foot [79], and mandibular motion [2]. The SPH model and oropharyngeal swallowing simulations described in this thesis are implemented in *ArtiSynth*. They utilize its graphics rendering capabilities, user interface, vector math library, hierarchical tree representations, and proximity detection methods.

Chapter 3

Smoothed Particle Hydrodynamics for fluid flow

Smoothed Particle Hydrodynamics (SPH) is now a popular method for simulating free-surface flows of liquids. This chapter describes extensions to a state-of-the-art SPH method, the ability to simulate non-Newtonian materials in 3D moving walls, that are necessary for a swallowing simulation. SPH is a Lagrangian method, meaning simulation points remain "fixed" to a material point. The simulation points are referred to as "particles". Movement of a point represents movement of a quanta of material. SPH is a mesh-free method, meaning there is no formally defined connectivity between a particle and its neighbours. Instead, each particle can be thought of as exerting an influence on its neighbours, where the strength of this interaction scales with a "kernel" function.

SPH is most commonly used to represent free-surface flows of high-Reynolds problems, such as dam breaking [83] and sloshing tanks [3]. We believe that with some modification, SPH can be adapted for use in an oropharyngeal swallowing simulation. Its advantages over traditional methods are that it implicitly handles free surfaces and splitting and merging of

fluids without any special handling. This chapter describes the basic formulation of SPH, and the Unified Semi-Analytic Wall (USAW) approach to dealing with solid boundaries. One of the primary contributions of this thesis are extensions to the USAW SPH method to be able to simulate moving walls in 3D, and non-Newtonian fluids. They are described in sections 3.2.2 and 3.2.3, resp. At the end of the chapter, Couette flow, startup Hagen-Poiseuille flow, a lid-driven cavity problem, and non-Newtonian Hagen-Poiseuille flow are simulated with our extended SPH method. The results are compared to theoretical solutions, or in the case of the lid-driven cavity, a canonical solution to the problem. The extended USAW SPH method shows good agreement with accepted solutions, and approximately first-order convergence.

3.1 Classic Smoothed Particle Hydrodynamics formulation

Typical SPH derivations begin by considering that a smooth field in a domain χ may be reproduced exactly under convolution with the Dirac delta function [75, 76]:

$$f(\mathbf{x}) = \iiint_{\chi} f(\mathbf{x}')\,\delta(\mathbf{x}' - \mathbf{x})\,\mathrm{d}\mathbf{x}' \tag{3.1}$$

The representation is then transformed to a smoothed approximation by replacing the delta function with a "kernel" function, usually a polynomial

approximation to the Gauss function.

$$\langle f(\mathbf{x})\rangle = \iiint_{\chi} f(\mathbf{x}')\, W(\mathbf{x}' - \mathbf{x}, h)\, \mathrm{d}\mathbf{x}' \tag{3.2}$$

where $W(\mathbf{x}' - \mathbf{x}, h)$ is the kernel function, centered at 0 and scaled by h, a "smoothing length" which determines the extent of the interaction.

The kernel is defined to have local support, so that $W(\mathbf{x}' - \mathbf{x}, h) = 0$ for anything outside of its support domain, Ω. This allows the integral in equation (3.2) to be evaluated over the truncated domain Ω:

$$\langle f(\mathbf{x})\rangle = \iiint_{\Omega} f(\mathbf{x}')\, W(\mathbf{x}' - \mathbf{x}, h)\, \mathrm{d}\Omega \tag{3.3}$$

The kernel should also be normalized to unity,

$$\int_{\Omega} W(\mathbf{x}' - \mathbf{x}, h) d\mathbf{x}' = 1. \tag{3.4}$$

Spatial discretization is performed by seeding the domain with SPH particles, each having mass and density. The continuous approximation (3.3) is then discretized:

$$(f(\mathbf{x})) = \sum_{b}^{N} f(\mathbf{x_b})\, W(\mathbf{x_b} - \mathbf{x}, h)\, \Delta V_b \tag{3.5}$$

where the summation is over the N particles near $\mathbf{x}$ for which the kernel function W is not equal to 0, and $\mathbf{x}_b$ is the position of neighbour particle b. See Figure 3.1 for a 2-D example. ΔV_b is the volume represented by the neighbour particle, and is defined as the mass divided by density $\Delta V_b = \frac{m_b}{\rho_b}$.

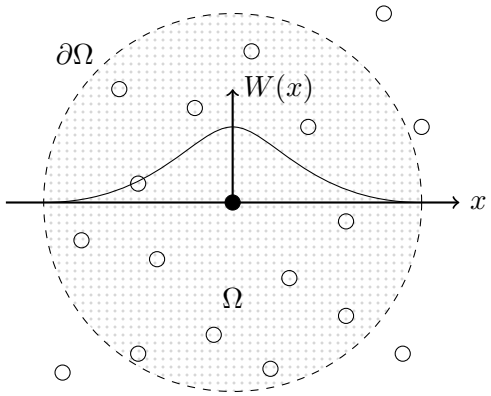

Figure 3.1: Example 2-D particle distribution for an SPH fluid particle (black circle) with full support over its domain Ω (dotted area). The domain boundary is designated by $\partial\Omega$ (dashed circle). A typical 1-dimensional kernel function $W(x)$ is overlaid. Notice that $W(\mathbf{x}) = 0$ for $\mathbf{x} \in \partial\Omega$.

3.1.1 Spatial derivatives

SPH offers a simple method for estimating spatial derivatives. For a divergence,

$$\langle \nabla \cdot f(\mathbf{x}) \rangle = \iiint_{\Omega} [\nabla \cdot f(\mathbf{x}')]\, W(\mathbf{x}' - \mathbf{x}, h)\, \mathrm{d}\Omega \tag{3.6}$$

and after integrating by parts,

$$\langle \nabla \cdot f(\mathbf{x}) \rangle = \iiint_{\Omega} \nabla \cdot \left[f(\mathbf{x}')\, W(\mathbf{x}' - \mathbf{x}, h) \right] \mathrm{d}\Omega - \iiint_{\Omega} f(\mathbf{x}') [\nabla\, W(\mathbf{x}' - \mathbf{x}, h)]\, \mathrm{d}\Omega \tag{3.7}$$

Application of Gauss's (divergence) theorem to the first term of the

right-hand side of this equation yields

$$\langle \nabla \cdot f(\mathbf{x}) \rangle = \oiint_{\partial\Omega} [f(\mathbf{x}')\, W(\mathbf{x}' - \mathbf{x}, h)] \mathrm{d}\mathbf{S} - \iiint_{\Omega} f(\mathbf{x}') [\nabla\, W(\mathbf{x}' - \mathbf{x}, h)]\, \mathrm{d}\Omega \tag{3.8}$$

where $\mathbf{S}$ is the area element in the direction of the face normal.

Since $W(\mathbf{x}' - \mathbf{x}, h)$ is defined to be 0 (see Figure 3.1) on the boundary $\partial\Omega$, the first term is usually dropped, leading to the final gradient approximation:

$$\langle \nabla \cdot f(\mathbf{x}) \rangle = - \iiint_{\Omega} f(\mathbf{x}') [\nabla\, W(\mathbf{x}' - \mathbf{x}, h)]\, \mathrm{d}\Omega. \tag{3.9}$$

The derivative is now applied to the kernel function, defined analytically, and so it is very simple to evaluate. This equation is discretized and summed, as in equation 3.5.

The above assumption holds as long as the fluid integration domain is covered adequately with particles. However, if the fluid domain is truncated by a solid wall, this assumption no longer holds. This is one of the sources of the "particle deficiency" problem.

In practice, the following equivalent forms of the spatial derivatives are discretized since they demonstrate improved stability.

$$\nabla \cdot f(\mathbf{x}) = \frac{1}{\rho} \left[\nabla \cdot (\rho f(\mathbf{x})) - f(\mathbf{x}) \cdot \nabla \rho \right], \tag{3.10}$$

and,

$$\nabla \cdot f(\mathbf{x}) = \rho \left[\nabla \cdot \left(\frac{f(\mathbf{x})}{\rho} \right) + \frac{f(\mathbf{x})}{\rho^2} \cdot \nabla \rho \right]. \tag{3.11}$$

After applying the SPH discretization method, the symmetrized forms

of the derivative appear:

$$(\nabla \cdot f(\mathbf{x}))_a = \frac{1}{\rho_a} \sum_b^N m_b \left(f(\mathbf{x}_b) - f(\mathbf{x}_a)\right) \cdot \nabla W, \tag{3.12}$$

and,

$$(\nabla \cdot f(\mathbf{x}))_a = \rho_a \sum_b^N m_b \left(\frac{f(\mathbf{x}_b)}{\rho_b^2} + \frac{f(\mathbf{x}_a)}{\rho_a^2}\right) \cdot \nabla W, \tag{3.13}$$

3.1.2 SPH for the incompressible, viscous, Navier-Stokes equations

The typical SPH approach to solving the incompressible Navier-Stokes was first presented by Monaghan [92]. Incompressibility is weakly enforced through a stiff equation of state utilizing an artificial speed of sound. For the viscosity term, we use the method described by Morris [95].

For a Lagrangian system, the incompressible Navier-Stokes equations may be written as

$$\frac{D\mathbf{v}}{Dt} = -\frac{1}{\rho}\nabla p + \frac{1}{\rho}\left(\nabla \cdot \mu\nabla\right)\mathbf{v} + \mathbf{B} \tag{3.14}$$

$$\frac{D\rho}{Dt} + \rho\nabla \cdot \mathbf{v} = 0 \tag{3.15}$$

where $\mathbf{v}$ is the velocity, $\frac{D}{Dt}$ is the total derivative, ρ is the density, p is pressure, μ is the Newtonian viscosity, and $\mathbf{B}$ is the body force (e.g. gravity) per unit volume.

We use the following equation of state to relate the density changes to

the pressure [94]:

$$p = c^2 \left(\rho - \rho_0\right), \tag{3.16}$$

where ρ is the density of the current particle, ρ_0 is the reference density of that particle, and c is an artificial speed of sound in the fluid, chosen large enough so that incompressibility is approximately obtained, but small enough so as not to make the time step size too restrictive.

Applying the SPH discretization operator (3.12) to the continuity equation (3.15) yields the formula for updating each particle's density:

$$\frac{D\rho_a}{Dt} = -\sum_b^N m_b \mathbf{v}_{ab} \cdot \nabla W \tag{3.17}$$

where we use $\mathbf{v}_{ab}$ as short-hand for $\mathbf{v}_a - \mathbf{v}_b$. The density of each particle is then updated explicitly.

For the momentum equation, the contribution from the pressure term is computed using equation (3.13):

$$\left(\frac{1}{\rho}\nabla p\right)_a = \sum_b^N m_b \left(\frac{p_a}{\rho_a^2} + \frac{p_b}{\rho_b^2}\right) \nabla W. \tag{3.18}$$

The diffusion term in the momentum equation is evaluated using the method described by Morris [95]:

$$\left(\frac{1}{\rho}(\nabla \cdot \mu\nabla)\mathbf{v}\right)_a = \sum_b^N \frac{m_b(\mu_a + \mu_b)\mathbf{v}_{ab}}{\rho_a \rho_b} \left(\frac{1}{r_{ab}} \frac{\partial W}{\partial r_a}\right) \tag{3.19}$$

where r_{ab} is the distance between particles a and b.

3.1.3 Boundary handling in SPH

When fluids interface with the air, the air pressure is assumed to be zero, and this is handled implicitly by the pressure formulation by the lack of particles representing an air phase [76]. Similarly, shearing forces from the air are assumed to be negligible. These assumptions are reasonable for many applications.

Interfaces with solid walls are much more difficult to handle properly, and their representation in SPH is one of the primary differentiators between different methods. The traditional methods for dealing with solid walls are those of repulsive forces [92], dummy particles [95], and mirror particles [22]. Dummy particles require special placement around irregular boundaries in order to maintain correct densities. Similarly, mirroring requires special handling of corners to maintain a correct particle density. For irregular moving boundaries such as those found in the human body these methods would be unable to correctly represent the solid wall. In this chapter we use repulsive force particles that prevent fluid particles from penetrating into solid walls. They are easily placed along an irregular boundary have no issues with moving geometry. However they are unable to enforce a no-slip boundary condition correctly.

3.1.4 Smoothing pressures with δ-SPH

In order to stabilize an explicit time integration scheme, Monaghan [92] uses an artificial viscosity term that damps vibrations.

$$\Pi_{ab} = \begin{cases} \frac{-\alpha c \overline{\mu}_{ab}}{\overline{\rho}_{ab}}, & \mathbf{u}_{ab} \cdot \mathbf{r}_{ab} < 0 \\ 0, & \text{otherwise} \end{cases} \tag{3.20}$$

where $\overline{\mu}_{ab} = (\mu_a + \mu_b)/2$, $\overline{\rho}_{ab} = (\rho_a + \rho_b)/2$, c is the speed of sound, and α is a parameter that can be tuned based on the simulation. This term is added within the pressure summation term of the momentum update equation. In our experiments we found that this term adds some undesirable viscous damping in addition to numerical damping.

The work of [3] proposes a new damping term that is purely numerical. The method is given the name of δ-SPH [83]. In their work they use fixed boundary particles to represent boundaries. We find that it works well, without modification, with the USAW SPH scheme and produces relatively smooth pressure distributions even with an explicit solver and a high speed of sound. In our experiments it stabilizes the simulation without adding a significant amount viscous damping, and therefore replaces Monaghan's damping term entirely.

The δ-SPH method adds additional damping terms to the SPH update equations,

$$\mathbb{D}_a^{\rho} = \xi h c \sum_b^N \frac{m_b}{\rho_b} \psi_{ab} \cdot \nabla W, \tag{3.21}$$

$$\mathbb{D}_a^p = \alpha h c \rho_a \sum_b^N \frac{m_b}{\rho_b} \pi_{ab} \nabla W, \tag{3.22}$$

where the terms $\mathbb{D}_a^\rho$ and $\mathbb{D}_a^p$ are added to the density and momentum updates for particle a, respectively, c is the speed of sound, and h is the kernel smoothing length. ξ and α are constants that that control the amount of damping. In our experiments, both are set to 0.02, and with some informal testing we found that simulation results are not sensitive to this choice. ψ_{ab} and π_{ab} are defined as

$$\psi_{ab} = 2(\rho_b - \rho_a) \frac{\mathbf{r}_b - \mathbf{r}_a}{|\mathbf{r}_b - \mathbf{r}_a|^2}, \tag{3.23}$$

$$\pi_{ab} = \frac{(\mathbf{u}_b - \mathbf{u}_a) \cdot (\mathbf{r}_b - \mathbf{r}_a)}{|\mathbf{r}_b - \mathbf{r}_a|^2}, \tag{3.24}$$

3.2 Unified Semi-Analytic Wall SPH

This section briefly describes the evolution from the classic SPH formulation to the Unified Semi-Analytic Wall (USAW) method of boundary handling [32, 72, 85]. We demonstrate how 3D moving boundaries, such as those found in the airway, can be simulated using the USAW SPH method. Next, we present a formulation for non-Newtonian viscosities using USAW SPH.

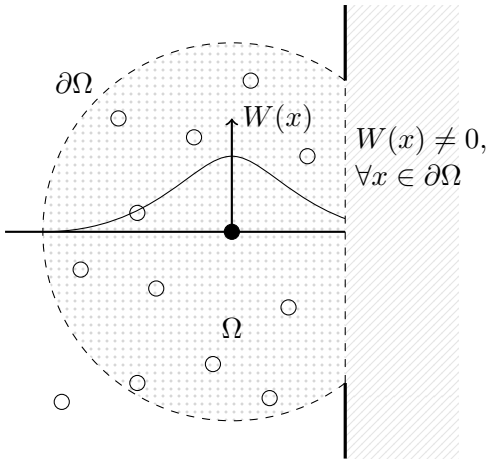

Figure 3.2: Example particle distribution for an SPH fluid particle (black circle) with truncated support over its domain Ω (dotted area). The domain boundary is designated by $\partial\Omega$ (dashed circle). A typical 1-dimensional kernel function $W(x)$ is overlaid. Notice that unlike Figure 3.1, $W(\mathbf{x}) \neq 0$ for $\forall \mathbf{x} \in \partial\Omega$.

3.2.1 Solid boundaries and insufficient domain representation

The truncated support domain causes two problems in the SPH approximation, the first is that the kernel is no longer normalized, and the second is that the value of the kernel on the boundary is no longer zero, and so the boundary terms can not be dropped. Bonet and Kulasegaram address the first issue in [10, 69] by beginning from a variational formulation for a particle system and introducing a scaling term to 3.2 the interpolation equation by γ, a renormalization factor.

$$\langle f(\mathbf{x}) \rangle = \frac{1}{\gamma} \iiint_{\chi} f(\mathbf{x}')\, W(\mathbf{x}' - \mathbf{x}, h)\, \mathrm{d}\mathbf{x}', \tag{3.25}$$

$$\gamma = \int_{\Omega} W(\mathbf{x}' - \mathbf{x}, h) d\mathbf{x}' \tag{3.26}$$

However the computation of γ is non-trivial and an accurate method of evaluation is required. Their variational formulation leads to a new term in the pressure equation that accounts for boundary forces, which includes a derivative of γ term.

Ferrand et al. [32] reformulate the boundary force term ($\nabla\gamma$) and their group further expand the method to include turbulence, a 2D truly incompressible pressure solve [72], and into 3D [85]. Much of the challenge is in finding an accurate and efficient method for evaluating γ and $\nabla\gamma$.

The density and momentum updates, equations (3.17 - 3.19), have had their boundary terms dropped due to the assumption that the kernel-function $W(\mathbf{x}' - \mathbf{x}, h)$ is nil on the boundaries. This assumption is true for fluid particles that are far from a wall, but does not hold near solid boundaries (see Figure 3.2). The equations (3.12 - 3.13) are re-written here with the surface terms and renormalization terms included:

$$\begin{aligned}(\nabla \cdot f(\mathbf{x}))_a = \frac{1}{\gamma_a \rho_a} \sum_b^N m_b \left(f(\mathbf{x}_b) - f(\mathbf{x}_a)\right) \cdot \nabla W \\ - \frac{1}{\gamma_a \rho_a} \sum_k^K \rho_k \left(f(\mathbf{x}_k) - f(\mathbf{x}_a)\right) \cdot \mathbf{n} W \Delta S\end{aligned} \tag{3.27}$$

$$(\nabla \cdot f(\mathbf{x}))_a = \frac{\rho_a}{\gamma_a} \sum_b^N m_b \left(\frac{f(\mathbf{x}_b)}{\rho_b^2} + \frac{f(\mathbf{x}_a)}{\rho_a^2} \right) \cdot \nabla W - \frac{\rho_a}{\gamma_a} \sum_k^K \left(\frac{f(\mathbf{x}_k)}{\rho_k} + \rho_k \frac{f(\mathbf{x}_a)}{\rho_a^2} \right) \cdot \mathbf{n} W \Delta S \quad (3.28)$$

where the second term on the right-hand side of each equation is the boundary term, K is the set of boundary elements that intersect the sphere of influence, Ω, of particle a, $\mathbf{x}_k$ is the centroid of the surface element k, $\mathbf{n}$ is the unit-normal perpendicular to the surface element k, and ΔS is the magnitude of the area of the surface element.

These modified boundary terms are applied to equations (3.17) and (3.18), the density update equation and pressure term of the momentum equation, respectively.

$$\frac{D\rho_a}{Dt} = -\frac{1}{\gamma_a} \sum_b^N m_b \mathbf{v}_{ab} \cdot \nabla W + \frac{1}{\gamma_a} \sum_k^K \rho_k \mathbf{v}_{ak} \cdot \mathbf{n} W \Delta S \quad (3.29)$$

$$\left(\frac{1}{\rho} \nabla p \right)_a = \frac{1}{\gamma_a} \sum_b^N m_b \left(\frac{p_a}{\rho_a^2} + \frac{p_b}{\rho_b^2} \right) \nabla W - \frac{1}{\gamma_a} \sum_k^K \left(\rho_k \frac{p_a}{\rho_a^2} + \frac{p_k}{\rho_k} \right) \cdot \mathbf{n} W \Delta S \quad (3.30)$$

The same procedure can be applied to the diffusion term (3.19) and the following equation is obtained:

$$\left(\frac{1}{\rho} (\nabla \cdot \mu \nabla) \mathbf{v} \right)_a = \frac{1}{\gamma_a} \sum_b^N \frac{m_b (\mu_a + \mu_b) \mathbf{v}_{ab}}{\rho_a \rho_b} \left(\frac{1}{r_{ab}} \frac{\partial W}{\partial r_a} \right) - \frac{1}{\gamma_a \rho_a} \sum_k^K (\mu_a + \mu_k) W (\nabla \mathbf{v} \cdot \mathbf{n})_k \Delta S. \quad (3.31)$$

Evaluating equations (3.29 - 3.31) requires for the velocity gradient dotted with the surface normal ($\nabla \mathbf{v} \cdot \mathbf{n}$), for each surface element k. The next section discusses how this estimate is computed.

Estimating velocity gradient at the wall

The computation of the velocity gradient is not trivial due to the fact that particle distributions may be sparse and irregular. Consider the case where only one particle is near enough to a boundary element to influence it; there is inadequate information to compute the full tensor $\nabla \mathbf{v}$. However, note that the full gradient is not required in equation (3.31), and that it only contributes to the viscous term after being multiplied by the surface normal, $\nabla \mathbf{v} \cdot \mathbf{n}$.

In the viscous formulation by Morris for fluid particles, the velocity gradient is only evaluated in the relative direction between the two particles. A finite-difference approximation gives a good estimate for this quantity. After transforming the integral using the divergence theorem, the term that appears is $\nabla \mathbf{v} \cdot \mathbf{n}$. Using the finite-difference approach for the boundary terms would work for flat and concave boundaries, such as plane Couette flow and Hagen-Poiseuille flow. However it would be unstable for boundaries with convex curvatures, such as over a sphere or a bluff body. This instability arises because there is not enough information to give a good estimate for $\nabla \mathbf{v} \cdot \mathbf{n}$ when the surface normal and relative position vectors are perpendicular or near-perpendicular (see Figure 3.3).

To overcome this difficulty, it is assumed that for any fluid particle a, $\nabla \mathbf{v} \cdot \mathbf{n}$ is constant over the surface area under integration. It is defined by

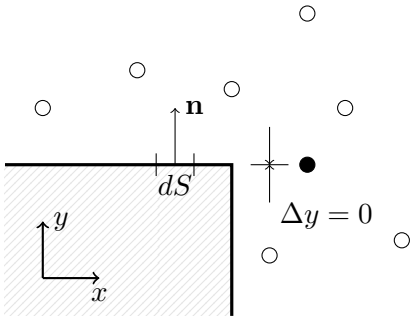

Figure 3.3: This figure illustrates the difficulty in getting an estimate for $\nabla \mathbf{v} \cdot \mathbf{n}$ for the differential surface element dS, using a fluid point (filled circle) perpendicular to the surface normal, $\mathbf{n}$. This situation occurs for geometries where the fluid is contained in a non-convex boundary. There is inadequate information to estimate any shear components since Δy between dS and the fluid particle is nil.

using the point on the solid surface which is closest to a, denoted $\mathbf{r}_g$, and by assuming the surface normal at $\mathbf{r}_g$ is in the direction of $\mathbf{r}_{ag}$ (see Figure 3.4). The following formula is then used:

$$(\nabla \mathbf{v} \cdot \mathbf{n})_a = \left[\frac{1}{r_{ag}} \mathbf{v}_{ag} \otimes \mathbf{n}_g \right] \cdot \mathbf{n}_g \tag{3.32}$$

$$\mathbf{n}_g = \frac{\mathbf{r}_{ag}}{r_{ag}}. \tag{3.33}$$

Equation (3.32) simplifies to:

$$(\nabla \mathbf{v} \cdot \mathbf{n})_a = \frac{1}{r_{ag}} \mathbf{v}_{ag}, \tag{3.34}$$

which is simply the finite difference approximation of the velocity gradient in the direction of particle a from point g using reflective boundary conditions.

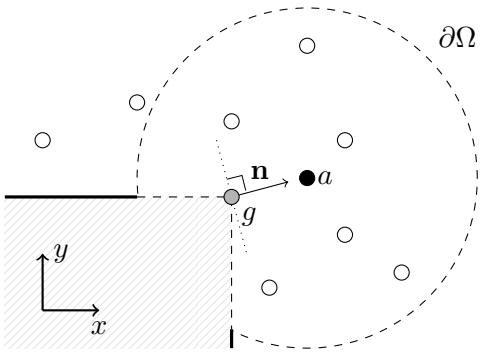

Figure 3.4: The vector $\nabla\mathbf{v}\cdot\mathbf{n}$ is assumed to be constant over $\partial\Omega$ for a fluid particle a where it is truncated by the wall. To compute $\nabla\mathbf{v}\cdot\mathbf{n}$, the point on the wall nearest to a, denoted g and indicated with a grey circle, is used in the computations. Additionally, it is assumed that the normal $\mathbf{n}$ points from g to a. This assumption is good near solid walls with low curvature, but gives the appearance of a "smoothed" wall near sharp, convex corners.

This approximation results in the following viscous term being used:

$$\left(\frac{1}{\rho}(\nabla\cdot\mu\nabla)\mathbf{v}\right)_a = \frac{1}{\gamma_a}\sum_b^N \frac{m_b(\mu_a+\mu_b)\mathbf{v}_{ab}}{\rho_a\rho_b}\left(\frac{1}{r_{ab}}\frac{\partial W}{\partial r_a}\right) - \frac{1}{\gamma_a\rho_a}\left(\frac{1}{r_{ag}}\mathbf{v}_{ag}\right)_a \sum_k^K (\mu_a+\mu_k)\, W\Delta S \quad (3.35)$$

This scheme has the added benefit of being computationally efficient, since $(\nabla\mathbf{v}\cdot\mathbf{n})_a$ is only evaluated once for each particle in the vicinity of a solid wall, as opposed to being evaluated for each differential surface element in the vicinity of the particle.

Surface discretization

When using a triangular mesh to represent a solid boundary, the triangles may not be of a similar size to the inter-particle spacing. Triangles that

are much smaller than the particle spacing do not pose an issue except that evaluating surface integrals may be inefficient. If triangles are much larger than the particle spacing, a pre-processing step can be performed checking each triangular element for size. If the length of the longest edge is larger than the initial particle spacing, the triangle is subdivided into four smaller triangles. This process is repeated recursively until none of the elements has any edge longer than the initial particle spacing. The centre of each sub-element is used in distance computations to fluid particles; that is, a triangle's area may be excluded from surface integration if the barycentric centre of the triangle is too far from a particle, even if some part of the triangle does lie within the fluid particles' sphere of influence Ω. Conversely, a triangle's full area may be included in the computation even though some of it may fall outside of Ω. This results in the method having some sensitivity to the quality of the surface discretization.

Care must also be taken when defining the initial distribution of fluid particles. Each SPH fluid particle can be considered as representing a volume of fluid, with volume $dV = m/\rho$. One edge of this volume of fluid is typically the plane halfway between this particle and its nearest immediate neighbour. With this in mind, particles adjacent to a wall should initially be placed away from the wall at a distance of half the initial spacing between particles. If one is not careful, an incorrect volume of fluid may be created. Placing particles on the surface of the mesh can alleviate this issue, however for irregular meshes that deform, this method may not be suitable.

3.2.2 Moving boundaries in 3D

The work of Mayrhofer et al. [85] extends the USAW SPH method to three dimensions. The main challenge is the evaluation of the $\nabla\gamma$ term in 3D. They demonstrate an analytical method for determining $\nabla\gamma$, however it requires the use of the 5^{th} order Wendland kernel [120]. In order to evaluate γ at a time t, γ can be initialized at time zero and then integrated numerically as the particle moves through the $\nabla\gamma$ field. Beginning with the following identity, which can be derived from the chain rule,

$$\int_{t_n}^{t_{n+1}} \frac{d\gamma}{dt}\, dt = \int_{t_n}^{t_{n+1}} \nabla\gamma \cdot \mathbf{u}\, dt, \tag{3.36}$$

$$\gamma(t_{n+1}) - \gamma(t_n) = \int_{\mathbf{x}_n}^{\mathbf{x}_{n+1}} \nabla\gamma \cdot d\mathbf{x}, \tag{3.37}$$

where γ follows the material point. This formulation assumes walls are static, e.g. for a static particle with a wall approaching it, $d\mathbf{x}$ is zero however $\gamma(t_n) \neq \gamma(t_{n+1})$. Mayrhofer et al. briefly describe a possible approach to the solution of γ when walls are moving, and here we present our discretized implementation,

$$\mathbf{x}_{n+1/2} = \mathbf{x}_n + \frac{1}{2}(\mathbf{u}_a(t_n) - \mathbf{u}_m(t_n))dt \tag{3.38}$$

$$\gamma_a(t_{n+1}) - \gamma_a(t_n) = \sum_k^K \nabla\gamma(\mathbf{x}_{n+1/2}) \cdot (\mathbf{u}_a(t_n) - \mathbf{u}_k(t_n))\, dt, \tag{3.39}$$

where a is the particle under consideration, k is a triangular surface element in the set K that are close to particle a.

This method has been implemented in ArtiSynth and simulations are able to run stably with moving, irregular boundaries while maintaining stability and good approximations of γ. For time-integrated quantities, numerical drift can present an issue. In these cases, re-initialization of γ explicitly is possible. In our implementation, particles that are far from any solid walls have their γ value forced to either 0 or 1, depending on whether it is inside or outside a containing geometry. This step effectively "re-initializes" γ so that numerical drift does not become an issue even for long running simulations. For instance, simulation times of 30–60 s were used for the lid-driven cavities presented later in this chapter and drift of γ is never an issue.

3.2.3 Non-Newtonian fluids in USAW SPH

Until now, the USAW SPH method has only described flow for Newtonian boluses. Previous SPH simulations for non-Newtonian flows use static boundary particles to represent solid walls, for example [30, 56, 109, 122]. However, static boundary particles are not easy to define for irregular boundaries, and deforming boundaries may change the boundary particle distribution in unpredictable ways causing errors in the SPH integral.

Here we present a USAW SPH method for explicitly integrated non-Newtonian flow, extending the work of [122]. The main challenge is to evaluate the shear-rate, $\dot{\gamma}$, from which an effective viscosity $\mu_{\text{eff}}(\dot{\gamma})$ can be computed using one of many models such as power-law, Cross, or Herschel-Bulkley.

Applying the SPH formulation to the velocity gradient for a particle i yields the following definition for its components:

$$k_a^{\alpha\beta} = \left(\frac{du^\alpha}{dx^\beta}\right)_a = \sum_b^N \frac{m_b}{\rho_b}(u_b^\alpha - u_a^\alpha)\frac{\partial W_{ab}}{\partial x^\beta}, \tag{3.40}$$

where $\alpha, \beta \in \{0, 1, 2\}$, and x^α, u^β are the components of position and velocity in the α and β directions, resp. W_{ab} is shorthand for $W(\mathbf{x}_b - \mathbf{x}_a, h)$. In 3D the shear rate is defined as

$$\dot{\gamma} = \sqrt{2 \text{ tr}(d^{\alpha\beta} \cdot d^{\beta\alpha})}, \tag{3.41}$$

$$d^{\alpha\beta} = \frac{1}{2}\left(\frac{du^\alpha}{dx^\beta} + \frac{du^\beta}{dx^\alpha}\right). \tag{3.42}$$

$$\dot{\gamma}_a = \left[2((k_a^{00})^2 + (k_a^{11})^2 + (k_a^{22})^2) + (k_a^{10} + k_a^{01})^2 + (k_a^{20} + k_a^{02})^2 + (k_a^{21} + k_a^{12})^2\right]^{1/2}. \tag{3.43}$$

Extending the definition for USAW SPH requires including boundary terms into $k_a^{\alpha\beta}$. For the typical USAW SPH derivation, the following expression is obtained,

$$k_a^{\alpha\beta} = \left(\frac{du^\alpha}{dx^\beta}\right)_a = \frac{1}{\gamma}\sum_b^N \frac{m_b}{\rho_b}(u_b^\alpha - u_a^\alpha)\frac{\partial W_{ij}}{\partial x^\beta} - \frac{1}{\gamma}\sum_k^K (u_k^\alpha - u_a^\alpha) n^\beta W_{im}\Delta S, \tag{3.44}$$

where n^β is the β^{th} component of the wall normal. This definition can be used in equation 3.43 in order to produce the correct shear rate using USAW

boundaries.

3.2.4 Time integration

The simulation is initialized at time zero by seeding the domain with particles and assigning initial values to velocity, density, γ. We use a semi-implicit Euler time integration scheme to advance the simulation. In order to advance a simulation from time t_n to t_{n+1},

while $t_n < t_{\text{end}}$ **do**

$\mathbf{U}_{n+1} = \mathbf{U}_n + \Delta t \cdot F(\mathbf{X}_n, \mathbf{R}_n, \mathbf{\Gamma}_n, \mathbf{U}_n)$

$\mathbf{R}_{n+1} = \mathbf{R}_n + \Delta t \cdot D(\mathbf{X}_n, \mathbf{R}_n, \mathbf{\Gamma}_n, \mathbf{U}_{n+1})$

$\mathbf{X}_{n+1} = \mathbf{X}_n + \Delta t \cdot \mathbf{U}_{n+1}$

$\mathbf{\Gamma}_{n+1} = \mathbf{\Gamma}_n + \Delta t \cdot G(\mathbf{X}_{n+1})$

$t_{n+1} = t_n + \Delta t$

end while

where $\mathbf{U}_n$, $\mathbf{X}_n$, $\mathbf{R}_n$, and $\mathbf{\Gamma}_n$, are the vectors of all particle velocities, positions, densities, and γ, respectively, at time n. The function F computes the rate of change of velocities, D the rate of change of densities, and G the rate of change of γ. Δt is the timestep $t_{n+1} - t_n$.

3.3 Verification and validation

The USAW SPH method described in this chapter was implemented entirely in Java, as part of the *ArtiSynth* multibody simulation platform [77]. It is used to simulate four viscous flows with known solutions: Couette flow between two parallel planes, Hagen-Poiseuille startup flow in a cylin-

der, lid-driven cavity flow, and steady-state Hagen-Poiseuille flow for a non-Newtonian fluid. For the Couette and Hagen-Poiseuille flows, theoretical transient and steady-state solutions are known [121]. For the lid-driven cavity flows, our results are compared to those computed by Ghia et al. in [39].

Fluid particles were initialized with zero velocity, and mass equal to the fluid density (initially constant throughout the domain) multiplied by the differential volume they occupy (e.g. $dV = dx\,dy\,dz$ or in the case of cylindrical coordinates, $dV = r\,\sin\phi\,d\phi\,dr\,dz$).

3.3.1 Couette flow

In the first flow regime, two infinitely large, solid planes are parallel to each other, with the bottom plane at $z = 0$ having velocity $\mathbf{0}$, and the top plane at $z = 1$ having velocity $1\,\hat{\mathbf{i}}$. The space between the planes is filled with viscous fluid with $\nu = \frac{\mu}{\rho} = 1$. At steady state, the theoretical solution for velocity in the fluid is simply proportional to the height above the stationary plane. For $\mathbf{x} = (x, y, z) = x\hat{\mathbf{i}} + y\hat{\mathbf{j}} + z\hat{\mathbf{k}}$,

$$\mathbf{v}(\mathbf{x}) = z\hat{\mathbf{i}}. \tag{3.45}$$

For this simulation, particles were arranged in a regular lattice, with spacing size of 0.1 between particles. The planes were actually size 2×2, and velocity samples were taken for a single column of particles near the centre of the plane. The simulation was driven by the top plane's assigned velocity.

For the Couette flow, the theoretical solution is recovered almost exactly

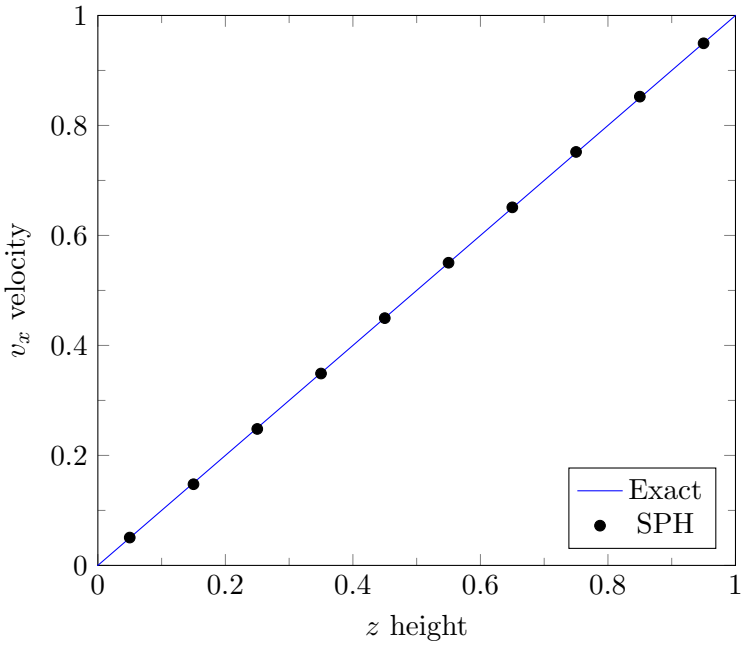

Figure 3.5: Simulation results vs. exact solution for Couette flow between two parallel planes. Ten particles span the distance between the top and bottom planes.

even at low resolution, with only 10 particles spanning the channel (see Figure 3.5). This simulation tests only the viscous part of the update, since density updates and pressures are not used in finding the solution. In deriving the viscous term over the boundary, the assumption was made that $\nabla\mathbf{v}\cdot\mathbf{n}$ is constant over the intersection of the surface with a particles support sphere. This holds exactly for this simple case. The assumption involving the face normal direction is also true for this case.

3.3.2 Startup Hagen-Poiseuille flow for a Newtonian fluid

The second flow, Hagen-Poiseuille flow in a circular pipe, is driven by a uniform pressure differential inside the pipe. The pipe geometry is defined with its axis aligned with $\hat{\mathbf{k}}$, with radius $R = 1$, and a fluid with $\nu = 1$ driven by a pressure differential equivalent to an acceleration of $1\hat{\mathbf{k}}$.

The exact time dependent solution of laminar, fully-developed Hagen-Poiseuille flow is given by the infinite series:

$$v_z(r,t) = \frac{|\mathbf{B}|}{4\nu}(r^2 - R^2) + \sum_{m=1}^{\infty} \frac{|\mathbf{B}|R^2}{\nu\alpha_m^2} \frac{J_2(\alpha_m)}{J_1^2(\alpha_m)} J_0\left(\frac{r\alpha_m}{R}\right) exp\left[-\frac{\nu\alpha_m^2 t}{R^2}\right], \tag{3.46}$$

where v_z is the axial component of the velocity, r is the distance from the axial centre of the pipe, t is the time, and the pipe radius is R. $\nu = \frac{\mu}{\rho}$ is the dynamic viscosity. J_n are Bessel functions of the first kind with order n, and α_m is the m^{th} root of $J_0(kr)$. $\mathbf{B}$ is the pressure force driving the flow, a body force in our simulations. In the limit as $t \to \infty$, the steady state solution is reached,

$$v_z(r) = \frac{|\mathbf{B}|}{4\nu}(r^2 - R^2) \tag{3.47}$$

Particles were distributed regularly in the $\hat{\mathbf{k}}$ direction, and radially in the direction perpendicular to the flow (see Figure 3.6 for an example of the distribution used in a moderate-resolution simulation). Care was taken to initialize the particle positions to the centroid of the differential volume element they are supposed to represent. The simulation was driven by a body force in the axial direction of the pipe and evolved in time until the

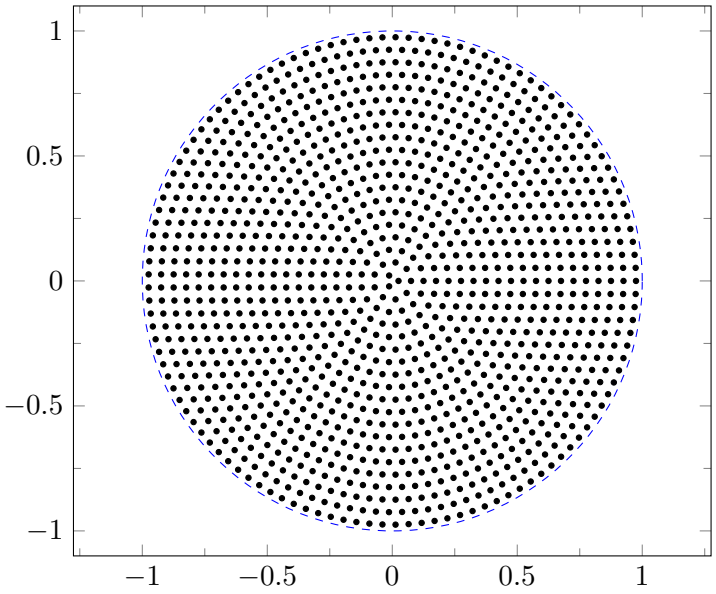

Figure 3.6: Particle distribution for Hagen-Poiseuille in a plane perpendicular to the flow direction for initial spacing of approximately 0.05. The tube wall is shown as a dashed circle.

simulation reached a steady state. Periodicity was enforced with a method similar to [110], where *master* particles near the outlet of the pipe have their densities, velocities, and pressures copied to their corresponding *slave* particles near the inlet. A similar but opposite scheme is used to enforce periodicity at the outlet.

For this experiment, the velocities for half of a single row of particles spanning the diameter of the pipe are reported. Figure 3.8 shows the simulation predictions plotted against the transient solutions for both moderate- and high-resolution simulations. The predicted velocities show excellent agreement with the transient solution, even at moderate resolutions.

Table 3.1 shows the L_2 Error for a slice of particles perpendicular to

the flow direction and in the centre of the simulated pipe. The simulation appears to be converging to the correct solution at an approximately first-order rate (see Figure 3.7).

Approx. Spacing	L_2 Error	Apparent Conv. Rate
0.1	1.01978×10^{-3}	–
0.05	3.00186×10^{-4}	1.76433
0.025	2.38488×10^{-4}	0.33194
0.0125	1.25535×10^{-4}	0.92583

Table 3.1: L_2 Error and apparent convergence for Hagen-Poiseuille flow simulation. Samples were for a slice of particles near the centre of the pipe perpendicular to the flow direction.

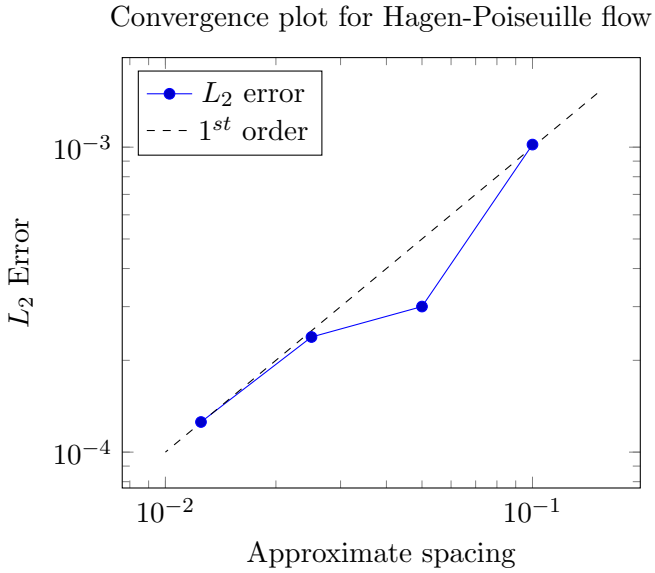

Figure 3.7: The rate of convergence for Hagen-Poiseuille flow appears to be approximately first-order.

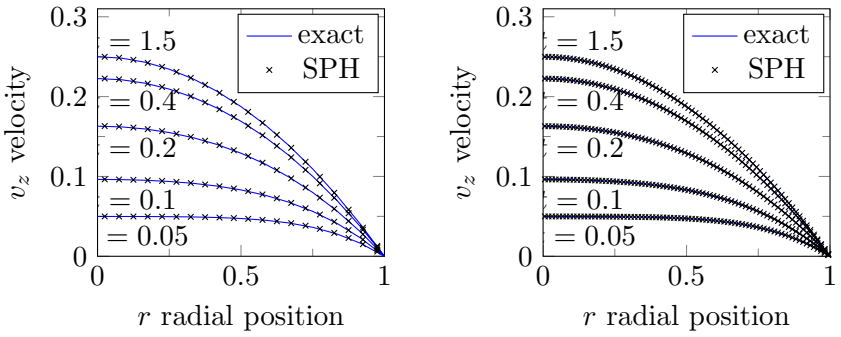

Figure 3.8: Hagen-Poiseuille flow simulation vs exact solution for the moderate (a) and high (b) resolution spacing. For the moderate resolution simulations, the particle spacing is approximately 0.05 and 40 particles span the pipe diameter. For the high resolution simulations the particle spacing is approximately 0.0125 and 160 particles span the diameter. Only half of the pipe is shown due to symmetry.

3.3.3 Lid-driven cavity

The third flow is the classic lid-driven cavity experiment. We solve a pseudo-2D problem where all of the kernels and solid geometries are 3D, but the computational SPH particles are only distributed in a single plane. Out-of-plane particles are simply duplicates of the computation particles, offset by a distance equal to the initial particle spacing. In total, 8 out-of-plane particles were created for each computation particle: 4 on either side. In order to compensate for small, out of plane velocities and displacements accumulating for each particle, every computation particle had the out-of-plane component of its position and velocity clamped to zero every 100 time steps.

In our tests, a box with size 1×1 was created, with a velocity of 1 on

the top boundary. The density of the fluid was set to 1000, and Reynolds numbers of 100 and 1000 were simulated for 30 and 60 time units, respectively.

Streamlines results are generated with *Paraview* using the *pv-meshless* plugin for SPH flows. Figure 3.10 shows the streamlines predicted by SPH after steady-state has been achieved. The steady-state velocity profiles through the horizontal and vertical centres of the cavity show good agreement with the results reported by Ghia et al. [39] (see Figure 3.9). The predicted location of the centre of the primary vortex was within one grid cell of the results reported in [39] (grid cell sizes are defined by Ghia et al.). For Re = 100, secondary and tertiary vortices appeared and disappeared frequently during the transient stage, but were not present after steady-state had been reached. For Re = 1000 the bottom right vortex was present at steady-state and the location also matched well with that reported by Ghia et al. In order to test that the results were "grid-converged", the Re = 100 simulation was run with a 200×200 particle distribution with only small differences in both the velocity profiles, centre of main vortex, and streamline shapes. The L_2-norm of the difference in velocity profiles is less than 1%.

3.3.4 Non-Newtonian Hagen-Poiseuille flow

The Hagen-Poiseuille flow can also be run for non-Newtonian boluses. We test the shear-rate estimate (equation 3.44) by simulating a power-law fluid, for which an analytical solution of the velocity profile at steady-state is known for flow in a circular pipe.

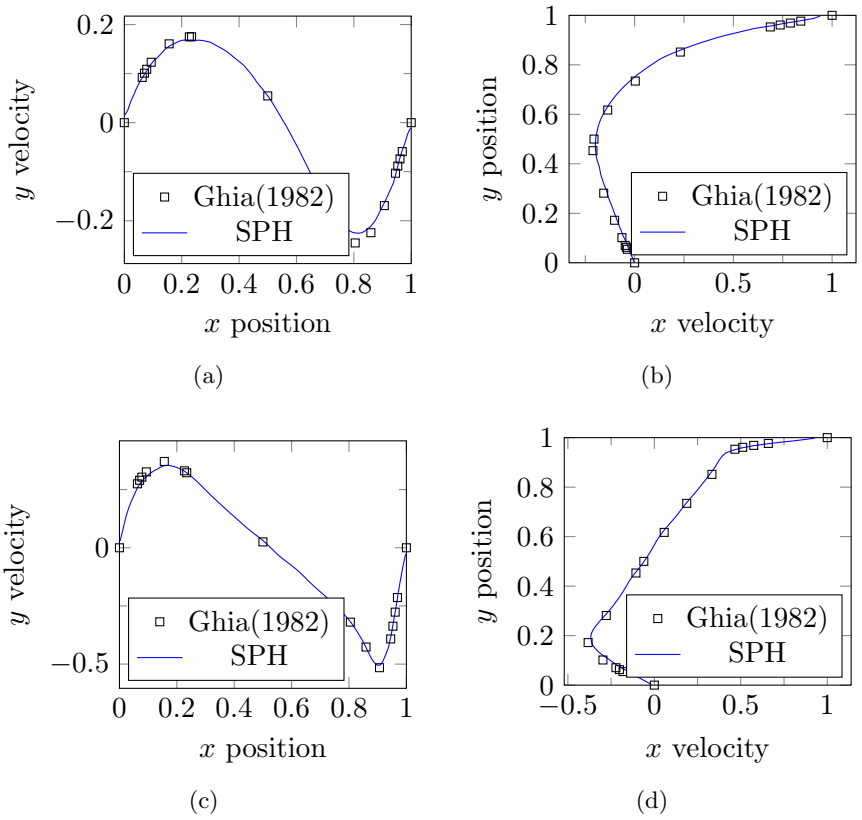

Figure 3.9: Velocity profiles for the lid-driven cavity flow for Re= 100 (top row) and Re= 1000 (bottom row). Y-velocity through the horizontal centre of the cavity (left column) and x-velocity through the vertical centre of the cavity (right column). The SPH results show good agreement with the results of Ghia (1982).

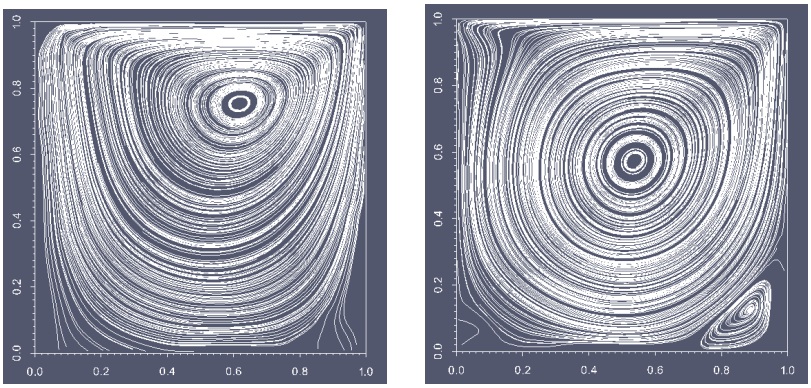

(a) (b)

Figure 3.10: The streamlines for the lid-driven cavity experiment for Re = 100 (left) and Re = 1000 (right). A speed-of-sound of $c = 5$ was used, and the simulation was run for 60 time units. The pseudo-2D simulation was seeded with 100×100 (Re = 100) and 200×200 (Re = 1000) particles. Running the Re = 100 simulation with 200×200 resolution resulted in nearly identical results.

A power-law fluid is characterized by the parameters n and K, where $n < 1$ models a shear thinning fluid, $n = 1$ models a Newtonian fluid, and $n > 1$ models a shear thickening fluid. K is a "flow-consistency index". The shear-stress of a power-law fluid is defined in 1D as

$$\tau = K \left(\frac{\partial u}{\partial y} \right)^n , \tag{3.48}$$

which can be written as a generalized Newtonian fluid,

$$\tau = \mu_{\text{eff}} \left(\frac{\partial u}{\partial y} \right) , \tag{3.49}$$

$$\mu_{\text{eff}} = K \left(\frac{\partial u}{\partial y} \right)^{n-1} . \tag{3.50}$$

In multiple dimensions, the shear rate ($\dot{\gamma}$) is defined by equations 3.41i–3.42. The effective viscosity is

$$\mu_{\text{eff}}(\dot{\gamma}) = K\dot{\gamma}^{n-1}. \tag{3.51}$$

A Hagen-Poiseuille flow for a shear-thinning power-law fluid was set up in a similar manner to the Newtonian simulation of flow through a cylindrical pipe. The velocity profile for a power-law fluid at steady state can be found analytically, and the solution is given by

$$v_z(r) = \frac{n}{n+1}\left(\frac{\partial p}{\partial z}\frac{1}{2K}\right)^{\frac{1}{n}}(R^{\frac{n+1}{n}} - |r|^{\frac{n+1}{n}}), \tag{3.52}$$

where v_z is the velocity in the axial direction, and x is the distance from the centre of the pipe.

A Hagen-Poiseuille flow for a power-law fluid was simulated with three different resolutions, resulting in 11, 21, and 41 particles spanning the diameter of the pipe. The fluid has a density $\rho = 1000$, $K = 1000$, $n = 0.8$, making it moderately shear-thinning. The pipe has a radius $R = 1$. The simulations were run for one second of simulation time.

Approx. Spacing	L_2 Error	Apparent Conv. Rate
0.2	7.67764×10^{-3}	–
0.1	3.40116×10^{-3}	1.17463
0.05	1.71635×10^{-3}	0.98668

Table 3.2: L_2 Error and apparent convergence for a power-law Hagen-Poiseuille flow simulation. Samples were for a slice of particles near the centre of the pipe perpendicular to the flow direction.

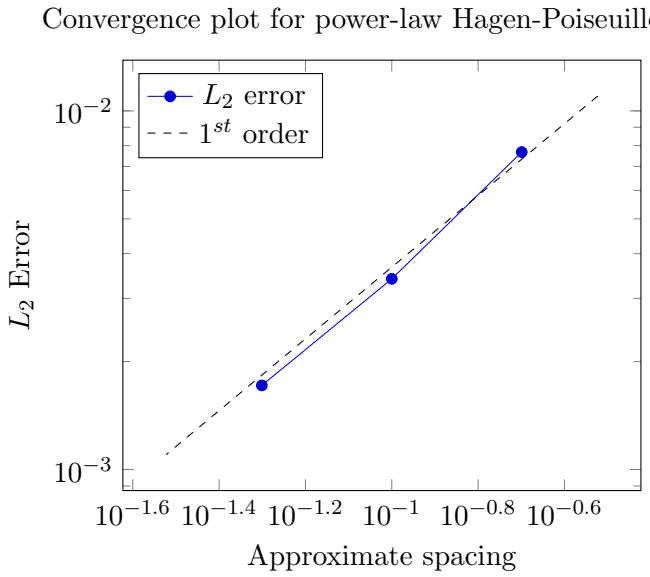

Figure 3.11: The rate of convergence for power-law Hagen-Poiseuille flow also appears to be approximately first-order.

3.4 Conclusion

This chapter summarizes USAW SPH, the SPH method that we chose to use for simulating fluid boluses. We present USAW SPH derivation and its relation to the original derivations. We then show a illustrate a method for handling moving boundaries as well as a method for calculating shear-rates, necessary for simulating non-Newtonian boluses. We demonstrated that the method gives the expected results when simulating some canonical Newtonian and non-Newtonian flows including Couette flow, Hagen-Poiseuille flow, and a lid-driven cavity flow. The Hagen-Poiseuille flow was performed for both Newtonian and power-law fluids. Both demonstrate approximate first-order convergence in the L_2 error norm.

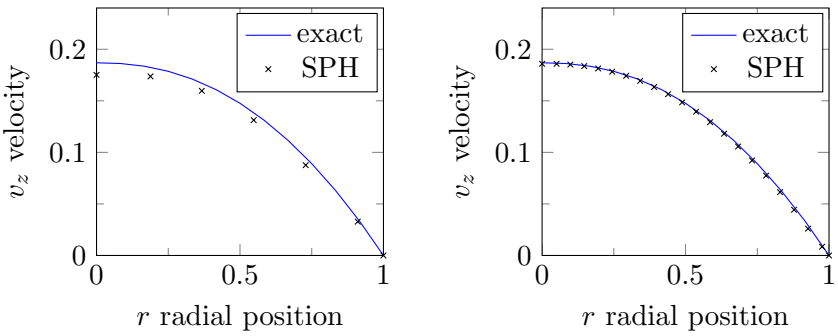

(a) 11 particles span the pipe

(b) 41 particles span the pipe

Figure 3.12: Hagen-Poiseuille flow simulation for a power-law fluid plotted against the exact steady-state solution. The power-law fluid has $K = 1000$ and $n = 0.8$.

Chapter 4

Fluid simulation of oropharyngeal swallowing

A multitude of complexities make it difficult to simulate oropharyngeal swallowing. The flow is truly 3D, and axisymmetric simulations oversimplify the problem. There is a high degree of irregular boundary motion that drives the flow. The material properties of fluid boluses can also be very complex, and there is an interface with air that needs to be handled appropriately. Collecting 3D images of human swallowing is difficult, and until recently there have been no full 3D captures of human swallowing.

After applying the extensions described in Chapter 3, USAW SPH is capable of simulating swallowing in the oropharynx. This chapter describes a practical test of these capabilities, a numerical fluid simulation of swallowing. Section 4.3 describes a novel workflow and purpose-built tool used to segment the airway from 320-row ADCT sequences of swallowing. The numerical simulation tests the assumption that saliva provides lubrication for starch-thickened liquid boluses. The assumption is tested by running both slip and no-slip simulations in dynamic 3D geometries of the aerodigestive tract based on dynamic 3D images. The results suggest that saliva does not

have a significant effect on clinical timing measures of the bolus, however it may decrease oropharyngeal residue at the end of the swallow. The small number of subjects (3) limits the scope of the findings, but the experiments are a successful proof of concept.

4.1 The role of saliva in swallowing

Saliva plays important roles in mastication, swallowing, and maintaining oral and general health. Decreased salivary flow may result in dysphagia [34, 100, 103] and videofluorosopic studies suggest that saliva is required for lubricating the airway and bolus [43, 105]. However, other work finds that the relationship between hyposalivation and dysphagia is unclear [107, 111]. One of the difficulties in understanding this relationship is that the hyposalivation may be confounded by other factors, such as reduced tongue-base retraction. Using a numerical simulation, lubrication as a result of saliva can be simulated in isolation from other pathologies.

This work uses state-of-the-art 320-row Area Detector CT (ADCT) images as the basis for computer fluid simulations of the bolus [57]. 3D simulations of lubricated and non-lubricated aerodigestive tracts in normal subjects were performed, and the results were compared to the bolus position in the images. We assumed that the lubricated simulations would produce better results than their non-lubricated counterparts. Six different swallows were studied; three swallows were completed with starch-thickened boluses, both nectar- and honey-thick. The non-Newtonian viscosities of the nectar- and honey-thick boluses were measured experimentally. The results indicate that

for liquid boluses in normal subjects, the no-slip condition produces more accurate bolus transit times than a slip condition, and that saliva does not lubricate the bolus through the oropharynx. However, the no-slip simulations show significant amounts of residue compared to the slip condition.

4.2 320-row ADCT swallowing sequences

We collaborated with swallowing researchers from Fujita Health University who acquire dynamic 320-row ADCT images of human swallowing in their clinic [36, 57]. Their imaging technique is the first with the ability to capture dynamic, fully 3D images of human swallowing in a single shot (that is, without requiring repetitions of the swallow to form a single image sequence).

The following dataset of six 320-row ADCT swallows were used to create the simulations. Each swallow was of a healthy Japanese subject who swallowed normally. The swallows were from two subjects, as described in Table 4.1. Each image sequence consisted of approximately 2–3 seconds of data sampled at 10 Hz resulting in 20–25 3D "frames". Each frame has $512 \times 512 \times 320$ voxels, with resolution of $0.468 \times 0.468 \times 0.5$ mm^3. This study was approved by the UBC Clinical Research Ethics Board, certificate no. H16-01546.

Subject	Sequence description
34 y.o. female	reclining 45° - nectar thick 4ml
35 y.o. female	reclining 45° - thin 10ml
31 y.o. female	reclining 45° - thin 10ml reclining 45° - honey thick 10ml semi-prone - thin 10ml semi-prone - honey thick 10ml

Table 4.1: Scans from three female subjects provided the data for this simulation study. All subjects were healthy with no history of dysphagia, and not taking any medication.

4.3 Deriving geometric boundaries from 4D ADCT data

For each ADCT sequence, a dynamic *mesh* needs to be created from the images. A mesh is an interconnected set of triangles that approximates a smooth, 3D surface. The vertices of each triangle can be moved in time, causing the mesh surface to move and thus the 3D surface changes shape. Each moving mesh is used as a solid wall boundary condition for the fluid simulation of the bolus.

This section describes a workflow and newly created tools for extracting moving boundaries from 4D images of swallowing. It is published in [54]. Existing methods, both commercial and research, were found to be inadequate for extracting a dynamic boundary of the upper airway from dynamic CT for fluid simulation (see Section 2.4).

Working with dynamic ADCT data has its challenges. There does not appear to be a suitable automated technique for automatically labelling the data. Each sequence has high spatial resolution but only moderate temporal

resolution (10 Hz). During the reconstruction of the images from the scanner data, artifacts can appear as a result of metal fillings, subject motion, or bolus motion. The artifacts may appear as double images (for example, two hyoid bones in the same instance), blurring of edges, dark and bright radial spokes that emanate within an axial slice, and dark spots that appear next to bright moving objects. Additionally, openings such as the upper esophageal sphincter (UES) are normally closed in the CT with no discernible edges (for example, see Figure 4.2(a)), however for USAW SPH simulation, the boundary is required to be topologically constant in time, and therefore these closed sections need to be represented at all time instances. Despite these shortcomings, dynamic ADCT is the only imaging modality that has demonstrated its ability to capture human swallowing in full 3D.

A triangular surface mesh would provide a suitable representation of the aerodigestive tract (the airway). By deriving the motion of the mesh vertices from the ADCT images, a moving 3D boundary would be obtained. However, achieving temporal continuity is a challenge. For example, the UES forms the boundary between the pharynx and the esophagus. It must be segmented correctly in all time instances, even when it is closed. However, in the CT images the UES is squeezed flat, and thus is invisible for most of the sequence (see Figure 4.2(a)). The same issue applies to tongue/palate contact and other anatomic regions that close during the swallow in order to propel the bolus or protect the airway.

We attempted to use existing 3D image-to-image registration algorithms (such as the Diffeomorphic Demons algorithm [119] as implemented in the *Insight Toolkit*) to generate deformation fields that could warp an exist-

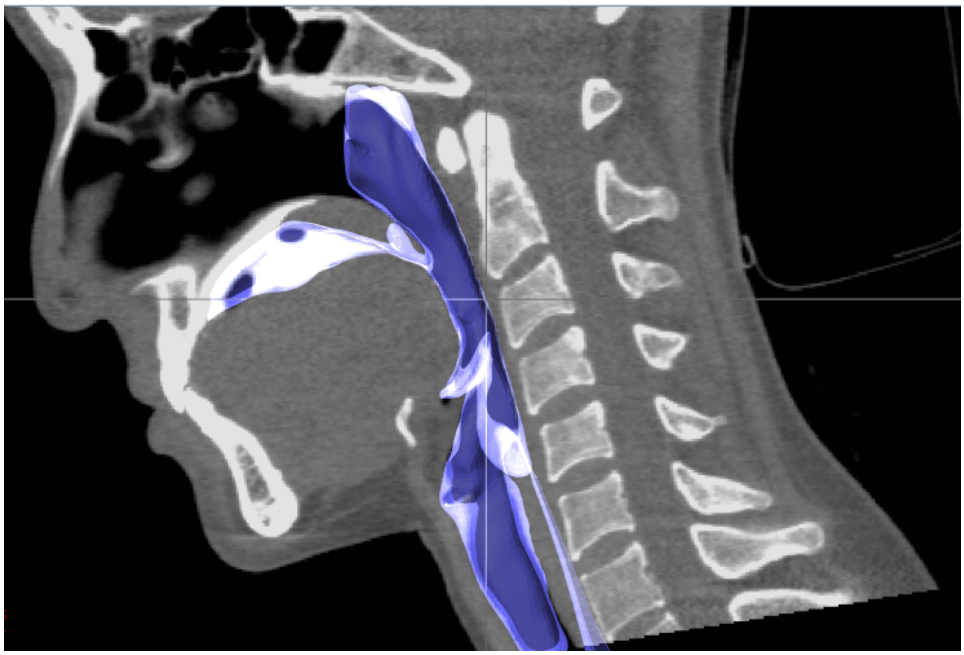

Figure 4.1: The segmented initial mesh (translucent blue) overlaid on the mid-sagittal slice to illustrate the anatomical area being considered.

ing mesh at one time to a subsequent time frame, but this approach was unsuccessful. A similar approach using the *Elastix* toolkit [66] was also unsuccessful. We soon concluded that even if a suitable automated method existed, it would require at least *some* manual intervention.

4.3.1 *BlendSeg*

To address the need for manual deformable registration in 3D, *BlendSeg* was created. It is a tool based on the open-source and extensible 3D modeling software *Blender* (Blender Foundation, Amsterdam, Netherlands). *BlendSeg* facilitates the registration of a triangulated mesh to a 3D volumetric image. *BlendSeg* makes use of *Blender's* "sculpting" feature that allows the operator to morph a mesh using a variety of sculpting brushes while maintaining the same mesh topology (connectivity). Keeping the topology constant allows linear interpolation between vertices in the temporal direction, leading to a continuous deforming mesh. *BlendSeg* consists of two features missing in *Blender*: the first is a method to efficiently display volumetric data as slices in the same space as the mesh, and the second is a method to compute and render the intersection between the mesh and a plane.

4.3.2 Initial mesh generation using *Amira*

The initial triangular mesh can be created using any number of traditional segmentation tools. *Amira* was chosen to create the initial segmentation manually. The surface was tesselated into triangles, simplified, and smoothed using both *Amira* and *MeshLab* software. This initial mesh can now be deformably registered to subsequent time frames (see Figure 4.2).

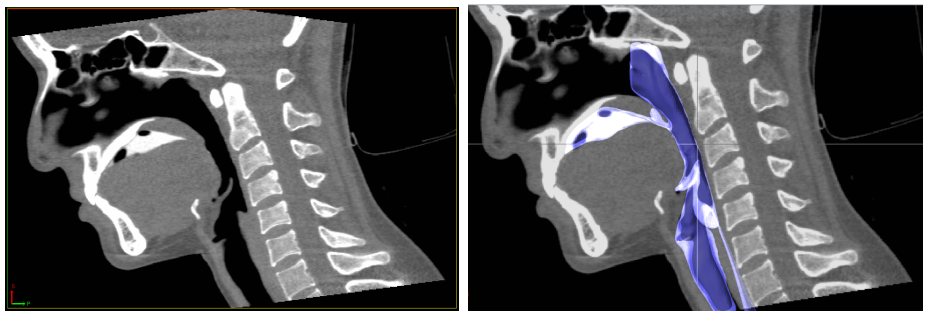

(a) At this initial time, there is no motion and the airway is clearly rendered. However there is closure of the esophagus, and the soft palate seals the oral cavity from the pharynx.

(b) The segmented initial mesh overlaid on the mid-sagittal slice to illustrate the anatomical area being considered.

Figure 4.2: Generating an initial mesh from time t=0. Mid-sagittal slices are shown.

4.3.3 Visualizing 3D volumetric data in *Blender*

Blender's primary function is to create and modify piecewise-planar surface meshes. Currently, there is no method for visualizing 3D imaging data in *Blender*. A powerful application programming interface (API) to *Blender's* underlying engine is provided through the *Python* programming language.

BlendSeg is a *Python* plugin, and it facilitates the visualization of 3D volumetric data in the *Blender* sculpting window. 3D volumetric data (e.g. DICOM data) are converted to three "stacks" of images, each comprised of an axial, coronal, or sagittal stack of images, and imported into *Blender*. Three orthogonal planes are created in *Blender* with each corresponding to one of the anatomical planes. The planes may be moved interactively by the user, however the motion is constrained to translation along the normal direction only. When the planes are translated in space, the displayed texture is updated. In a 4-pane setup (*Blender's* quad-view option), this gives

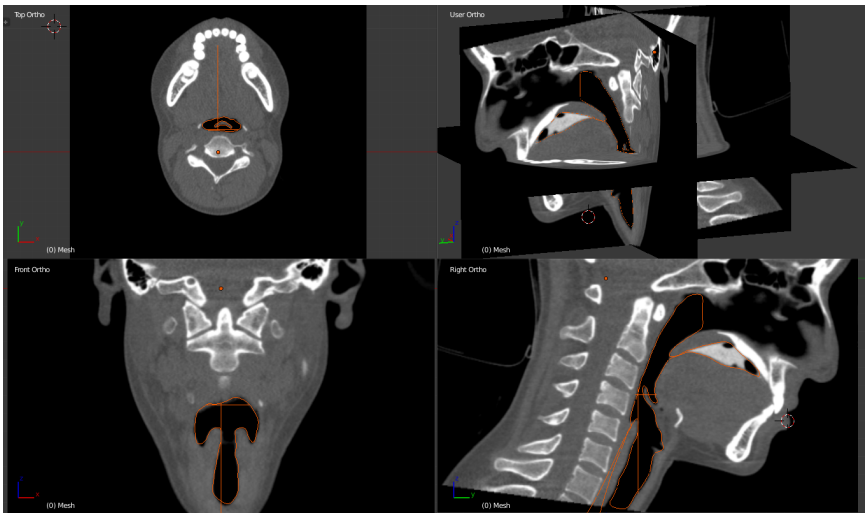

Figure 4.3: Blender's quad-view, when combined with BlendSeg, give the usual anterior-posterior, superior-inferior, and lateral views (bottom left, top left, and bottom right, respectively). The upper right view gives an interactive 3D view which can be used to select which slice is being visualized, as well as to perform sculpting on the mesh. Here, the mesh is being hidden so that the intersections (orange) can be seen more clearly.

the typical anterior, superior, and lateral views (see Figure 4.3). The fourth pane is used for an interactive 3D view, where the planes can be translated by the operator and sculpting of the mesh can be performed.

4.3.4 Generating intersection contours

The second component of BlendSeg is intersection contour rendering. The intersection contour between two surfaces, S and G, is defined as the set of points $x \in (S \cap G)$. BlendSeg computes the intersection contours between the mesh and plane by searching for triangles that cross over the current position of each plane, using an algorithm similar to that described in [4].

Each triangular mesh stores its connectivity using a "quad-edge" data

structure. For the general problem of finding intersections between two discretized surfaces, a tree of axis-aligned bounding boxes (AABBs) can be used to quickly minimize the amount of tests that need to be performed. From this set of potentially intersecting pairs of triangles, a set of Mesh Intersection Points (MIPs) is created.

Any intersection contour between two triangular meshes can be described by an ordered set of MIPs, with straight lines connecting each MIP to the next. Considering two triangles that intersect with one another, the MIPs are the points where an edge of one triangle intersects the face of the other triangle. For a single pair of triangles that potentially intersect, zero or two MIPs exist. Once a set of MIPs are found, at least one contour exists. Beginning at an arbitrary MIP, one can find neighbouring MIPs by utilizing the quad-edge connectivity data to "walk" around the intersection contour, removing MIPs from the set until reaching the beginning MIP. Open contours are possible as well, and are handled by reversing direction upon encountering an open edge (such as the edge of a plane).

For each intersection point and edge representing the contour, new vertices and edges were defined in *Blender* and rendered. Computing intersection contours and rendering them is performed at interactive rates on a laptop computer running *Debian Linux* with an Intel Core i5 processor and 16 GB of memory. Moving the orthogonal, textured planes in *Blender* updates the image as well as the intersection of the mesh with the plane, allowing the user to view how well the mesh lines up with the 3D image data (see Figure 4.3). *BlendSeg* is freely available for download at `https://github.com/andrewkho/blendseg/`.

4.3.5 Interpolating in time to create a moving boundary

Blender's sculpting feature provides a number of "brushes" allowing the operator to push, pull, grab, smooth, and otherwise modify the mesh locally and interactively. The mesh will maintain the same connectivity as long as the option for dynamic topology (DynoTopo) is disabled. This feature allows the operator to sculpt the mesh to match each 3D volume of the swallow sequence. Each vertex position can be interpolated between time points to create a continuous 4D mesh representation of the airway during the swallow sequence.

Different interpolation schemes could be used, but simple linear interpolation provides the best results. Linear interpolation guarantees that the interpolated value will exactly match the specified value at knot points and that there won't be any overshoot. We found this to be important when dealing with opening and closing of the glossopalatal junction.

Special mention should be made regarding tangential mesh motion, i.e. vertex motion constrained to the surface of the mesh. For a fluid simulation using no-slip boundary conditions, shearing forces would be exerted on the fluid in the direction of the vertex motion. In reality, surfaces such as the hard-palate exhibit no tangential motion, but other surfaces like the tongue may exhibit substantial tangential motion that is not captured in the CT images. The CT data is unable to directly capture this type of tangential boundary motion, however it may occur in the 4D mesh as an artifact of the sculpting process. To eliminate this effect on the fluid simulation, when computing the vertex velocities on the boundary, the tangential component

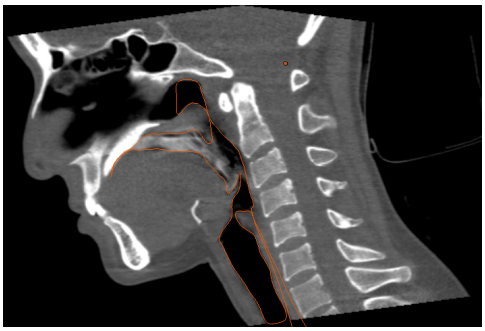

Figure 4.4: Example mid-sagittal slice from time t=0.5s showing the intersection of the mesh with the slice.

of the velocity is ignored.

4.3.6 Extracting the boundaries

The process of using BlendSeg to register a mesh to a single 3D image can take anywhere from a few minutes to a few hours depending on the amount of sculpting required. After creating meshes for four swallow sequences, each consisting of between 22 and 25 individual 3D images, the total time for creating a moving airway is estimated to be around 30 hours. This does not include the time it takes to create an initial mesh. The first time a mesh of an anatomic structure is created (for example the tongue, or airway), a mesh needs to be created using traditional tools (such as *Amira*) which can take a significant amount of time depending on the tools used. If a mesh with approximately similar geometry already exists, it can be registered to a new initial frame quickly using BlendSeg. Since temporal continuity is not required from the prior mesh to the new initial mesh, new vertices may be inserted and topology changes are permitted.

To evaluate each registered mesh, two experts familiar with the anatomy

and physiology of swallowing were enlisted. One is a practising clinician and the other is an anatomist who specializes in swallowing function. The experts verified the registrations by visual inspection of the intersections in BlendSeg. The method of handling airway closures (such as the UES, vocal folds, palatal-glottal contact, and nasopharynx) was explained to the experts. To evaluate each registration, a first pass was made looking at the sagittal slices that covered the airway. The lateral videofluoroscopic image is the most common method of evaluating dysphagia, and so the sagittal slices were chosen for the first pass (see Figure 4.4). Following the first pass, closer examination was performed for areas of the image that included motion artifacts such as blurring or ghosting. In these difficult-to-interpret sections, context from nearby sagittal, axial, coronal, and temporal images were required.

4.4 Viscosity of thickened boluses

Viscosity is a material property that represents the amount of resistance to shearing of a fluid, here represented with the symbol μ. Imagine the tongue holding a liquid bolus against the hard-palate. A shearing motion is one where the tongue moves parallel to the hard palate. For a "thicker" fluid such as honey, there is significant resistance to that shearing motion, and thus the viscosity is higher. For a "thin" fluid such as water, there is little resistance, and thus the viscosity is low.

A Newtonian material, such as water, has a value of μ which is constant. In our simulations we assigned water a viscosity of 1 cP (centi-

Poise). Boluses thickened with starch exhibit non-Newtonian shear-thinning behaviour, and the value of μ depends on the *shear-rate*. To go back to the tongue analogy, a shear-thinning bolus would show high resistance to shearing when the tongue is moving slowly, but as the tongue speeds up, the resistance would lower. The Cross model of viscosity computes an effective viscosity based on the shear rate according to the following equation:

$$\mu_{\text{eff}}(\dot{\gamma}) = \frac{\mu_0}{1 + (\frac{\mu_0}{\tau_*}\dot{\gamma})^{n+1}}, \tag{4.1}$$

where μ_0, τ_*, and n characterize the behaviour of the fluid. μ_0 has units of viscosity [Pa·s], τ_* has units of stress [Pa], and n is dimensionless.

The viscosities of the nectar- and honey-thick boluses were measured in order to simulate them. A 100 ml sample of nectar-thick bolus consists of 95 ml water, 5ml barium suspension, and 2.5 grams of thickener. The honey-thick bolus is the same as the nectar except 5 grams of thickener is used. The thickening agent is *Top Balance III* (Neo-hai-torome-ru; Foodcare Inc., Sagamigahara, Japan) which comes in 2.5 gram packets. Before being administered to the subject for imaging, the bolus is chilled in a refrigerator for 4-5 hours.

A calibrated *KINEXUS* rheometer (Malvern Instruments, Malvern UK) was used to measure the viscosity of the boluses. Samples of the nectar- and honey-thickened boluses were prepared using distilled water. A cup-and-bob geometry was used to measure the boluses. The boluses were measured at a temperature of 10°C. Each bolus type underwent the following protocol: a five minute pre-shear was run in order to stabilize the sample and the tem-

perature. A test was performed by varying shear rate between 0.01 s^{-1} and 1000 s^{-1}. After the first ramp-up test was performed, a second test was performed on the same sample after a five minute delay. A new sample was then loaded into the machine, underwent a five minute pre-shear/temperature stabilization, and a third ramp-up test was performed. To check whether the refrigeration period of the sample makes any difference, a final pre-shear and ramp-up test was performed on a sample which had been refrigerated for 3 hours in order to make sure that refrigeration has no effect on the measurements.

4.4.1 Slip and no-slip boundary conditions

The typical boundary condition used in fluid flow problems is no-slip. Fluids "stick" to solid boundaries and their velocity is equal to that of the boundary. For fluid flowing through a stationary rigid pipe, the velocity of the fluid at the wall is zero. We use the no-slip boundary condition to approximate a dry-mouth swallow, since there is no saliva lubricating the bolus.

For healthy subjects, such as those in the images that are being used in this study, a layer of saliva coats the solid boundaries. The saliva lowers the friction between solid-solid contact (such as between the tongue and palate). As a boundary condition for fluid flow in a saliva coated airway, we use a full-slip boundary condition on the fluid. The full-slip condition constrains the fluid velocity to prevent penetration into the solid, but does not restrict its velocity in a direction tangent to the solid surface.

As shown in Appendix B, the full-slip condition can be a reasonable approximation for lubricated bolus flow, however the quality of the assumption

depends on the viscosity and width (quantity) of saliva coating the airway, as well as the duration of the swallow. In reality, saliva viscosity and width can vary based on many factors. It can change between individuals, within the same individual based on time of day, whether the salivary flow is stimulated or not, and even depending on the location in the airway where the measurement is made. We expect that the results of a full-slip and no-slip simulation will bracket the actual behaviour of the bolus flow, however for the time-scales involved in swallowing, and for some choices of saliva viscosity and quantity, the full-slip condition is a reasonable approximation to a saliva-lubricated flow.

4.4.2 Bolus measurements

Bolus based measurements were made on both the CT data and the simulation data. The measurements chosen are entirely determined by bolus position, and as such are suitable for measuring the simulation data. The oral transit time (OTT), pharyngeal transit time (PTT), and residue were measured. Three time points were marked for each swallowing sequence: the time of the first backwards motion of the bolus head, the time when the bolus head cross the ramus of the mandible, and the time when the tail of the bolus clears the cricopharyngeal region. The OTT is defined as the difference between the first two times, and the PTT is defined as the difference between the second and third times.

All images were presented from a lateral, orthographic view. The CT data was transformed into a "virtual videofluoroscope" that compressed each 3D time frame into a 2D view that mimics a traditional VFL image. The

simulations were presented from a lateral, orthographic view (see Figure 4.9, left and right columns). CT frames were 0.1 seconds apart, and the simulation time frames were 0.02 seconds apart. The measurements were made by a Speech Language Pathologist (SLP). A second SLP also evaluated the data to confirm the results of the first. The second SLP was blinded to the results prior to the evaluation. In cases where their measures differed by 0.05 seconds or more, the SLPs came to a joint consensus about what time should be chosen. The time interval 0.05 s corresponds to three or more frames in simulation, and one or more frames of ADCT data.

4.5 Results

The viscosity measurements for the starch-thickened boluses are presented in a plot measuring the apparent viscosity as a function of strain-rate, in Figure 4.5. For each bolus type (nectar and honey), four tests were run on 3 different samples, and there were almost no differences observed between them, demonstrating high repeatability.

The viscosity curves were modelled using the Cross viscosity model, as described in equation 4.1. A power-law model was first fit to the experimental data, and then the Cross model parameters were chosen to match the power-law model. The parameters are given in the Table 4.2. The models of the viscosity curves are also plotted in Figure 4.5.

All of the boluses were simulated with initial density of $\rho_0 = 1000\ \frac{kg}{m^3}$, and an initial spacing of 1 mm between particles, with 1000 particles for each millilitre of fluid. The artificial speed-of-sound was $c = 10\ \frac{m}{s}$ for all

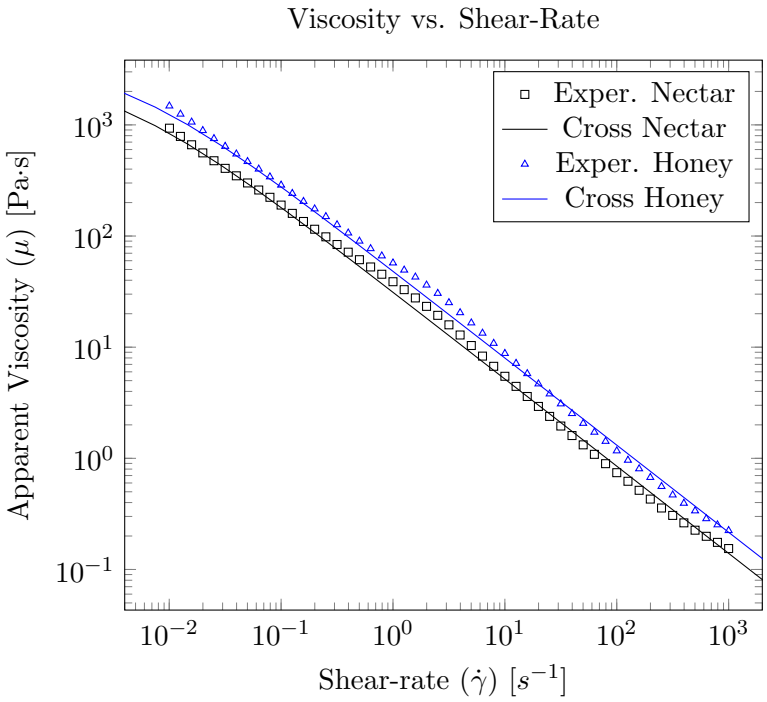

Figure 4.5: Plot of apparent viscosity vs. shear-rate for nectar- and honey-thick boluses at a temperature of 10°C. Note that these are log-log axes. The materials have very similar curves, and are both highly shear thinning.

	Nectar-thick	Honey-thick
n	0.2156	0.2156
μ_0 [Pa·s]	3000	4000
τ_* [Pa]	9	14.5

Table 4.2: Parameters of the Cross model for the Nectar- and Honey-thick simulations.

simulations.

The simulations were able to run mostly unsupervised and each took between 1−21 days to complete using machines with multi-core Intel i7 CPUs. The reason for the long computation times were that starch-thickened boluses required smaller simulation time-steps to avoid numerical instability because of the viscous diffusion limit on the maximum step size, while the thinner boluses had time steps limited by the CFL condition.

4.5.1 Thickened boluses

For the starch-thickened bolus simulations, we expected to see a large difference between the slip condition and no-slip condition simulations. For all three of the thickened bolus sequences, we found that the no-slip condition produced a more accurate approximation of the bolus flow compared with the slip condition. The position related timings of the bolus are in Table 4.3. As a test for resolution independence, the nectar-thick simulation was performed with an initial spacing of 0.8 mm, resulting in 7812 particles instead of 4000. The results for both the slip and no-slip simulations showed no significant differences.

OTT and PTT are useful measures when comparing both inter- and intra-patient swallows, however since we are looking at a single swallow and comparing simulation to CT scans, we are actually performing intra-*swallow* comparisons. In this case the absolute time measures become relevant. In Figures 4.6–4.8, the times chosen for "first backwards motion of the bolus", "bolus head crosses the intersection of the ramus of the mandible and base of tongue", and "bolus tail leaves cricopharyngeal area" are indicated

		CT	Slip	No-slip
Nectar (reclined)	OTT [s]	0.3	0.3	0.26
	PTT[s]	0.5	0.5	0.52
	Residue [%]	0	0.4	43.0
Honey (semi-prone)	OTT [s]	1.1	0.98	1.12
	PTT[s]	0.5	0.72	0.58
	Residue [%]	0	18.53	29.02
Honey (reclined)	OTT [s]	0.9	0.32	0.8
	PTT[s]	0.7	0.98	0.7
	Residue [%]	0	15.71	31.07

Table 4.3: Summary of transit times and residue for CT, and simulated slip/no-slip for each swallow sequence.

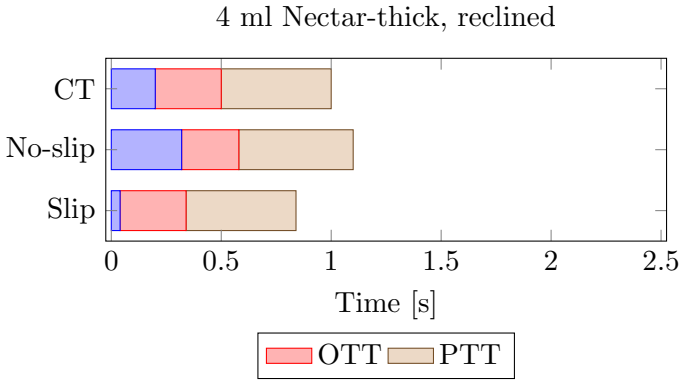

Figure 4.6: Timing chart for 4ml nectar-thick bolus, reclined position.

discretely. The red and green bars indicate the OTT and PTT, resp.

Nectar-Thick - Reclined Position

For the 4 ml nectar-thick (reclined) sequence, the simulated slip condition bolus leaves the oral cavity before the no-slip bolus. Comparing the oral transit times of the CT, slip, and no-slip conditions (Table 4.3), both of the simulated OTTs were 0.04 s away from the CT measurement, however they lie on opposite sides of the CT measurement, with the no-slip simulation

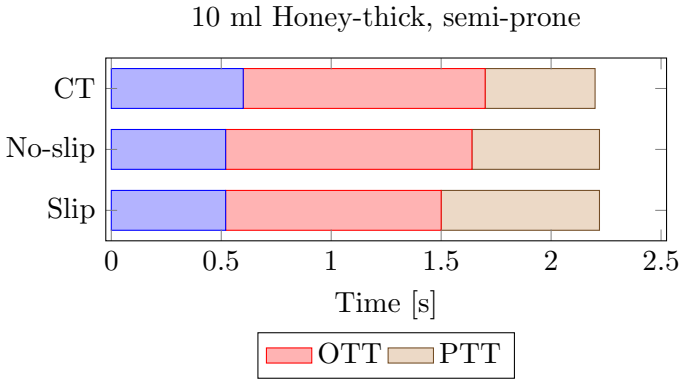

Figure 4.7: Timing chart for 10ml honey-thick bolus, semi-prone position

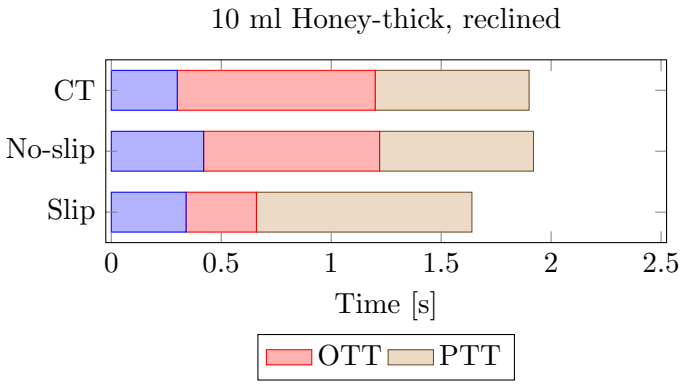

Figure 4.8: Timing chart for 10ml honey-thick bolus, reclined position

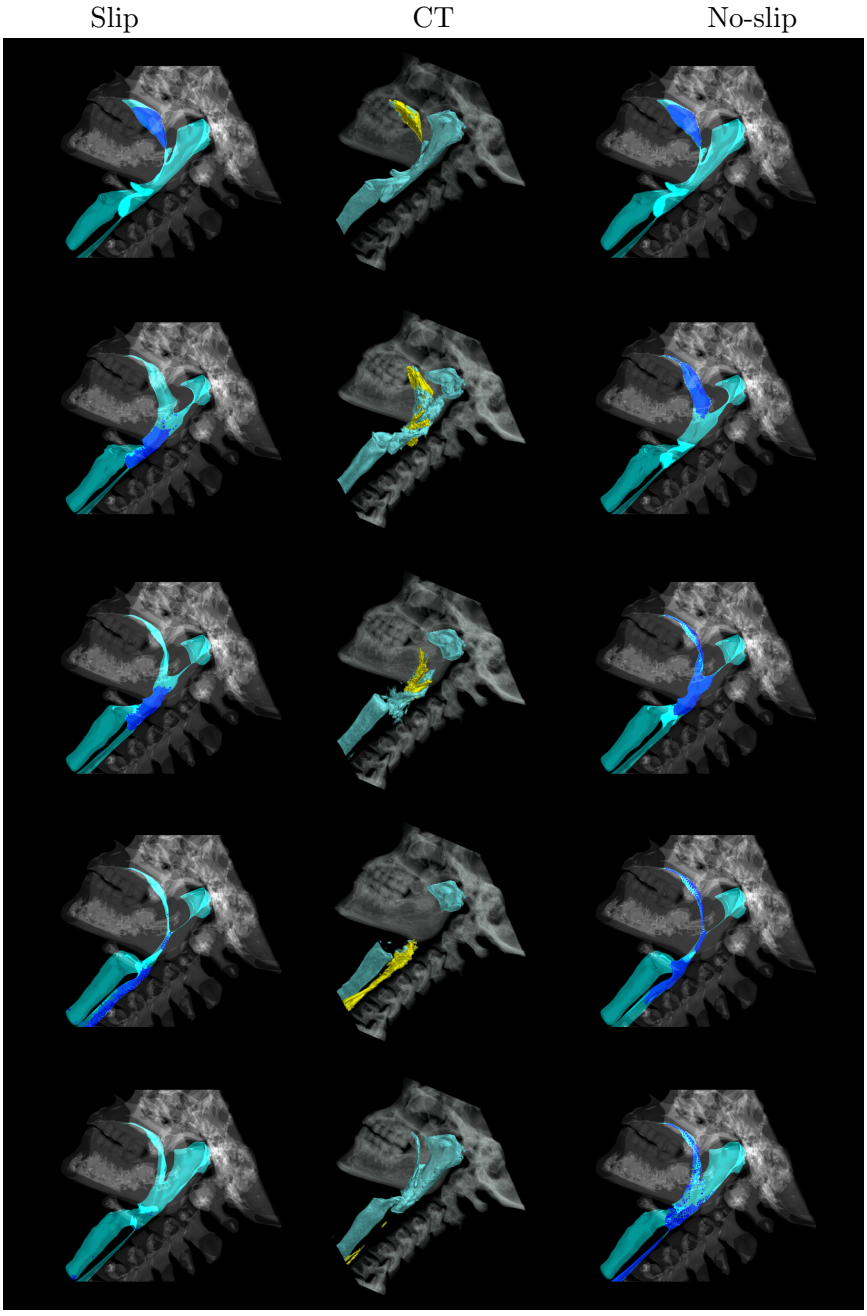

Figure 4.9: Nectar-thick bolus, semi-prone position. Columns (L-R): slip, 3D CT, no-slip.

having a shorter OTT. The reason for this is that the first backwards movement of the slip simulation was much earlier due to poor oral containment. For PTT the slip and no-slip give very similar measurements. In this case, looking at the timing chart in Figure 4.6 illustrates how the OTT is better approximated by the no-slip condition. The bolus leakage from the oral cavity in the slip condition means that the PTT begins earlier. Therefore, the bolus tail leaving the cricopharyngeal region is also earlier for the slip condition.

These differences can be observed in Figure 4.9. In the CT images, it appears that the squeezing motion of the tongue, palate, and pharynx is the dominant driver of bolus motion as evidenced by the lack of air near the bolus tail (see Figure 4.9, row 2). However, for the slip condition an air bubble is visible trailing the bolus tail.

When quantifying the residue remaining in the oral cavity and pharynx after the swallow, the no-slip simulation has a large quantity of residue in the oral cavity and pharynx, however the slip has almost none. The CT images show only trace amounts of residue after the swallow.

Honey-thick - Semi-Prone Position

This sequence consists of a normal subject lying semi-prone in the CT scanner swallowing a 10 ml honey-thick starch-thickened bolus. The measured OTT and PTT of the no-slip bolus condition shows better agreement with the CT data compared with the slip bolus condition (see Table 4.3).

Visually, the slip and no-slip simulations both show similar results to the CT images (see Figure 4.10). Neither the slip nor no-slip conditions have an

air bubble trailing the bolus tail. The most obvious visual difference is found when looking at the interface between the bolus head and the air when it starts to leave the oral cavity (see Figure 4.10, second row). An alternate view can be found in Figure 4.11 where slices of the simulations are shown instead of lateral projections.

When considering residue, both of the simulations have significant residue in the oral cavity, valleculae, and piriforms after the swallow, with more residue observed in the no-slip condition simulation compared with the slip condition simulation (see Table 4.3).

Honey-thick reclined

In this sequence the subject sat in a reclined position and swallowed a 10 ml honey-thick starch-thickened bolus. The most striking visual difference between the slip and no-slip simulations is the significant pre-swallow leakage of the bolus from the oral cavity during the slip condition simulation (see Figure 4.12, second and third rows). Similar to the nectar thick swallows, for both the CT and no-slip images, the bolus tail is cleared from the oral cavity by the squeezing motion of the tongue against the palate, while the slip condition exhibits a bolus tail that is trailed by an air bubble.

Looking at Table 4.3, as well as Figure 4.8, the no-slip condition simulation shows better agreement with the CT images while the slip condition measure for OTT is much shorter due to the leakage of the bolus and the speed with which the leakage travels to the intersection of the ramus of the mandible and the tongue base.

Both the slip and no-slip simulations show significant residue in the

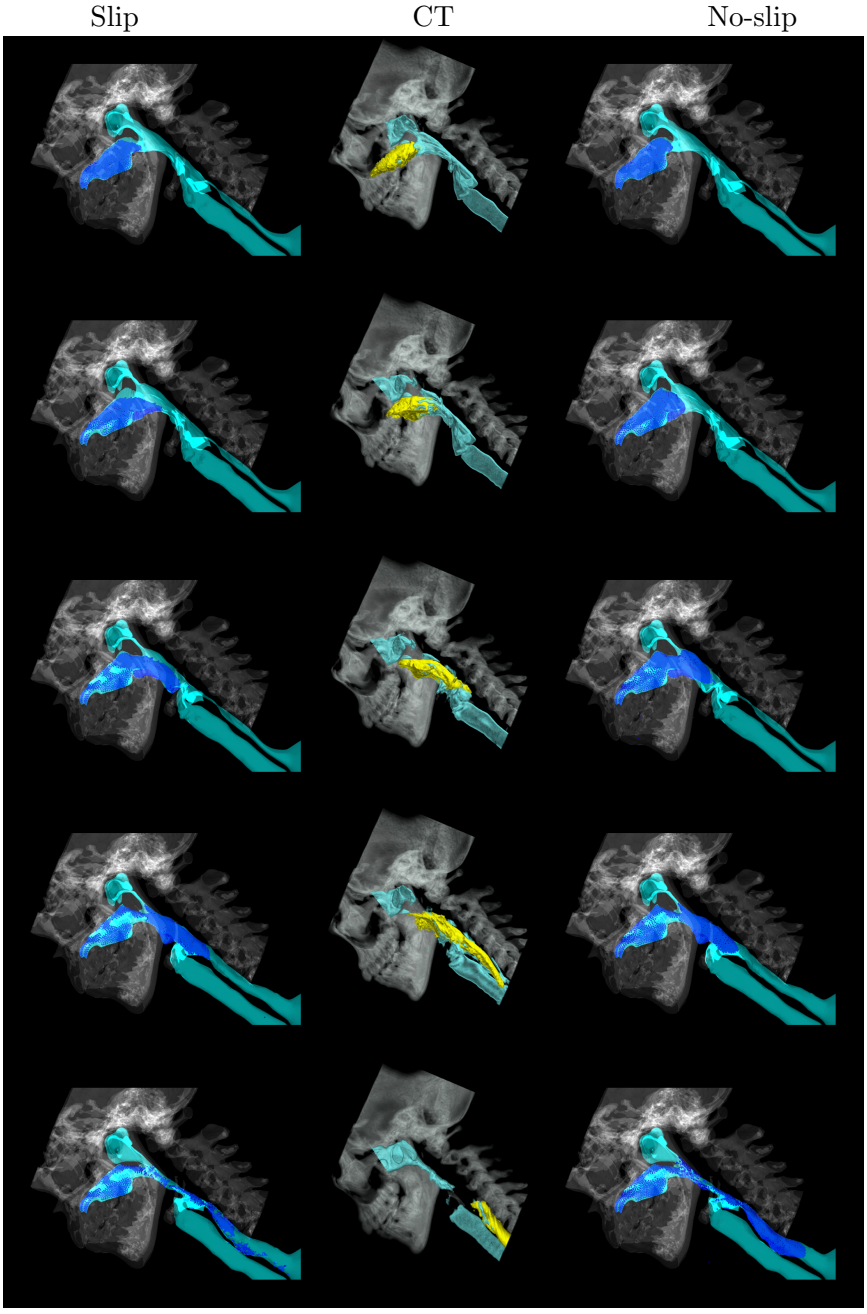

Figure 4.10: Honey-thick bolus, semi-prone position. Columns (L-R): slip, 3D CT, no-slip. The shape of the air-bolus interface at the bolus head shows better agreement to the CT images in the no-slip condition than the slip condition in the oral cavity and pharynx.

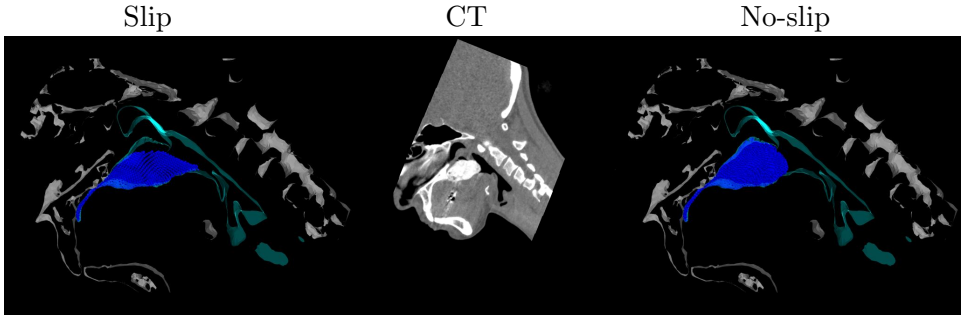

Figure 4.11: Detail of bolus-air interface at a single mid-sagittal slice, at the initiation of swallowing. The interface of the no-slip bolus shows better agreement with the original images than the slip bolus.

oral cavity and pharynx after the swallow, with more residue observed in the no-slip simulation. The quantities of residue are similar to the honey-thick semi-prone swallow simulations. For the no-slip simulation, numerical instability occured before the end of the swallow, however, we have estimated the quantity and location of residue based on the last stable time.

4.5.2 Thin boluses

The thin boluses were simulated as Newtonian materials with a viscosity of 1 cP. All three sequences used boluses of 10 ml. Because the viscosity was so low, we expected the slip and no-slip simulations to be very similar. In the first reclined simulation, the no-slip simulation showed had a small amount of residue (9 particles) and a single particle was aspirated. In the other two simulations, both the slip and no-slip simulations showed small amounts of aspiration (less than 3% of total volume) while the CT images showed none. The semi-prone swallow exhibited approximately 5% oropharyngeal residue, while none was detectable in the CT images.

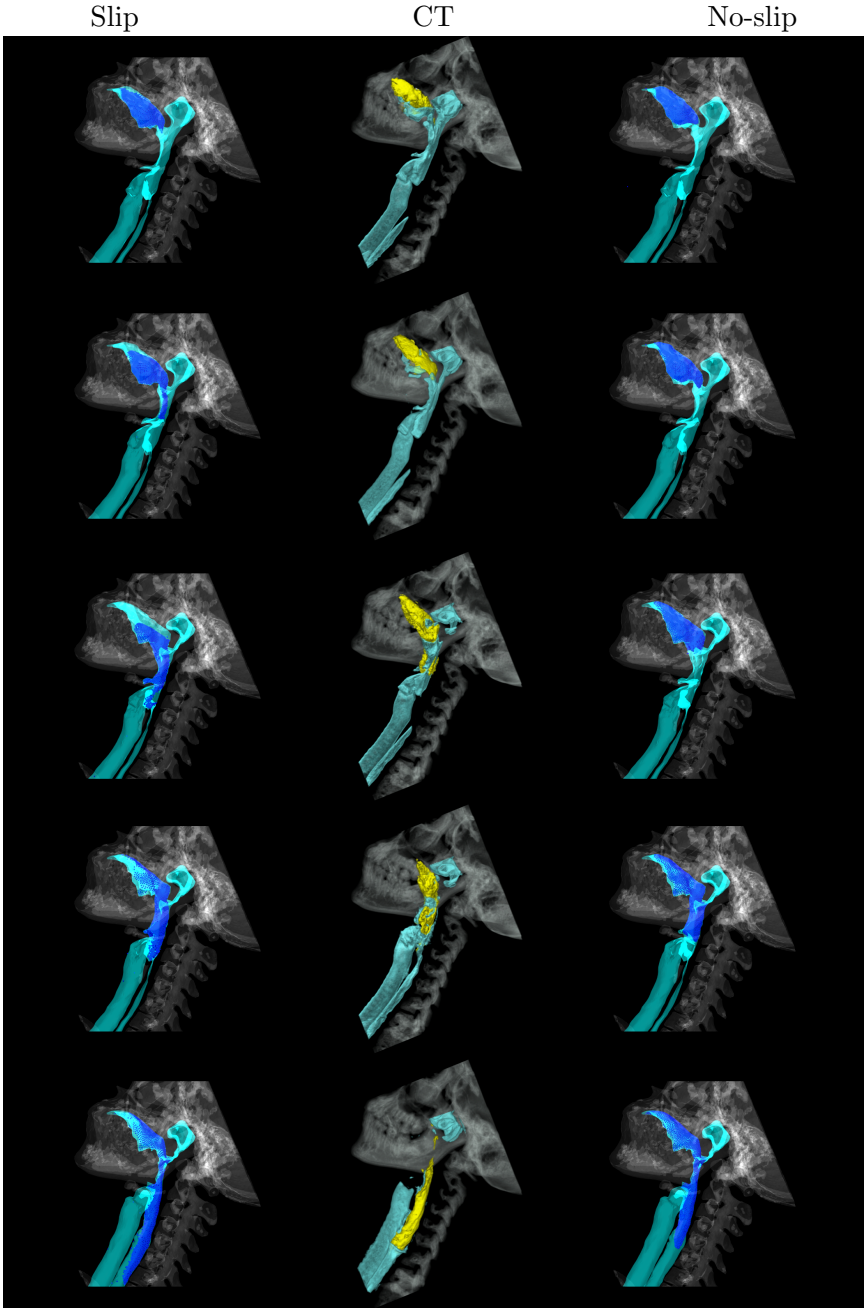

Figure 4.12: Honey-thick bolus, reclined position. Columns (L-R): slip, 3D CT, no-slip. The slip bolus escapes the oral cavity very easily as shown in the second and third rows. The no-slip bolus remains in the oral cavity, showing better agreement with the CT images.

		CT	Slip	No-slip
Thin (reclined)	OTT [s]	0.2	0.18	0.14
	PTT[s]	0.3	0.54	0.56
	Residue [%]	0	0	0.09
	Aspiration [%]	0	0	0.01
Thin (reclined)	OTT [s]	0.3	0.24	0.22
	PTT[s]	0.1	0.3	0.38
	Residue [%]	0	0.69	1.36
	Aspiration [%]	0	2.92	2.47
Thin (semi-prone)	OTT [s]	0.2	0.14	0.14
	PTT[s]	0.5	0.4	0.44
	Residue [%]	0	4.42	5.65
	Aspiration [%]	0	1.75	2.55

Table 4.4: Summary of transit times and residue for thin boluses. CT, simulated slip, and no-slip for each swallow sequence. Some simulated boluses were "aspirated", and percentage volume is indicated as well.

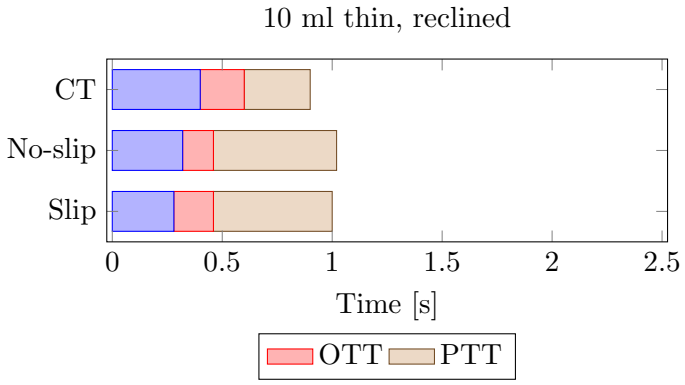

Figure 4.13: Timing chart for 10ml thin bolus, reclined position.

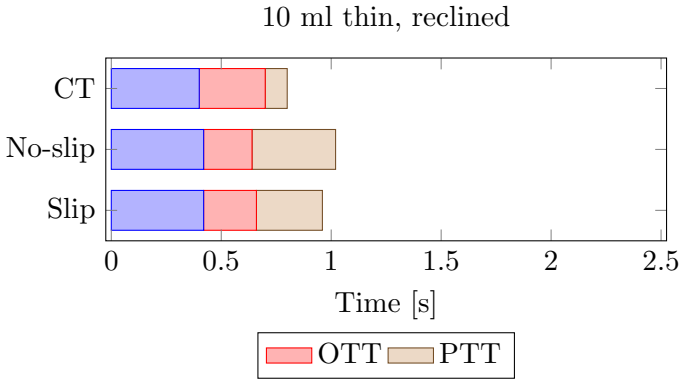

Figure 4.14: Timing chart for 10ml thin bolus, semi-prone position

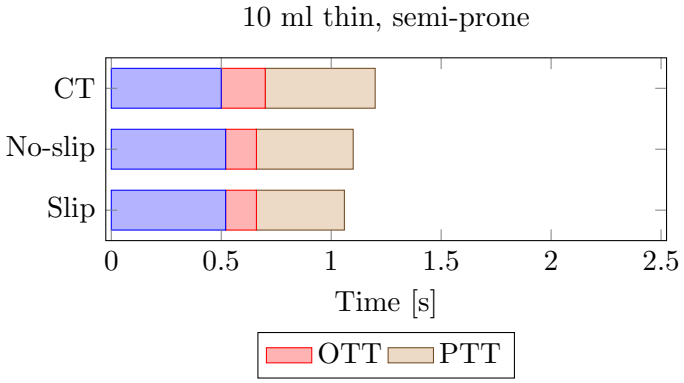

Figure 4.15: Timing chart for 10ml thin bolus, reclined position

4.6 Discussion

The experiments in this work test the assumption that in healthy individuals, saliva lubricates starch-thickened boluses during swallowing. We performed a series of simulations of healthy swallows based on dynamic CT data and, for thickened boluses, found that the no-slip condition generally gives better predictions of bolus transport and transit times than a slip condition. However, the no-slip condition also predicts a much higher quantity of residue than the slip condition, and that are visible in the ADCT images.

The results of the simulations seem to imply that in normal subjects, the presence of saliva does not have the effect of lubricating the bolus to shorten its transport times through the airway. Saliva has a much lower viscosity than the thickened boluses in the sequences we studied. With a moderately thick (or wide) layer of saliva coating the airway, we would expect to see measurable shortening of bolus transport times and a quicker transport through the oral cavity and pharynx (see Appendix B). However, the no-slip simulations exhibit a higher quantity of oropharyngeal residue after the swallow. This could be interpreted as evidence that saliva helps to decrease the residue after a swallow.

4.6.1 Thickened boluses

One of the biggest differences between the two boundary conditions were that with the slip condition, the bolus appears to be influenced much more by gravity. This is evidenced by the air near the tail of the slip bolus, which is absent in the no-slip and the CT images. A number of physical phenomena

might explain the observations. One explanation is that the saliva is present in a thin enough layer that it does not significantly affect the bolus. For this to be realistic, consider a gravity driven bolus (such as the reclined position with leakage out of the oral cavity, Figure 4.12). For a saliva layer at least 100 microns thick, we would expect the full-slip approximation to give a good approximation to the CT images (see Appendix B).

Instead, the no-slip condition appears to give a much better approximation. One possible explanation is that the saliva layer has a thickness on the order of only a few microns or less. If we consider a flow-rate based analysis, as in Appendix A, thin portions of the bolus would be influenced more by a thin layer of saliva than thicker portions. However, a microns thick saliva layer is extremely thin and it is not obvious if this is the case in reality.

Another explanation is that the saliva is quickly absorbed into the bolus so that it no longer provides lubrication, or similarly, that the saliva is quickly removed from the airway surface by the passing bolus so that its lubricating effect would not significantly speed up the transport of the bolus. It could also be a combination of the two, however the important takeaway is that it does not appear that saliva lubricates **liquid** boluses in this manner. Solids do not follow the same rules as fluids with respect to friction, therefore saliva might still play a very important role in lubricating solid and semi-solid foods during the swallow and lowering the coefficient of friction.

Residue

The thickened bolus simulations all demonstrated higher quantities of residue with a no-slip condition than a slip condition. This might suggest that saliva

may play a role in decreasing residue, however there are other possible explanations for this behaviour. One is that the residue in the simulation is a function of the moderate number of particles. The no-slip condition makes the assumption that an infinitesimally small layer of bolus always coats the surface of the aerodigestive tract. For the particle resolution used in this work (1 mm diameter), the small layer has a finite and significant volume that contributes to the residue at the end of the swallow. Increasing the resolution of the simulation may decrease the amount of residue because the no-slip layer would then consist of smaller particles. However it is not clear if the volume of residue would approach zero as the particle size tended to zero, or if it would converge to some small but finite volume.

The residue in the simulations might also be due to the difficulty in fully closing the virtual pharynx (a small gap must be left in order for the simulation to remain stable), or obtaining the correct timing of the pharynx closure. It is also possible that saliva has a larger effect when lubricating thin streaks of boluses, such as the bolus tail, and so they are more effectively cleared by the squeezing motion. Another possibility is that the temperature of the bolus tail is higher than 10°C, and thus has a lower viscosity than the assigned viscosity.

4.6.2 Thin boluses

Because the thin boluses were simulated with a very low viscosity (similar to water), we did not expect the slip and no-slip to have very different results, and that is what we observed. The measured timings were all very similar, within 0.05 s or less, except in one case where the PTT was increased by

0.08 s in the no-slip simulation. In addition, the differences in simulated residue and aspiration between slip and no-slip were within 1% of the total bolus volume.

We suspect that the simulations show aspiration because thin boluses move faster than thickened boluses, and as such, the 10 Hz may be insufficient to adequately capture the speed of the epiglottic inversion and vocal fold closure. 'Because the simulations showed aspiration while the original CT images did not show any, and because the slip and no-slip simulations were very similar, they did not give evidence towards saliva's role in swallowing with respect to lubrication.

4.6.3 Corroboration with existing simulation and clinical research

In Sonomura et al. [112] the authors use a slip condition to model the presence of saliva. However, they also found that they needed to decrease the strength of gravity to one third of its actual value in order to obtain realistic bolus velocities. Our findings suggest an explanation for their results, that the slip condition would have unrealistically sped up the bolus in their simulation. In the clinical research literature, Sonies et al. [111] found that despite the fact that healthy individuals demonstrate a wide range in salivary flow rates (salivary volumes), they are very similar with regard to the characteristics of their oropharyngeal swallowing of saliva and thin fluid boluses. Rogus-Pulia & Logemann [107] examined swallowing in patients with Sjögren's Syndrome compared with healthy controls. They found that although patients with Sjögren's syndrome perceive their swallows to be

impaired, few statistically significant differences were found between the patients with Sjögren's syndrome and the normal age-matched controls on temporal measures of swallowing of thin, pudding thick, and solid food boluses. These findings appear to be consistent with our simulation results. Hamlet et al. [43] performed a retrospective study of head and neck cancer patients with postradiation xerostomia and normal controls swallowing for barium liquid, paste, and shortbread cookies. They found that bolus transit times were unaffected compared to healthy controls, but oral and pharyngeal residue was increased in the patient group, also consistent with our results.

However, other studies have reported that hyposalivation is associated with significant lengthening of bolus transit times [12, 105], but this may be due in part, to variation in study designs, assessment methods, and selection of outcome measures. For instance, in [12], the authors perform an age-matched comparison between subjects with Sjögren's Syndrome and healthy controls, and found that the Sjögren's subjects exhibited longer times for a water bolus than the healthy controls. However, they used ultrasound to measure hyoid bone motion and did not observe the bolus flow directly with VFL. In [105], the authors also compare patients suffering from Sjögren's syndrome with healthy controls, and use VFL to measure timings for basal swallows (no bolus) and 10 ml water bolus swallows. However, their study did not use barium as a contrast agent and therefore do not observe the bolus directly. Their timing measures are based on the motion of observable anatomical landmarks, such as the hyoid bone.

4.6.4 Limitations and assumptions

Every computer model relies on making simplifying assumptions to keep simulation times tractable. The main assumptions in this simulation are the following: temperature is constant (isothermal), chemical effects are ignored (e.g. amylase in saliva is known to significantly decrease the viscosity of starch-thickened boluses), the effect of air is ignored, the fluid is allowed to be slightly more compressible than in reality, and the simulation method only allowed for a moderate number of particles. The simulations also assume that the saliva presence is uniform throughout the oropharynx, however in reality the thickness of saliva varies and depends on multiple factors.

Of these assumptions, the chemical effects are the most likely to influence the simulation. Air has a low density relative to liquids so that its effect is likely negligible. Temperature changes could affect the simulation in one of two ways: by energy exchange and therefore having an effect on the momentum of the fluid, or by changing the material properties of the bolus. Although there is a significant temperature difference between the human body and the bolus, the short duration of the event makes it unlikely that the temperature of the bolus changes significantly during the swallow. Artificial compressibility is controlled by a speed of sound parameter, and it has been reported that choosing a speed of sound 10 times greater than the maximum expected velocity results in a less than 1% change in volume. Our chosen speed of sound (10 m/s) is much higher than ten times the maximum bolus viscosity, and therefore should not have a significant effect on the simulation outcome. Chemical effects, that is, the mixture of amylase with saliva,

have been shown to have a significant effect on viscosity over short periods of time [44]. However, their study found that without vigorous mixing, the effect of the amylase was restricted to a small local area, and for our simulation we assume that the bolus was not vigorously mixed with saliva before swallowing.

The most significant source of error in the simulation is in the boundary extraction from the CT images. Since the work was done manually, human errors are inevitable but hopefully small. Spatial resolution of the CT images is very high and more than adequate for thin structures such as the epiglottis, however the temporal resolution, 10 Hz may not be enough to capture sufficient temporal information. However, despite this shortcoming, the dynamic 320-row ADCT is the only imaging modality that allows for this type of simulation study to be performed.

4.6.5 Future directions

This work can be extended in a number of directions. As a preliminary experiment, a number of issues were highlighted and these should be addressed in subsequent work. Imaging dry-mouth, but otherwise normal subjects, would give a good test case for the no-slip boundaries. Increasing the number of subjects, as well as postures and bolus types, would improve the strength of the findings. The study of solid and semi-solid boluses would require more complex material properties definitions, measurements, and simulation techniques than those present in this study.

Another possible extension is to modify the geometry and/or timings of the boundaries in a way that mimics physical pathologies, such as base-of-

tongue tumour removal. This may help illuminate some of the underlying causes for dysphagia in patients who have had partial glossectomy with a freeflap and/or radiotherapy.

The airway could be coupled to finite-element computer models of the head and neck anatomy using software such as *ArtiSynth* [77], instead of having its deformations kinematically controlled. This would allow us to study how changes to the organs may affect the bolus flow.

4.7 Summary

This chapter presents a numerical study of six healthy oropharyngeal swallows. We test the assumption that a slip boundary condition would provide a better approximation to reality than a no-slip condition. The reasoning behind the assumption is that in normal individuals, saliva coats the aerodigestive tract and has a much lower viscosity than thickened boluses. We found that the no-slip condition gave a better approximation to the CT images when observing bolus transit times, however oropharyngeal residue after the swallow was significantly increased.

The results of the thin swallows were inconclusive. Because of the very low viscosity of water, the slip and no-slip simulations were nearly identical, and did not always agree with the CT images. Nevertheless, because of the nearly identical behaviour between slip and no-slip simulations, these results would neither support or refute the assumption being tested. It is not obvious what could have caused this result, but one possible explanation is that thin boluses move quicker than thickened boluses and the 10 Hz frame

rate of the CT images could not adequately capture the solid motion.

In the existing literature, there is conflicting evidence with respect to the effect of hyposalivation on dysphagia. Our observations corroborate with modified barium studies that indicate bolus transit times are unaffected by hyposalivation, but residue increases with hyposalivation. Further investigation in the clinic, using simulation, and in the laboratory studying saliva at the microscopic level may shed light on this complex phenomenon.

Chapter 5

Conclusion

This thesis presents a numerical study of fluid flow in the oropharynx, with the goal of understanding the relationship between saliva and dysphagia. In the current literature, there are only a handful of publications that study fluid flow in the oropharynx, and many of them used simplified geometries of the airway due to a lack of imaging modalities that could support true 3D fluid analysis. With the advent of dynamic full 3D imaging of human swallowing using 320-row ADCT, true dynamic 3D simulation is now possible. However, a number of challenges first needed to be overcome.

The first challenge is deciding on an appropriate fluid simulation technique for representing the bolus. 3D fluid simulation is a challenging problem, and simulation of swallowing requires a transient, free-surface representation and proper handling of moving boundaries. The Unified Semi-Analytic Wall (USAW) SPH method offers an attractive solution to some of these problems. However, it required extension to be able to handle moving 3D boundaries and non-Newtonian flows. With these modifications, it became suitable for the study of thickened liquids in the oropharynx. We perform partial validation of the methods through the simulation of Couette, Hagen-Poiseuille, and lid-driven cavity flows.

Extracting the airway and its motion from the ADCT data required the development of a new tool, *BlendSeg*. Using *BlendSeg*, airways from a series of ADCT scans were extracted and used to drive the modified USAW SPH simulations of the bolus. The nectar- and honey-thick boluses were thickened with starch. Their viscosity was measured using a *KINEXUS* rheometer. They are both shear thinning materials, and in the extended USAW SPH method, they were modelled as Cross-type fluids.

BlendSeg was shown to be practical and effective as it was used to extract geometry from six ADCT image sequences of healthy subjects swallowing thin, nectar-thick, and honey-thick boluses. We conducted a preliminary numerical investigation using these geometries and the extended USAW SPH method. For each of the six geometries, both no-slip and slip boundary conditions were simulated. Bolus transit times were measured and compared to measurements of the ADCT data. The results for the thin bolus simulations were inconclusive. The thickened bolus simulations suggest that in normal subjects saliva does not speed up the bolus transit times. However, the no-slip simulations had higher amounts of residue after the swallow.

Impaired saliva production is thought to cause dysphagia, however a review of the literature indicates that the relationship between them is unclear. A number of existing clinical studies have compared swallowing of subjects with hyposalivation to normals, and found that bolus transit times were unaffected in the patient group. Further, increased residue was observed in patient groups experiencing hyposalivation [43, 107], corroborating our simulation findings. On the other hand, other studies find that swallowing durations measured using anatomical landmarks increase for subjects with

hyposalivation [12, 105].

To summarize, the contributions of this thesis are firstly presenting an extension to a state-of-the-art SPH simulation method, in order to run simulations in the oropharynx with non-Newtonian liquids. A new method of manually extracting boundaries from 4D data was created and described here. This method was used to extract a boundary from dynamic ADCT data and used to represent the aerodigestive tract in our swallowing simulations. These methods were used in a preliminary examination of saliva's role in swallowing liquid boluses. The experiments suggest that saliva does not increase bolus speed, but may decrease oropharyngeal residue.

5.1 Limitations

The contributions presented in this thesis have a number of limitations. The tool developed to create moving boundaries from ADCT data, *BlendSeg*, is a tool that allows an operator to make fine, detailed adjustments to a 3D mesh. Currently we use it as the primary tool in the creation of dynamic 3D geometries. However, the process is time consuming and at risk of error. The ADCT data has a relatively low temporal resolution of 10 Hz. As a result of subject and bolus motion during the acquisition of each frame, artifacts such as blurring, ghosting, and streaking are present in the images. These artifacts confound automated registration and segmentation techniques, and also manual extraction with *BlendSeg* as boundaries become difficult to delineate.

Because the oropharyngeal bolus simulations are primarily driven by the

boundary motion, any errors in airway identification because of operator mistakes, or due to artifacts in the images, culminate in errors of the fluid simulation and may influence the results. We expect this to be the primary source of error in the oropharyngeal bolus simulations. In fact, we suspect this may contribute to the disagreement between thin bolus simulations and the ADCT data. The biggest hurdle to improving the 3D bolus simulations may be obtaining 3D data with a higher frame rate than 10 Hz.

The extended USAW SPH methods could be better validated. A stronger validation would include moving boundaries, a free surface, and non-Newtonian fluid, with a size and fluid velocity comparable to that of oropharyngeal swallowing. This type of experiment would be useful not only for validating the extended USAW SPH method, but for measuring improvements to it, and also to validate other simulation methods as they become available. A significant issue with our extension is that the non-Newtonian solver is explicit. For shear-thinning boluses, this puts a severe time step size restriction on the solver, limiting the resolution of the particles and increasing the simulation time.

Oropharyngeal swallowing is an extremely complex phenomenon. Our treatment of it was limited to the consideration of fluids. Additionally, only three healthy subjects with six swallows between them were studied. An expanded study with perhaps a dozen healthy subjects swallowing different materials would result in stronger clinical impact of the findings.

The inconsistent results of the thin bolus simulations were troubling. For the thickened boluses, a number of assumptions were made. The first is that the air in the airway does not contribute significantly to the flow of the

bolus. In terms of shearing, this is most likely a good assumption. However, without considering air explicitly, SPH can not predict the trapping of air bubbles and their effect on the flow.

The temperature of the bolus was assumed to be constant at 10°C. This is the temperature at which the rheology was measured. For all fluids, and particularly for non-Newtonian fluids, the viscosity can be a strong function of temperature. observation of the thickened boluses indicates that they are sensitive to temperature, but the sensitivity was not quantified.

The presence of amylase in saliva could also have a large effect on the bolus viscosity. In a study of starch-thickened boluses, a 1 ml volume of saliva was introduced to 10 ml of starch-thickened bolus, the viscosity of the bolus was reduced by 90% after only 10 s of mixing [44]. However, this finding seems to be sensitive to mixing. If the subject mixed saliva with the bolus vigorously before swallowing, it would likely have a large effect on the viscosity. In the ADCT study, this effect is hopefully small if the subject holds the bolus stationary in their mouth before swallowing. It is also possible that mixing with saliva occurs during the swallow, and that the bolus viscosity is decreasing during the oropharyngeal swallow. Our simulations do not account for this factor.

The resolution of the particles is another potential source of error in the swallowing simulation. Each particle has a diameter of 1 mm, and each millilitre of bolus is represented by 1000 particles. The 4 ml nectar bolus was re-run with twice the number of particles, each having a diameter of 0.8 mm, without any significant change in the bolus timing measures. However it remains a possibility that further increasing the number of particles could

have an effect on the results. For example, the upper esophageal sphincter is normally closed. This closure is represented in the model by opposing surfaces overlapping. We observed that as the particles shrink in size, more demand is placed on the airway model because smaller particles may slip through the closure if the regions do not overlap adequately. In addition, the squeezing of the stripping wave is similarly modelled by the two opposing surfaces (representing the tongue and the pharynx) pushing together. If the squeezing does not proceed in the proper peristaltic direction, instability could occur as fluid is trapped with nowhere to go. Therefore, increasing the resolution of the simulation significantly might require a faster solver, increased temporal resolution to properly resolve the stripping wave, and improved techniques for representing closure.

5.2 Future work

Looking forward, a number of future directions present themselves in the fields of fluid simulation, biomechanics, dysphagia research, and image processing. One of the most time consuming parts of this work was extracting moving boundaries from ADCT data. Finding new automated techniques that could speed up this process would significantly reduce the time it takes to study the CT data. Further improvements in the temporal resolution of ADCT data could possibly make it easier for automated methods to work, as this might decrease the severity of motion artifacts.

In our extension of USAW SPH, shear-thinning boluses integrated explicitly require very small time steps and increases the computation time

greatly. This could be alleviated by performing an implicit time integration for the viscous term, however existing implicit viscosity solvers would need to be extended to the USAW SPH formulation.

The current oropharyngeal swallowing study only included two healthy subjects swallowing liquids. More subjects of different ages and pathologies should be included in order to have a more complete picture of saliva in swallowing. Another approach forward is to gather 3D scans of subjects swallowing semi-solid and solid boluses. A large gap in knowledge exists here because of the complexity in the physics behind mastication, food breakdown, and swallowing of solid foods.

Moving away from the bolus, existing biomechanics models of the human head and neck region can now leverage the dynamic 3D ADCT scans. The imaging data provides a detailed look at the 3D motion in the oropharynx and can potentially be used to study the biomechanics of the head and neck during swallowing. A biomechanics simulation coupled to a fluid simulation of the bolus has the capability of predicting swallowing outcomes that could result from surgical or neurological changes to the body. The work presented in [116] illustrates a possible approach to achieving this coupling by using a unified skinning technique.

In dysphagia research, the observations of the simulation should be further corroborated with clinical studies. These could be done by re-analyzing older data, or by designing new studies that complement the simulation data. Saliva is a complex fluid and so far, most dysphagia research has focused on quantity of saliva. Studying the molecular changes in saliva due to medications and radiotherapy, and its effect on swallowing, may be a fruitful area

of research.

Bibliography

[1] Rebecca H Affoo, Norine Foley, Rushlee Garrick, Walter L Siqueira, and Ruth E Martin. Meta-analysis of salivary flow rates in young and older adults. *Journal of the American Geriatrics Society*, 63(10):2142–2151, 2015.

[2] Sug-Joon Ahn, Ling Tsou, C Antonio Sánchez, Sidney Fels, and Ho-Beom Kwon. Analyzing center of rotation during opening and closing movements of the mandible using computer simulations. *Journal of biomechanics*, 48(4):666–671, 2015.

[3] Matteo Antuono, Andrea Colagrossi, Salvatore Marrone, and Diego Molteni. Free-surface flows solved by means of sph schemes with numerical diffusive terms. *Computer Physics Communications*, 181(3):532–549, 2010.

[4] David Baraff, Andrew Witkin, and Michael Kass. Untangling cloth. In *ACM Transactions on Graphics (TOG)*, volume 22, pages 862–870. ACM, 2003.

[5] Christopher Batty, Florence Bertails, and Robert Bridson. A fast vari-

ational framework for accurate solid-fluid coupling. In *ACM Transactions on Graphics (TOG)*, volume 26, page 100. ACM, 2007.

[6] Ted Belytschko, Yury Krongauz, Daniel Organ, Mark Fleming, and Petr Krysl. Meshless methods: an overview and recent developments. *Computer methods in applied mechanics and engineering*, 139(1):3–47, 1996.

[7] Ted Belytschko, Yun Yun Lu, and Lei Gu. Element-free galerkin methods. *International journal for numerical methods in engineering*, 37(2):229–256, 1994.

[8] M Bergdahl and J Bergdahl. Low unstimulated salivary flow and subjective oral dryness: association with medication, anxiety, depression, and stress. *Journal of Dental Research*, 79(9):1652–1658, 2000.

[9] Richard P Beyer. A computational model of the cochlea using the immersed boundary method. *Journal of Computational Physics*, 98(1):145–162, 1992.

[10] J Bonet, S Kulasegaram, MX Rodriguez-Paz, and M Profit. Variational formulation for the smooth particle hydrodynamics (sph) simulation of fluid and solid problems. *Computer Methods in Applied Mechanics and Engineering*, 193(12):1245–1256, 2004.

[11] JU Brackbill and HM Ruppel. Flip: A method for adaptively zoned, particle-in-cell calculations of fluid flows in two dimensions. *Journal of Computational Physics*, 65(2):314–343, 1986.

[12] Anthony J Caruso, Barbara C Sonies, Jane C Atkinson, and Philip C Fox. Objective measures of swallowing in patients with primary sjögren's syndrome. *Dysphagia*, 4(2):101–105, 1989.

[13] Thanapong Chaichana, Zhonghua Sun, and James Jewkes. Computation of hemodynamics in the left coronary artery with variable angulations. *Journal of biomechanics*, 44(10):1869–1878, 2011.

[14] Michael W. Chang, Eugene Lin, and Jenq-Neng Hwang. Contour tracking using a knowledge-based snake algorithm to construct three-dimensional pharyngeal bolus movement. *Dysphagia*, 14(4):219–227, 1999.

[15] Michael W. Chang, Brigette Rosendall, and Bruce A. Finlayson. Mathematical modeling of normal pharyngeal bolus transport; a preliminary study. *Journal of rehabilitation research and development*, 35:327–334, 1998.

[16] Med Chaos. Normal epiglottis, 2013.

[17] Gloria Chi-Fishman. Quantitative lingual, pharyngeal and laryngeal ultrasonography in swallowing research: a technical review. *Clinical linguistics & phonetics*, 19(6-7):589–604, 2005.

[18] PW Cleary, J Ha, M Prakash, and T Nguyen. 3d sph flow predictions and validation for high pressure die casting of automotive components. *Applied Mathematical Modelling*, 30(11):1406–1427, 2006.

[19] Andrea Colagrossi and Maurizio Landrini. Numerical simulation of in-

terfacial flows by smoothed particle hydrodynamics. *Journal of Computational Physics, Volume 191, Issue 2, p. 448-475.*, 191:448–475, nov 2003.

[20] LMC Collins and C Dawes. The surface area of the adult human mouth and thickness of the salivary film covering the teeth and oral mucosa. *Journal of dental research*, 66(8):1300–1302, 1987.

[21] Ian J Cook, Wylie J Dodds, RO Dantas, Benson Massey, Mark K Kern, Ivan M Lang, James G Brasseur, and WJ Hogan. Opening mechanisms of the human upper esophageal sphincter. *American Journal of Physiology-Gastrointestinal and Liver Physiology*, 257(5):G748–G759, 1989.

[22] Sharen J. Cummins and Murray Rudman. An sph projection method. *Journal of computational physics*, 152(2):584–607, 1999.

[23] Kristopher S Cunningham and Avrum I Gotlieb. The role of shear stress in the pathogenesis of atherosclerosis. *Laboratory investigation*, 85(1):9–23, 2005.

[24] Jérôme Declerck, Jacques Feldmar, and Nicholas Ayache. Definition of a four-dimensional continuous planispheric transformation for the tracking and the analysis of left-ventricle motion. *Medical Image Analysis*, 2(2):197–213, 1998.

[25] W.J. Dodds. The physiology of swallowing. *Dysphagia*, 3(4):171–178, 1989.

[26] J Donea, Antonio Huerta, J-Ph Ponthot, and A Rodriguez-Ferran. Encyclopedia of computational mechanics vol. 1: Fundamentals., chapter 14: Arbitrary lagrangian-eulerian methods, 2004.

[27] Jim Douglas and James E Gunn. A general formulation of alternating direction methods. *Numerische Mathematik*, 6(1):428–453, 1964.

[28] John W Eveson. Xerostomia. *Periodontology 2000*, 48(1):85–91, 2008.

[29] EA Fadlun, R Verzicco, Paolo Orlandi, and J Mohd-Yusof. Combined immersed-boundary finite-difference methods for three-dimensional complex flow simulations. *Journal of computational physics*, 161(1):35–60, 2000.

[30] X-J Fan, RI Tanner, and R Zheng. Smoothed particle hydrodynamics simulation of non-newtonian moulding flow. *Journal of Non-Newtonian Fluid Mechanics*, 165(5):219–226, 2010.

[31] Stanley Osher Ronald Fedkiw and S Osher. Level set methods and dynamic implicit surfaces. *Surfaces*, 44:77, 2002.

[32] Martin Ferrand, D. R. Laurence, B. D. Rogers, Damien Violeau, and Christophe Kassiotis. Unified semi-analytical wall boundary conditions for inviscid, laminar or turbulent flows in the meshless sph method. *International Journal for Numerical Methods in Fluids*, 71(4):446–472, 2013.

[33] Cormac Flynn, Ian Stavness, John Lloyd, and Sidney Fels. A finite element model of the face including an orthotropic skin model under

in vivo tension. *Computer Methods in Biomechanics and Biomedical Engineering*, 0(0):1–12, 0. PMID: 23919890.

[34] Philip C Fox, Peter F van der Ven, Barbara C Sonies, James M Weiffenbach, and Bruce J Baum. Xerostomia: evaluation of a symptom with increasing significance. *The Journal of the American Dental Association*, 110(4):519–525, 1985.

[35] Robert I Fox, Michael Stern, and Paul Michelson. Update in sjögren syndrome. *Current opinion in rheumatology*, 12(5):391–398, 2000.

[36] Naoko Fujii, Yoko Inamoto, Eiichi Saitoh, Mikoto Baba, Sumiko Okada, Satoshi Yoshioka, Toshiaki Nakai, Yoshihiro Ida, Kazuhiro Katada, and Jeffrey B Palmer. Evaluation of swallowing using 320-detector-row multislice ct. part i: single- and multiphase volume scanning for three-dimensional morphological and kinematic analysis. *Dysphagia*, 26(2):99–107, 2011.

[37] P Garcia-Peris, L Parón, C Velasco, C De la Cuerda, M Camblor, I Bretón, H Herencia, J Verdaguer, C Navarro, and P Clave. Long-term prevalence of oropharyngeal dysphagia in head and neck cancer patients: impact on quality of life. *Clinical Nutrition*, 26(6):710–717, 2007.

[38] Donna T Geddes, Lynda M Chadwick, Jacqueline C Kent, Catherine P Garbin, and Peter E Hartmann. Ultrasound imaging of infant swallowing during breast-feeding. *Dysphagia*, 25(3):183–191, 2010.

[39] U. K. N. G. Ghia, Kirti N. Ghia, and C. T. Shin. High-re solutions for incompressible flow using the navier-stokes equations and a multigrid method. *Journal of computational physics*, 48(3):387–411, 1982.

[40] Robert A Gingold and Joseph J Monaghan. Smoothed particle hydrodynamics: theory and application to non-spherical stars. *Monthly notices of the royal astronomical society*, 181(3):375–389, 1977.

[41] Henry Gray. *Anatomy of the human body*. Lea & Febiger, 1918.

[42] S. Hamlet, L. Jones, R. Mathog, M. Bolton, and R. Patterson. Bolus propulsive activity of the tongue in dysphagic cancer patients. *Dysphagia*, 3(1):18–23, 1988.

[43] Sandra Hamlet, Jennifer Faull, Barbara Klein, Amr Aref, James Fontanesi, Robert Stachler, Falah Shamsa, Lewis Jones, and Mark Simpson. Mastication and swallowing in patients with postirradiation xerostomia. *International Journal of Radiation Oncology* Biology* Physics*, 37(4):789–796, 1997.

[44] Ben Hanson, Mark T OLeary, and Christina H Smith. The effect of saliva on the viscosity of thickened drinks. *Dysphagia*, 27(1):10–19, 2012.

[45] Negar M Harandi, Jonghye Woo, Maureen Stone, Rafeef Abugharbieh, and Sidney Fels. Subject-specific biomechanical modelling of the tongue: analysis of muscle activations during speech. *Proc Int Semin Speech Prod (ISSP)*, pages 174–177, 2014.

[46] Francis H. Harlow and J. Eddie Welch. Numerical calculation of time-dependent viscous incompressible flow of fluid with free surface. *Physics of Fluids, Volume 8, Issue 12, p.2182-2189*, 8:2182–2189, dec 1965.

[47] H Ric Harnsberger. *Handbook of head and neck imaging*. Mosby Incorporated, 1995.

[48] Simon M Harrison, Paul W Cleary, Graham Eyres, Matthew D Sinnott, and Leif Lundin. Challenges in computational modelling of food breakdown and flavour release. *Food & function*, 5(11):2792–2805, 2014.

[49] Simon M. Harrison, Graham Eyres, Paul W. Cleary, Matthew D. Sinnott, Conor Delahunty, and Leif Lundin. Computational modeling of food oral breakdown using smoothed particle hydrodynamics. *Journal of Texture Studies*, 45(2):97–109, 2014.

[50] Hellerhoff. Normaler schluck-11, 2011.

[51] BS Henson, MR Inglehart, A Eisbruch, and JA Ship. Preserved salivary output and xerostomia-related quality of life in head and neck cancer patients receiving parotid-sparing radiotherapy. *Oral oncology*, 37(1):84–93, 2001.

[52] Cyril W. Hirt and Billy D. Nichols. Volume of fluid (vof) method for the dynamics of free boundaries. *Journal of computational physics*, 39(1):201–225, 1981.

[53] Susan G Hiss and Gregory N Postma. Fiberoptic endoscopic evaluation of swallowing. *The Laryngoscope*, 113(8):1386–1393, 2003.

[54] Andrew Kenneth Ho, Yoko Inamoto, Eiichi Saitoh, Sheldon Green, and Sidney Fels. Extracting moving boundaries from dynamic, multi-slice ct images for fluid simulation. *Computer Methods in Biomechanics and Biomedical Engineering: Imaging & Visualization*, pages 1–6, 2016.

[55] Andrew Kenneth Ho, Ling Tsou, Sheldon Green, and Sidney Fels. A 3d swallowing simulation using smoothed particle hydrodynamics. *Computer Methods in Biomechanics and Biomedical Engineering: Imaging & Visualization*, 2(4):237–244, 2014.

[56] SM Hosseini, MT Manzari, and SK Hannani. A fully explicit three-step sph algorithm for simulation of non-newtonian fluid flow. *International Journal of Numerical Methods for Heat & Fluid Flow*, 17(7):715–735, 2007.

[57] Yoko Inamoto, Naoko Fujii, Eiichi Saitoh, Mikoto Baba, Sumiko Okada, Kazuhiro Katada, Yasunori Ozeki, Daisuke Kanamori, and Jeffrey B Palmer. Evaluation of swallowing using 320-detector-row multislice ct. part ii: kinematic analysis of laryngeal closure during normal swallowing. *Dysphagia*, 26(3):209–17, 2011.

[58] Razvan Ioan Ionasec, Ingmar Voigt, Bogdan Georgescu, Yang Wang, Helene Houle, Fernando Vega-Higuera, Nassir Navab, and Dorin Comaniciu. Patient-specific modeling and quantification of the aortic

and mitral valves from 4-d cardiac ct and tee. *IEEE transactions on medical imaging*, 29(9):1636–1651, 2010.

[59] Barbara M Johnston, Peter R Johnston, Stuart Corney, and David Kilpatrick. Non-newtonian blood flow in human right coronary arteries: steady state simulations. *Journal of biomechanics*, 37(5):709–720, 2004.

[60] Barbara M Johnston, Peter R Johnston, Stuart Corney, and David Kilpatrick. Non-newtonian blood flow in human right coronary arteries: transient simulations. *Journal of biomechanics*, 39(6):1116–1128, 2006.

[61] Peter J Kahrilas, Shezhang Lin, Jim Chen, and Jerilyn A Logemann. Three-dimensional modeling of the oropharynx during swallowing. *Radiology*, 194(2):575–579, 1995.

[62] Peter J Kahrilas, Shezhang Lin, Jerilyn A Logemann, Gulchin A Ergun, and Frank Facchini. Deglutitive tongue action: volume accommodation and bolus propulsion. *Gastroenterology*, 104(1):152–162, 1993.

[63] Takahiro Kikuchi, Yukihiro Michiwaki, Tetsu Kamiya, Yoshio Toyama, Tasuku Tamai, and Seiichi Koshizuka. Human swallowing simulation based on videofluorography images using hamiltonian mps method. *Computational Particle Mechanics*, 2(3):247–260, 2015.

[64] John Kim and Parviz Moin. Application of a fractional-step method to incompressible navier-stokes equations. *Journal of computational physics*, 59(2):308–323, 1985.

[65] Jungwoo Kim, Dongjoo Kim, and Haecheon Choi. An immersed-boundary finite-volume method for simulations of flow in complex geometries. *Journal of Computational Physics, Volume 171, Issue 1, pp. 132-150 (2001).*, 171:132–150, jul 2001.

[66] Stefan Klein, Marius Staring, Keelin Murphy, Max A Viergever, and Josien PW Pluim. Elastix: a toolbox for intensity-based medical image registration. *Medical Imaging, IEEE Transactions on*, 29(1):196–205, 2010.

[67] Seiichi Koshizuka, Atsushi Nobe, and Yoshiaki Oka. Numerical analysis of breaking waves using the moving particle semi-implicit method. *International Journal for Numerical Methods in Fluids*, 26(7):751–769, 1998.

[68] Seiichi Koshizuka and Y Oka. Moving-particle semi-implicit method for fragmentation of incompressible fluid. *Nuclear science and engineering*, 123(3):421–434, 1996.

[69] Sivakumar Kulasegaram, Javier Bonet, RW Lewis, and M Profit. A variational formulation based contact algorithm for rigid boundaries in two-dimensional sph applications. *Computational Mechanics*, 33(4):316–325, 2004.

[70] William E Langlois and Michel O Deville. *Slow viscous flow*. Springer, 1964.

[71] E.-S. Lee, C. Moulinec, R. Xu, D. Violeau, D. Laurence, and P. Stansby. Comparisons of weakly compressible and truly incom-

pressible algorithms for the sph mesh free particle method. *Journal of Computational Physics, Volume 227, Issue 18, p. 8417-8436.*, 227:8417–8436, sep 2008.

[72] Agnes Leroy, Damien Violeau, Martin Ferrand, and Christophe Kassiotis. Unified semi-analytical wall boundary conditions applied to 2-d incompressible sph. *Journal of Computational Physics*, 261:106–129, 2014.

[73] Shezhang Lin, Jim Chen, Paul Hertz, and Peter J. Kahrilas. Dynamic reconstruction of the orophanryngeal swallow using computer based animation. *Computerized medical imaging and graphics*, 20(2):69–75, 1996.

[74] Xiang Lin, Brett R Cowan, and Alistair A Young. Automated detection of left ventricle in 4d mr images: experience from a large study. In *International Conference on Medical Image Computing and Computer-Assisted Intervention*, pages 728–735. Springer, 2006.

[75] G.R. Liu and MB Liu. *Smoothed particle hydrodynamics: a meshfree particle method*. World Scientific Pub Co Inc, 2003.

[76] M. B. Liu and G. R. Liu. Smoothed particle hydrodynamics (sph): an overview and recent developments. *Archives of computational methods in engineering*, 17(1):25–76, 2010.

[77] John E. Lloyd, Ian Stavness, and Sidney Fels. Artisynth: a fast interactive biomechanical modeling toolkit combining multibody and finite

element simulation. In *Soft tissue biomechanical modeling for computer assisted surgery*, pages 355–394. Springer, 2012.

[78] Jeri A Logemann, PETER J Kahrilas, JOAN Cheng, BR Pauloski, PATRICIA J Gibbons, ALFRED W Rademaker, and SHEZHANG Lin. Closure mechanisms of laryngeal vestibule during swallow. *American Journal of Physiology-Gastrointestinal and Liver Physiology*, 262(2):G338–G344, 1992.

[79] Vincent Luboz, Antoine Perrier, Ian Stavness, JE Lloyd, Marek Bucki, Francis Cannard, Bruno Diot, Nicolas Vuillerme, and Yohan Payan. Foot ulcer prevention using biomechanical modelling. *Computer Methods in Biomechanics and Biomedical Engineering: Imaging & Visualization*, 2(4):189–196, 2014.

[80] Leon B Lucy. A numerical approach to the testing of the fission hypothesis. *The astronomical journal*, 82:1013–1024, 1977.

[81] Michael Lynch, Ovidiu Ghita, and Paul F Whelan. Segmentation of the left ventricle of the heart in 3-d+ t mri data using an optimized nonrigid temporal model. *IEEE Transactions on Medical Imaging*, 27(2):195–203, 2008.

[82] M Malvè, A Garcia, J Ohayon, and MA Martinez. Unsteady blood flow and mass transfer of a human left coronary artery bifurcation: Fsi vs. cfd. *International communications in heat and mass transfer*, 39(6):745–751, 2012.

[83] S Marrone, M Antuono, A Colagrossi, G Colicchio, D Le Touzé, and G Graziani. δ-sph model for simulating violent impact flows. *Computer Methods in Applied Mechanics and Engineering*, 200(13):1526–1542, 2011.

[84] Bonnie Martin-Harris, Martin B Brodsky, Yvonne Michel, Donald O Castell, Melanie Schleicher, John Sandidge, Rebekah Maxwell, and Julie Blair. Mbs measurement tool for swallow impairment–mbsimp: establishing a standard. *Dysphagia*, 23(4):392–405, 2008.

[85] Arno Mayrhofer, Martin Ferrand, Christophe Kassiotis, Damien Violeau, and François-Xavier Morel. Unified semi-analytical wall boundary conditions in sph: analytical extension to 3-d. *Numerical Algorithms*, 68(1):15–34, 2015.

[86] Tim McInerney and Demetri Terzopoulos. A dynamic finite element surface model for segmentation and tracking in multidimensional medical images with application to cardiac 4d image analysis. *Computerized Medical Imaging and Graphics*, 19(1):69–83, 1995.

[87] Y. Meng, M. A. Rao, and A. K. Datta. Computer simulation of the pharyngeal bolus transport of newtonian and non-newtonian fluids. *Food and bioproducts processing*, 83(4):297–305, 2005.

[88] Rajat Mittal and Gianluca Iaccarino. Immersed boundary methods. *Annual Review of Fluid Mechanics, vol. 37, Issue 01, pp.239-261*, 37:239–261, jan 2005.

[89] H. Mizunuma, M. Sonomura, K. Shimokasa, H. Ogoshi, S. Nakamura, and N. Tayama. Numerical modeling and simulation on the swallowing of jelly. *Journal of texture studies*, 40(4):406–426, 2009.

[90] J Mohd-Yusof. Combined immersed-boundary/b-spline methods for simulations of ow in complex geometries. *Annual Research Briefs. NASA Ames Research Center= Stanford University Center of Turbulence Research: Stanford*, pages 317–327, 1997.

[91] Joe J. Monaghan. Smoothed particle hydrodynamics. *Annual review of astronomy and astrophysics*, 30:543–574, 1992.

[92] Joe J. Monaghan. Simulating free surface flows with sph. *Journal of computational physics*, 110(2):399–406, 1994.

[93] Johan Montagnat and Hervé Delingette. 4d deformable models with temporal constraints: application to 4d cardiac image segmentation. *Med Image Anal*, 9(1):87–100, 2005.

[94] Joseph P. Morris. Simulating surface tension with smoothed particle hydrodynamics. *International journal for numerical methods in fluids*, 33(3):333–353, 2000.

[95] Joseph P. Morris, Patrick J. Fox, and Yi Zhu. Modeling low reynolds number incompressible flows using sph. *Journal of computational physics*, 136(1):214–226, 1997.

[96] M.A. Nicosia, J.A. Hind, E.B. Roecker, M. Carnes, J. Doyle, G.A. Dengel, and J.A. Robbins. Age effects on the temporal evolution of

isometric and swallowing pressure. *The Journals of Gerontology Series A: Biological Sciences and Medical Sciences*, 55(11):M634, 2000.

[97] Mark A Nicosia. A planar finite element model of bolus containment in the oral cavity. *Comput. Biol. Med.*, 37(10):1472–8, 2007.

[98] Mark A. Nicosia. Theoretical estimation of shear rate during the oral phase of swallowing: effect of partial slip. *Journal of Texture Studies*, 44(2):132–139, 2013.

[99] Mark A. Nicosia and JoAnne Robbins. The fluid mechanics of bolus ejection from the oral cavity. *Journal of Biomechanics*, 34(12):1537–1544, 2001.

[100] Kerstin E Öhrn, Ylva-Britt Wahlin, and Per-Olow Sjödén. Oral status during radiotherapy and chemotherapy: a descriptive study of patient experiences and the occurrence of oral complications. *Supportive care in cancer*, 9(4):247–257, 2001.

[101] Barbara Roa Pauloski, Alfred W Rademaker, Jerilyn A Logemann, Muveddet Discekici-Harris, and Bharat B Mittal. Comparison of swallowing function after intensity-modulated radiation therapy and conventional radiotherapy for head and neck cancer. *Head & neck*, 37(11):1575–1582, 2015.

[102] Charles S Peskin. The immersed boundary method. *Acta numerica*, 11:479–517, 2002.

[103] Philippe Poisson, Thibault Laffond, Sandra Campos, Veronique

Dupuis, and Isabelle Bourdel-Marchasson. Relationships between oral health, dysphagia and undernutrition in hospitalised elderly patients. *Gerodontology*, 2014.

[104] Panu JF Rantonen and Jukka H Meurman. Viscosity of whole saliva. *Acta Odontologica Scandinavica*, 56(4):210–214, 1998.

[105] Nelson L Rhodus, Stephen Colby, Karlind Moller, and Janna Bereuter. Quantitative assessment of dysphagia in patients with primary and secondary sjögren's syndrome. *Oral Surgery, Oral Medicine, Oral Pathology, Oral Radiology, and Endodontology*, 79(3):305–310, 1995.

[106] Nicole M Rogus-Pulia, Charles Larson, Bharat B Mittal, Marge Pierce, Steven Zecker, Korey Kennelty, Amy Kind, and Nadine P Connor. Effects of change in tongue pressure and salivary flow rate on swallow efficiency following chemoradiation treatment for head and neck cancer. *Dysphagia*, pages 1–10, 2016.

[107] Nicole M Rogus-Pulia and Jeri A Logemann. Effects of reduced saliva production on swallowing in patients with sjögrens syndrome. *Dysphagia*, 26(3):295–303, 2011.

[108] James Albert Sethian. *Level set methods and fast marching methods: evolving interfaces in computational geometry, fluid mechanics, computer vision, and materials science*, volume 3. Cambridge university press, 1999.

[109] Songdong Shao and Edmond Y. M. Lo. Incompressible sph method for simulating newtonian and non-newtonian flows with a free sur-

face. *Advances in Water Resources, Volume 26, Issue 7, p. 787-800.*, 26:787–800, n/a 2003.

[110] Leonardo Di G. Sigalotti, Jaime Klapp, Eloy Sira, Yasmin Meleán, and Anwar Hasmy. Sph simulations of time-dependent poiseuille flow at low reynolds numbers. *Journal of Computational Physics, Volume 191, Issue 2, p. 622-638.*, 191:622–638, nov 2003.

[111] BC Sonies, JA Ship, and BJ Baum. Relationship between saliva production and oropharyngeal swallow in healthy, different-aged adults. *Dysphagia*, 4(2):85–89, 1989.

[112] M. Sonomura, H. Mizunuma, T. Numamori, H. Michiwaki, and K. Nishinari. Numerical simulation of the swallowing of liquid bolus. *Journal of Texture Studies*, 42(3):203–211, 2011.

[113] Leo M Sreebny and Steven S Schwartz. A reference guide to drugs and dry mouth–2nd edition. *Gerodontology*, 14(1):33–47, 1997.

[114] Leo M Sreebny and Arjan Vissink. *Dry mouth, the malevolent symptom: a clinical guide*. John Wiley & Sons, 2010.

[115] Ian Stavness, John E Lloyd, and Sidney Fels. Automatic prediction of tongue muscle activations using a finite element model. *Journal of biomechanics*, 45(16):2841–2848, 2012.

[116] Ian Stavness, C Antonio Sánchez, John Lloyd, Andrew Ho, Johnty Wang, Sidney Fels, and Danny Huang. Unified skinning of rigid and

deformable models for anatomical simulations. In *SIGGRAPH Asia 2014 Technical Briefs*, page 9. ACM, 2014.

[117] H. S. Udaykumar, R. Mittal, P. Rampunggoon, and A. Khanna. A sharp interface cartesian grid method for simulating flows with complex moving boundaries. *Journal of Computational Physics, Volume 174, Issue 1, pp. 345-380 (2001).*, 174:345–380, nov 2001.

[118] Martin Uecker, Shuo Zhang, Dirk Voit, Alexander Karaus, Klaus-Dietmar Merboldt, and Jens Frahm. Real-time mri at a resolution of 20 ms. *NMR Biomed*, 23(8):986–94, 2010.

[119] Tom Vercauteren, Xavier Pennec, Aymeric Perchant, and Nicholas Ayache. Diffeomorphic demons: Efficient non-parametric image registration. *NeuroImage*, 45(1):S61–S72, 2009.

[120] Holger Wendland. Piecewise polynomial, positive definite and compactly supported radial functions of minimal degree. *Advances in computational Mathematics*, 4(1):389–396, 1995.

[121] Frank M White and Isla Corfield. *Viscous fluid flow*, volume 3. McGraw-Hill New York, 2006.

[122] Xiaoyang Xu, Jie Ouyang, Binxin Yang, and Zhijun Liu. Sph simulations of three-dimensional non-newtonian free surface flows. *Computer Methods in Applied Mechanics and Engineering*, 256:101–116, 2013.

[123] Shuo Zhang, Arno Olthoff, and Jens Frahm. Real-time magnetic reso-

nance imaging of normal swallowing. *Journal of Magnetic Resonance Imaging*, 35(6):1372–1379, 2012.

[124] Luoding Zhu and Charles S Peskin. Simulation of a flapping flexible filament in a flowing soap film by the immersed boundary method. *Journal of Computational Physics*, 179(2):452–468, 2002.

[125] Yongning Zhu and Robert Bridson. Animating sand as a fluid. In *ACM Transactions on Graphics (TOG)*, volume 24, pages 965–972. ACM, 2005.

Appendix A

Estimate of effect of saliva on a gravity driven bolus

To estimate the influence of a thin layer of lubrication on a gravity driven flow, we assume a geometry of a flat wall, perpendicular to the ground. Two layers of fluid exist between the wall and the air: a higher viscosity fluid that is closer to the air, and a lower viscosity lubricating layer that is between the first fluid and the wall (see Figure A.1).

The lubricating layer has a viscosity μ_s, and thickness L_s, while the thicker fluid viscosity μ_b and thickness L_b. Gravity drives the flow downwards in the negative y direction. The density of the two fluids is assumed to be equal, $\rho = \rho_s = \rho_b$.

For a fluid element as shown in Figure A.2, τ_w is the stress from the wall, and $\tau(x)$ is the stress at distance x from the wall. Setting up the force balance equation,

$$\sum F_y = 0, \tag{A.1}$$

$$HD\tau_w - HD\tau(x) = Mg = \rho g HDx, \tag{A.2}$$

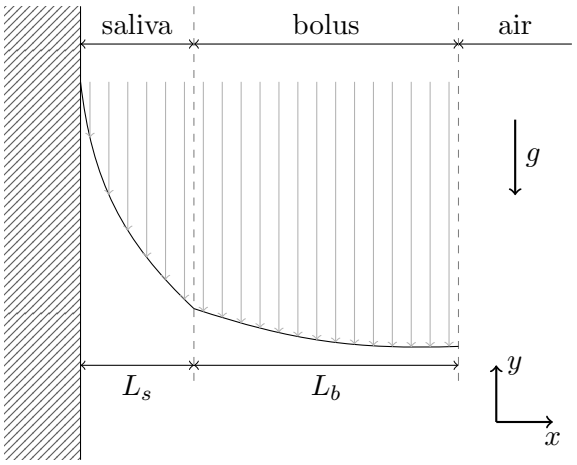

Figure A.1: Simplified geometry of a gravity driven bolus with lubricating saliva layer. Wall is on the left, gray arrows represent the velocity of the bolus. The g arrow shows the direction of gravity. L_s and L_b are the widths of the saliva and bolus, resp.

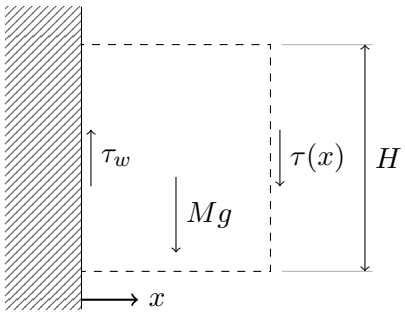

Figure A.2: Fluid element (dashed box) under consideration with height H depth D into the page. τ_w is the shear stress at the wall, and $\tau(x)$ is the shear stress at position x. Mg is the force of gravity on the element.

with boundary conditions

$$HD\tau_w = \rho g HD(L_s + L_b), \tag{A.3}$$

where $\tau(L_s + L_b) = 0$ because the shear stress due to air is negligible.

Therefore

$$\rho g HD(L_s + L_b) - HD\tau(x) = \rho g HDx, \tag{A.4}$$

$$\tau(x) = \rho g(L_s + L_b - x). \tag{A.5}$$

Inside the saliva, for a velocity $V(x)$,

$$\tau(x) = \mu_s \frac{dV}{dx}, \tag{A.6}$$

$$\frac{dV}{dx} = \frac{\rho g}{\mu_s}(L_s + L_b - x), \tag{A.7}$$

$$V(x) = \frac{\rho g}{\mu_s}\left((L_s + L_b)x - \frac{x^2}{2}\right) + C_1, \tag{A.8}$$

But $V(0) = 0$ due to the no-slip condition, therefore $C_1 = 0$

$$V(x) = \frac{\rho g}{\mu_s}\left((L_s + L_b)x - \frac{x^2}{2}\right), \quad x \leq L_s, \tag{A.9}$$

and

$$V(L_s) = \frac{\rho g}{\mu_s}\left(\frac{L_s^2}{2} + L_s L_b\right). \tag{A.10}$$

In the bolus,

$$\frac{dV}{dx} = \frac{\rho g}{\mu_b}(L_s + L_b - x), \tag{A.11}$$

$$V(x) = \frac{\rho g}{\mu_b}\left((L_s + L_b)x - \frac{x^2}{2}\right) + C_2, \tag{A.12}$$

and using the condition that the velocity at L_s is continuous,

$$C_2 = (\frac{\rho g}{\mu_s} - \frac{\rho g}{\mu_b})\left(\frac{L_s^2}{2} + L_s L_b\right) = \frac{\rho g}{\mu_s \mu_b}(\mu_b - \mu_s)\left(\frac{L_s^2}{2} + L_s L_b\right). \tag{A.13}$$

The volumetric flow rate Q is the amount of fluid flowing through a fixed plane, and is defined for the bolus as

$$Q = \int_{L_s}^{L_s+L_b} V(x) \cdot D dx. \tag{A.14}$$

Combining equations A.12−A.14,

$$Q = D\int_{L_s}^{L_s+L_b} \frac{\rho g}{\mu_b}\left[(L_s + L_b)x - \frac{x^2}{2}\right] + \frac{\rho g}{\mu_s \mu_b}(\mu_b - \mu_s)\left(\frac{L_s^2}{2} + L_s L_b\right) dx, \tag{A.15}$$

$$Q = \frac{\rho g D}{\mu_b}\left[(L_s + L_b)\frac{x^2}{2} - \frac{x^3}{6}\right]_{L_s}^{L_s+L_b} + \frac{\rho g D(\mu_b - \mu_s)L_b}{\mu_s \mu_b}\left(\frac{L_s^2}{2} + L_s L_b\right), \tag{A.16}$$

$$Q = \frac{\rho g D}{6\mu_b}(3L_s^2 L_b + 6L_s L_b^2 + 2L_b^3) + \frac{\rho g D(\mu_b - \mu_s)L_b}{\mu_s \mu_b}\left(\frac{L_s^2}{2} + L_s L_b\right). \quad \text{(A.17)}$$

Notice that the first term for Q in equation A.17 is independent of the viscosity of saliva, while the second term does depend on it. Taking the ratio of the second term to the first term and then simplifying gives us an estimate, which we call R_s, of how much saliva contributes to the overall bolus flow rate, assuming steady state.

$$R_s = \frac{3(\mu_b - \mu_s)}{\mu_s}\frac{L_s^2 + 2L_s L_b}{3L_s^2 + 6L_s L_b + 2L_b^2}\ . \quad \text{(A.18)}$$

Using equation A.18 and assuming the viscosity $\mu_b = 200\mu_s$, for R_s to have a value less than 0.1 (a 10% increase in bolus flow rate due to saliva), $L_b \approx 6000\ L_s$.

Appendix B

Using full-slip to approximate a lubricative saliva layer

In this appendix, we show that a full-slip boundary condition can be used to approximate viscous bolus flow with a lubricative saliva layer. Depending on the choices of saliva viscosity and thickness, a full-slip condition gives a reasonable approximation for time durations similar to those encountered in swallowing.

Oropharyngeal swallowing occurs in less than one second, and the time required for the bolus to leave the oral cavity is much shorter. A time-dependent finite volume (FV) solution of the velocity and flow-rates for a two material, gravity driven flow in a pipe (Figure B.1) is described and analyzed. The solver is verified by comparison with the theoretical transient and steady-state solutions, and shown to have second-order convergence in space.

The geometry is axisymmetric with two Newtonian materials representing the bolus and the saliva. An air core can be included in the model and

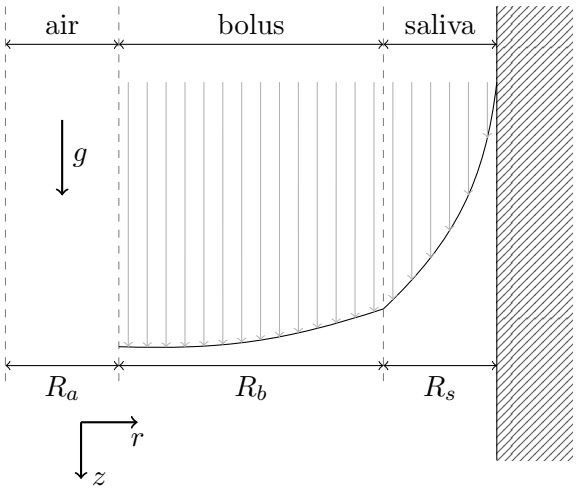

Figure B.1: Simplified geometry of a gravity driven bolus with lubricating saliva layer. Wall is on the right, gray arrows represent the fluid velocity. The g arrow shows the direction of gravity. R_a, R_b and R_s are the widths of the air core, bolus, and saliva, resp. Axial symmetry is assumed, with the centre of the air core at $r = 0$. The geometry has a total radius of $R = R_a + R_b + R_s$.

does not exert shear forces on the bolus. All fluids are assumed to be initially stationary and driven by gravity. A transient analysis shows that for the time durations associated with swallowing, and for realistic choices of saliva radius and viscosity, the full-slip boundary condition gives a reasonable approximation to the expected flow rate.

B.1 Problem description and assumptions

A layer of saliva is sandwiched between a solid stationary wall and a layer of bolus. The saliva and bolus are assumed to have Newtonian viscosities μ_s and μ_b, with radii R_s and R_b. They are assumed to have equal density, ρ. An air core is at the centre of the pipe, with radius R_a, and does not exert any shear forces on the bolus. The total pipe radius is $R = R_a + R_b + R_s$. A constant pressure gradient drives the flow with acceleration g. At time zero the velocity is zero everywhere.

We assume the flow is axisymmetric and infinite in the z direction. These assumptions simplify the Navier-Stokes equations in fluid m (where m could be bolus or saliva) to

$$\frac{\partial u_y}{\partial t} = \frac{\mu_m}{\rho_m}\frac{1}{r}\frac{\partial}{\partial r}\left(r\frac{\partial u_y}{\partial r}\right) + g. \tag{B.1}$$

The velocity between saliva and wall is no-slip.

$$u_y(R) = 0. \tag{B.2}$$

The air exerts no shear stress on the fluid

$$\frac{\partial u_y}{\partial r}(R_a) = 0. \tag{B.3}$$

The velocity of the saliva and bolus are equal at the saliva-bolus interface,

$$u_y(R_a + R_b)^- = u_y(R_a + R_b)^+, \tag{B.4}$$

as are their stresses:

$$\tau_s(R_a + R_b) = \tau_b(R_a + R_b) \tag{B.5}$$

$$\mu_s \frac{\partial u_y}{\partial r}(R_a + R_b)^- = \mu_b \frac{\partial u_y}{\partial r}(R_a + R_b)^+ \tag{B.6}$$

The $+$ and $-$ superscripts indicate a small distance to the left and right of R_x, resp.

B.1.1 Steady-state solution

The theoretical steady-state solution can be derived as follows,

$$\frac{\partial u_y}{\partial t} = \frac{\mu_m}{\rho_m} \frac{1}{r} \frac{\partial}{\partial r} \left(r \frac{\partial u_y}{\partial r} \right) + g. \tag{B.7}$$

and at steady state,

$$0 = \frac{\mu_m}{\rho_m} \frac{1}{r} \frac{\partial}{\partial r} \left(r \frac{\partial u_y}{\partial r} \right) + g. \tag{B.8}$$

At this point we drop the subscript y from the velocity. Inside the saliva, $R_a + R_b \leq r \leq R_a + R_b + R_s$,

$$\frac{\partial u}{\partial r} = -\frac{\rho_s g}{\mu_s}\frac{r}{2} + \frac{1}{r}C_0, \tag{B.9}$$

$$u(r) = -\frac{\rho_s g}{2\mu_s}\frac{r^2}{4} + C_0 \ln|r| + C_1. \tag{B.10}$$

In the bolus $R_a \leq r \leq R_a + R_b$,

$$\frac{\partial u}{\partial r} = -\frac{\rho_b g}{\mu_b}\frac{r}{2} + \frac{1}{r}C_2, \tag{B.11}$$

$$u(r) = -\frac{\rho_b g}{2\mu_b}\frac{r^2}{4} + C_2 \ln|r| + C_3. \tag{B.12}$$

The integration constants C_i can be found by applying the boundary conditions, leading to the following equations for velocity at steady state,

$$u(r) = -\frac{g\rho}{4\mu_b}\left(r^2 - 2R_a^2 \ln|r|\right) + C_1 \quad R_a \leq r \leq R_a + R_b, \tag{B.13}$$

$$u(r) = -\frac{g\rho}{4\mu_s} r^2 C_2 \ln|r| + C_3 \quad R_a + R_b \leq r \leq R, \tag{B.14}$$

$$C_1 = -\frac{g\rho}{4}\left(\frac{1}{\mu_b} - \frac{1}{\mu_s}\right)(R_a + R_b)^2 + \left(C_2 - \frac{g\rho}{2\mu_b}R_a^2\right)\ln|R_a + R_b| + C_3 \tag{B.15}$$

$$C_2 = \frac{g\rho}{2\mu_s} R_a^2, \tag{B.16}$$

$$C_3 = \frac{g\rho}{4\mu_s} \left(R^2 - 2R_a^2 \ln|R| \right). \tag{B.17}$$

B.1.2 Finite-Volume time-dependent solution

A finite-volume (FV) scheme can give us the time-dependent solution if solved numerically. We use a second-order space discretization, and a second-order implicit Crank-Nicholson time-stepping method. Special care is required for correct treatment at the saliva-bolus interface.

We discretize the one-dimensional problem into two sections, saliva and bolus. There are N_s and N_b saliva and bolus elements, respectively, and N elements total ($N = N_s + N_b$). Each cell, i, has a width Δr_i and a height Δz. Velocities u_i are computed at cell centres.

For an element i, the FV formulation is derived by integrating equation B.1 over each control volume,

$$\int_{dV} \rho_i \frac{\partial u_i}{\partial t} dV = \int_{dV} \mu_i \frac{1}{r} \frac{\partial}{\partial r} \left(r \frac{\partial u_i}{\partial r} \right) dV + g. \tag{B.18}$$

Integrating and applying the divergence theorem,

$$\rho_i \frac{\partial u_i}{\partial t} \Delta V = \oint_{\partial V} \mu_i \frac{\partial u_i}{\partial r} \Delta S + g. \tag{B.19}$$

$$\frac{\partial u_i}{\partial t} = \frac{\mu_i}{\rho_i r_i \Delta r_i} \left(\frac{\partial u_{i+\frac{1}{2}}}{\partial r} r_{i+\frac{1}{2}} - \frac{\partial u_{i-\frac{1}{2}}}{\partial r} r_{i-\frac{1}{2}} \right) + g, \tag{B.20}$$

where $r_{i+\frac{1}{2}} = r_i + \frac{\Delta r_i}{2}$ and $r_{i-\frac{1}{2}} = r_i - \frac{\Delta r_i}{2}$.

Within either fluid, the gradients can be discretized using a second-order centred scheme,

$$\frac{\partial u_{i+\frac{1}{2}}}{\partial r} = \frac{u_{i+1} - u_i}{\Delta r_{i+\frac{1}{2}}}, \tag{B.21}$$

where

$$\Delta r_{i+\frac{1}{2}} = \frac{\Delta r_i + \Delta r_{i+1}}{2}, \tag{B.22}$$

so that variable spacing can be handled correctly.

Discrete boundary conditions

For the wall boundary condition at $r = R, i = (N_b + N_s) - \frac{1}{2} = N - \frac{1}{2}$, we use $u(R) = 0$,

$$\frac{\partial u_{N-\frac{1}{2}}}{\partial r} = \frac{2u_{N-1}}{\Delta r_{N-1}}. \tag{B.23}$$

For the boundary condition at $r = R_a, i = -\frac{1}{2}$,

$$\frac{\partial u_{-\frac{1}{2}}}{\partial r} = 0. \tag{B.24}$$

At the saliva-bolus interface, $x = R_a + R_b, i = N_b - \frac{1}{2}$, we can not assume the left and right gradients are equal. The velocity gradient can be defined on either side to be a function of $u_{N_b-\frac{1}{2}}$.

$$\mu_b \frac{\partial u^-_{N_b-\frac{1}{2}}}{\partial r} = \mu_s \frac{\partial u^+_{N_b-\frac{1}{2}}}{\partial r}, \tag{B.25}$$

$$\mu_b \frac{u_{N_b-\frac{1}{2}} - u_{N_b-1}}{\frac{1}{2}\Delta r_{N_b-1}} = \mu_s \frac{u_{N_b} - u_{N_b-\frac{1}{2}}}{\frac{1}{2}\Delta r_{N_b}}, \tag{B.26}$$

leading to the following equation for $u_{N_b-\frac{1}{2}}$,

$$u_{N_b-\frac{1}{2}} = \frac{1}{1+a} u_{N_b} + \frac{a}{1+a} u_{N_b-1}, \tag{B.27}$$

where

$$a = \frac{\mu_b}{\mu_s} \frac{\Delta r_{N_b}}{\Delta r_{N_b-1}}. \tag{B.28}$$

This gives us the discrete forms of the velocity gradient adjacent to the saliva-bolus boundary for both sides,

$$\frac{\partial u^-_{N_b-\frac{1}{2}}}{\partial r} = \frac{2}{(1+a)\Delta r_{N_b-1}} (u_{N_b} - u_{N_b-1}), \tag{B.29}$$

$$\frac{\partial u^+_{N_b-\frac{1}{2}}}{\partial r} = \frac{2a}{(1+a)\Delta r_{N_b-1}} (u_{N_b} - u_{N_b-1}). \tag{B.30}$$

Time integration

The time integral can be discretized using the second-order implicit Crank-Nicholson method,

$$\frac{\partial u_i}{\partial t} = \frac{u_i^{n+1} - u_i^n}{\Delta t} = \frac{1}{2}\left(F^{n+1}_{i-\frac{1}{2}} + F^n_{i-\frac{1}{2}}\right) + \frac{1}{2}\left(F^{n+1}_{i+\frac{1}{2}} + F^n_{i+\frac{1}{2}}\right) + g, \tag{B.31}$$

where the left and right fluxes for a cell i at time n are given by

$$F^n_{i-\frac{1}{2}} = \frac{\mu_i r_{i-\frac{1}{2}}}{\rho_i r_i \Delta r_i} \left(\frac{\partial u_{i-\frac{1}{2}}}{\partial r} \right)^n, \tag{B.32}$$

$$F^n_{i+\frac{1}{2}} = \frac{\mu_i r_{i+\frac{1}{2}}}{\rho_i r_i \Delta r_i} \left(\frac{\partial u_{i+\frac{1}{2}}}{\partial r} \right)^n. \tag{B.33}$$

Performing some basic algebra results in a tri-diagonal system of equations that is closed by the boundary conditions given previously.

B.1.3 Code verification

The numerical solver is implemented in Java. We assume the density in both the saliva and bolus are constant $\rho = 1000$. An acceleration of $g = 9.81$ is used to drive the flow. The velocity is initialized to zero everywhere and the system is evolved in time until the following convergence criteria is met,

$$|u_0^{n+1} - u_0^n| < 10^{-13}. \tag{B.34}$$

At steady state, for a variety of choices of μ_b, μ_s, R_s, R_b, R_a, we are able to demonstrate second order convergence in space by comparing to the theoretical steady-state solution of Section B.1.1.

For a single material, $\mu_b = \mu_s$, and $R_a = 0$, the flow is the Newtonian Hagen-Poiseuille flow. A theoretical time-dependent solution can be calculated from an infinite series of Bessel functions [70]. In these cases, the solver shows good agreement with the theoretical results.

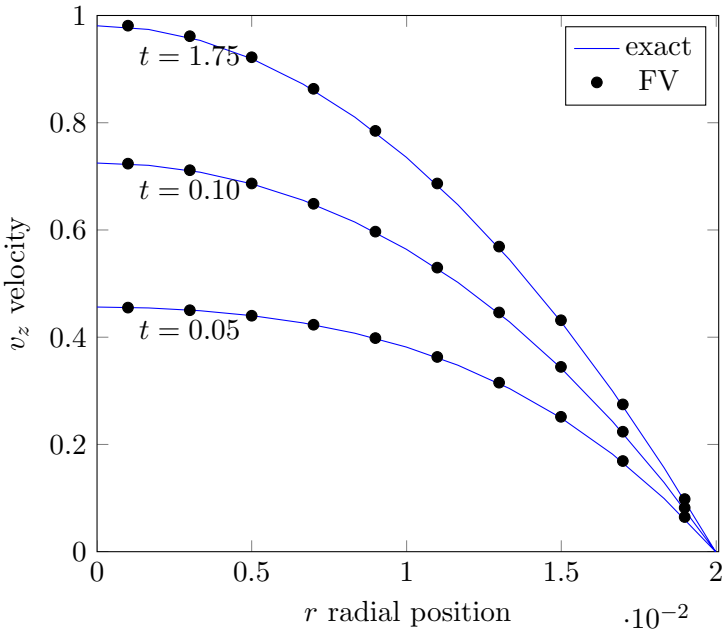

Figure B.2: Theoretical startup flow solution vs. FV solver for Newtonian flow in a pipe. $R_a = 0$, $R_b = R_s = 0.02$, $N_s = N_b = 5$, $\mu_b = \mu_s = 1$, $\rho = 1000$, $g = 9.81$.

Mesh size $(N_b + N_s)$	L_2 Error	Order
10	0.00290976	-
20	7.27920675E-4	1.99904924
40	1.82010841E-4	1.99975686
80	4.55046340E-5	1.99993900
160	1.13762741E-5	1.99998534

Table B.1: L_2 error convergence w.r.t. mesh size. $R_a = R_s = R_b = 0.01$, $N_s = N_b$, $\mu_b = mu_s = 1.0$.

Mesh size $(N_b + N_s)$	L_2 Error	Order
10	0.00485712	-
20	0.00121428	1.99999981
40	3.03569988E-4	2.00000012
80	7.58924447E-5	2.00000099
160	1.89730527E-5	2.00000445

Table B.2: L_2 error convergence w.r.t. mesh size. $R_a = 1.$, $R_s = 0.001$, $R_b = 0.01$, $N_s = N_b$, $\mu_b = 1$, $\mu_s = 0.01$.

B.2 Time dependent flows

The time-dependent startup velocity profile for a full-slip condition is:

$$u(t) = gt, \tag{B.35}$$

where g is acceleration due to gravity and t is the elapsed time. Consider a short-duration two-material startup flow where the bolus viscosity is much greater than the saliva viscosity. This section shows that the full-slip solution given above is a reasonable approximation for the bolus velocity profile for certain choices of saliva viscosity, μ_s, and the thickness, R_s. These choices of μ_s and R_s fall within the range of values that have been published in the lit-

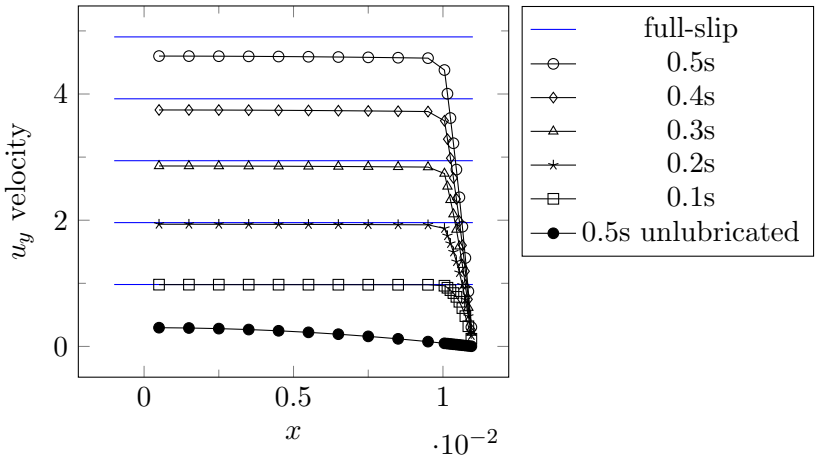

Figure B.3: Time dependent solutions of a two-material start-up pipe flow at various times. Low viscosity saliva lubricates a high-viscosity bolus in the centre of the pipe. For this plot, the parameters were $N = 20$, $R_a = 0$, $R_b = 10^-2$, $R_s = 10^-3$, $\mu_b = 1$, $\mu_s = 2e - 3$. For high viscosity boluses, the no-slip should give a much better approximation to the bolus flow than a no-slip condition.

erature, as long as the time duration is low enough. For example, Figure B.3 shows the velocity profiles at 0.1s intervals up to 0.5s. The bolus has $\mu_b = 1$, $R_b = 0.01$, while the saliva has $\mu_s = 0.002$ and thickness $R_s = 0.001$. For short time durations, the full-slip velocity gives a good approximation to the simulated bolus velocity profile. As the simulation progresses, the full-slip approximation begins to overshoot the simulated bolus velocity, however it still gives a much better approximation than an unlubricated (no-slip) velocity profile, also shown in Figure B.3. The unlubricated velocity profile at 0.5s was obtained by setting $\mu_s = \mu_b = 1$.

The quality of the full-slip approximation is most sensitive to three factors, μ_s, R_s, and the time duration. For a specific time, for example 0.25s after the start of the flow, we can plot the bolus flow rate, Q as a function

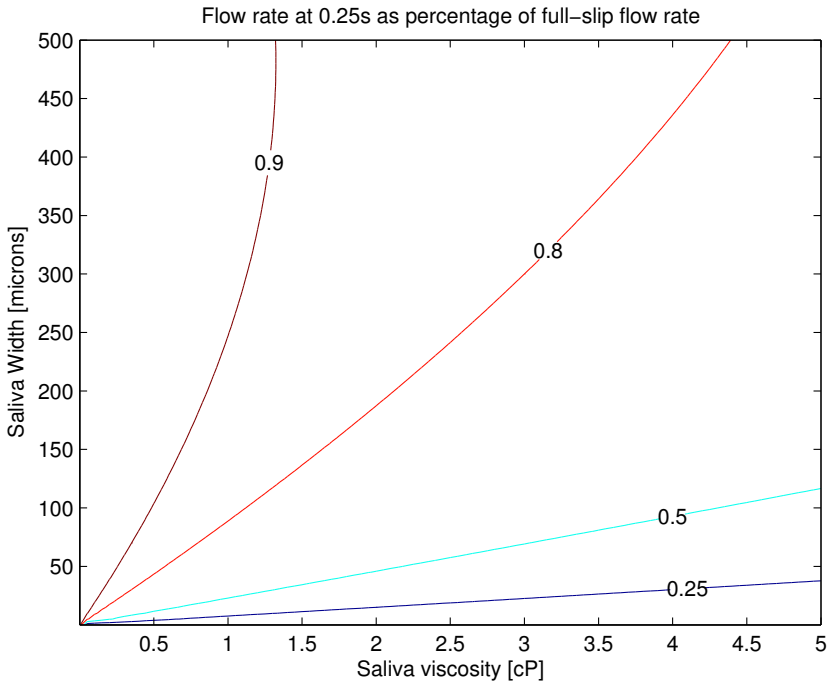

Figure B.4: Contour plot of flow rates, as percentage of the full-slip flow rate, at 0.25s, as a function of both μ_s and R_s.

of μ_s and R_s. Figure B.4 shows a contour plot where the lines correspond to the flow rate Q as a percentage of the theoretical full-slip flow-rate. On this plot, a no-slip (non-lubricated) flow can be found at the bottom edge of the plot, where R_s approaches zero. At 0.25s, the full-slip approximation may be reasonable for many choices of R_s and μ_s.

We can plot the constant contour line representing $Q = 85\%$ of the full-slip flow rate as a function of R_s and μ_s. Four such contour lines are shown in Figure B.5, representing the 85% cutoff line for times of 0.1s, 0.25s, 0.5s, and 1.0s. Areas to the left of the contour lines show the possible choices of R_s and μ_s that would be well approximated by a full-slip condition. These

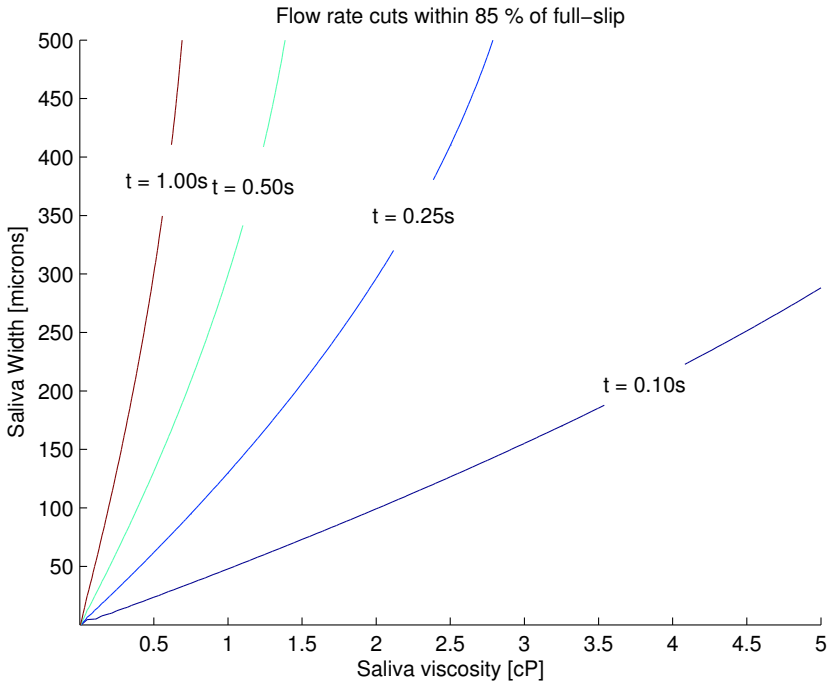

Figure B.5: Regions to the left of each contour represent choices of width, R_s, and viscosity, μ_S, for which a full-slip condition gives an approximation of flow rate within 85% of the actual flow rate.

experiments used a fixed time step $\Delta t = 10^{-3}$s, and bolus viscosity of $\mu_b = 1$. Decreasing the time step to 10^{-4} did not change the results significantly. The results were not sensitive to changes in bolus viscosity.

B.2.1 Measured values of saliva thickness and viscosity

Rantonen and Meurman [104] measured the mean viscosity of saliva at 90s^{-1} and 37°C of stimulated saliva to have a viscosity around 2–3 cP. The mean viscosity of unstimulated saliva was measured at around 4–8 cP. The thickness (R_s) of salivary film **in the oral cavity** has been estimated [20] to have

an average thickness of 50–100 microns, however this was for unstimulated saliva. This might underestimate the thickness of saliva during swallowing, since for example, the flow rate of stimulated saliva was measured to be about 5 times greater than for unstimulated saliva [104]. However it is not clear how this could be extrapolated to thickness of saliva during swallowing.